SIMULATION OF VARIABLE CAMBER CONTINUOUS TRAILING EDGE FLAP ON OUTBOARD AIRFOIL OF ATRA WING

BY

MOHAMMED ABDUL RAHEEM

A Thesis Presented to the
DEANSHIP OF GRADUATE STUDIES

KING FAHD UNIVERSITY OF PETROLEUM & MINERALS
DHAHRAN, SAUDI ARABIA

In Partial Fulfillment of the
Requirements for the Degree of

MASTER OF SCIENCE
In

AEROSPACE ENGINEERING

APRIL 2016

KING FAHD UNIVERSITY OF PETROLEUM & MINERALS
DHAHRAN 31261, SAUDI ARABIA

DEANSHIP OF GRADUATE STUDIES

This thesis, written by **MOHAMMED ABDUL RAHEEM** under the direction of his thesis adviser and approved by his thesis committee, has been presented to and accepted by the Dean of Graduate Studies, in partial fulfillment of the requirements for the degree of **MASTER OF SCIENCE IN AEROSPACE ENGINEERING**.

Thesis Committee

Dr. Prasetyo Edi (Adviser)

Dr. Ahmed Z. Ali Al-Garni (Co-adviser)

Dr. Abido, Mohammed Ali Y. (Member)

Dr. Ahmet Z. Sahin (Member)

Dr. Wael G. Abdelrahman (Member)

١٢/٨/١٤٣٧هـ

Dr. Ahmed Z. Ali Al-Garni
Department Chairman

Dr. Salam A. Zummo
Dean of Graduate Studies

23/5/16

Date

Dedication

To my beloved parents who always strived towards giving their children a quality education.

AND

To my uncle Mohammed Sirajuddin, for his support since our school education.

AND

To my sisters and brother for their love and support.

ACKNOWLEDGMENTS

"O my Lord! Increase me in my knowledge!" (20:114) "O Allah I ask you for knowledge that is of benefit."

All praises and worship are for Allah alone, the most glorious and the most merciful; who has blessed us with Iman. I always ask for his forgiveness as well as showing us the right path. Peace and blessings be on the succorer of humanity, the gem of mankind, the ruby of the universe,the mercy upon mankind, the one whose beauty is unmatched, the one whose strength is most supreme, the one whose knowledge is beyond the books, the one whose modesty is paramount, the last and the final Messenger of Allah, Mohammed (Sallalahu Alaihi wa sallam), upon his family, his companions, and all those who follow him until the day of judgment.

I owe to express a deep sense of gratitude to my thesis adviser Dr. Prasetyo Edi for his inspiration, patience, timely guidance, valuable ideas throughout my thesis. I feel very great to say; he has successfully instilled in me a passion for scientific research, which will continue to guide me for many more years to come.

I would like to thank my co-adviser Dr. Ahmed Z. Ali Al- Garni (Chairman, Department of Aerospace Engineering) for his constant guidance, interactions, motivation, encouragement through out the Master's program. Interactions with him has always ended with great passion for research. His words gave a new life to my efforts in hard times and his support helped me in writing my thesis properly. He guided me the perfect direction so that I never get deviated.

I would like to appreciate my committee members Dr. Abido, Mohammed Ali Y., Dr. Ahmet Z. Sahin and Dr. Wael G. Abdelrahman for their thoughtful suggestions, insightful comments, and support during my thesis phase.

I would like to appreciate my faculty members who taught me courses in KFUPM which were to the standards of other reputed universities.

I am blessed with opportunities with my stay at KFUPM and am thankful to the Department of Aerospace Engineering for giving me a chance to study in this esteemed university. I am thankful to the university for providing the resources and various benefits during the stay.

I would like to appreciate and thank my parents, Mrs. & Mr. Mohammed Abdul Raoof from the bottom of my heart for their patience, care, love and moral support. I am grateful to my sisters and brother for motivating me and for their valuable efforts throughout my life.

Thanks to all the friends who helped me during my Master's program. Especial thanks to Meer Abdul Mateen khan my room mate for being a family when I was away from the home. Thanks to Mohammed Yahiya Naveed, Mohammed Shahabuddin, Syed Azher Hussain, Faisal Moiz Hussain, Mohammad Raghib Shakeel, Mr. Syed Shiraz Mahdi, Mohammed Younus Siddiqui and Suleman Haroon.

TABLE OF CONTENTS

ACKNOWLEDGMENTS **v**

LIST OF TABLES **xi**

LIST OF FIGURES **xiii**

NOMENCLATURE **xix**

ABSTRACT (ENGLISH) **xxii**

ABSTRACT (ARABIC) **xxiii**

CHAPTER 1 INTRODUCTION **1**

- 1.1 Motivation 4
  - 1.1.1 Aerodynamic motivation: 4
  - 1.1.2 Cost motivation: 5
- 1.2 Background 7
  - 1.2.1 Variable Camber Continuous Trailing Edge Flap (VCCTEF) 8
- 1.3 Present Approach 10
  - 1.3.1 Wing of Advanced Technology Regional Aircraft(W-ATRA) 10
  - 1.3.2 Addition of VCCTEF to W-ATRA 11
- 1.4 Objectives 16
- 1.5 Thesis Outline 16

CHAPTER 2 LITERATURE REVIEW **18**

2.1 Review of previous work 18
2.2 Conclusion 29

CHAPTER 3 RESEARCH METHODOLOGY & THEORETICAL LIFT INCREMENT 31

3.1 Introduction 31
3.2 Navier-Stokes equations 34
3.3 Reynolds averaging 36
3.4 Reynolds-Averaged Navier-Stokes equation 38
  3.4.1 Reynolds form of the continuity equation 39
  3.4.2 Reynolds form of the momentum equation 40
  3.4.3 Reynolds form of the energy equation 42
  3.4.4 Need for turbulence modeling 43
3.5 Introduction to turbulence modeling 45
  3.5.1 Turbulent closure 45
  3.5.2 Classification of Turbulence Models: 47
  3.5.3 Algebraic or Zero- Equation Models 48
  3.5.4 Boussinesq approximation 49
  3.5.5 One equation Spalart-Allmaras model 50
  3.5.6 Boundary conditions for Spalart Allmaras model 51
  3.5.7 Transition k-kl-omega 52
  3.5.8 Boundary conditions for Transition k-kl-omega model . . . 53
3.6 Numerical method 54
  3.6.1 Generic form of governing equations 56
  3.6.2 Finite volume method 58
  3.6.3 Flux-difference splitting scheme 63
  3.6.4 Roe scheme 64
3.7 Theoretical Lift Increment 73
3.8 Conclusion 77

CHAPTER 4 GRID GENERATION & SIMULATION METHODOLOGY 79
4.1 Grid Generation guidelines 79
4.2 Considerations for Near Wall Mesh 80
4.2.1 Spalart-Allmaras (SA) Model 82
4.2.2 Transition Model (Transition k-kl-omega) 83
4.3 Validation Cases 83
4.3.1 Validation of SA model 84
4.3.2 Validation of Transition k-kl-omega model 86
4.4 Modeling geometries of present study 88
4.4.1 Modeling NACA 0012, Size & Shape of Domain 88
4.4.2 Modeling NACA 63209 and RAE 2822 90
4.4.3 Modeling Baseline and VCCTEF 91
4.5 Grids Generated 94
4.5.1 NACA 0012 Grids Generated 94
4.5.2 NACA 63209 AND RAE 2822 Grid 99
4.5.3 Baseline & VCCTEF Grids 101
4.6 Simulation in FLUENT 105
4.6.1 Flight conditions 105
4.7 Boundary condition 105
4.8 Conclusion 106

CHAPTER 5 RESULTS OF FULLY TURBULENT SIMULATION ON BASELINE & VCCTEF 107
5.1 Validation using NACA 0012 107
5.2 Outboard Airfoil or Kink 114
5.2.1 Baseline Case 114
5.2.2 Comparison of Baseline with VCCTEF 127
5.2.3 Comparison of computational lift increment with theoretical lift increment 133

5.3 Conclusion 135

CHAPTER 6 RESULTS OF TRANSITION SIMULATION ON BASELINE & VCCTEF 136

6.1 Validation using NACA 63209 137
6.2 Validation using RAE 2822 airfoil 138
6.3 Outboard Airfoil or Kink (Transition k-kl-omega Model) 142
  6.3.1 Baseline 142
  6.3.2 Comparison of Baseline and VCCTEF (Transition k-kl-omega model) 150
  6.3.3 Comparison of computational lift increment with theoretical lift increment 156

CHAPTER 7 CONCLUSIONS AND RECOMMENDATIONS 158

7.1 Conclusion 158
7.2 Recommendations & Future Work 160

REFERENCES 161

APPENDIX A 173

APPENDIX B 177

VITAE 190

LIST OF TABLES

1.1 VCCTEF configurations in study [4] 13

3.1 Model Constants for Transition k-kl-omega [60] 54

4.1 NACA 0012 with T.E thickness 99
4.2 Grid of NACA 63209 99
4.3 Grids of Baseline & VCCTEF 102
4.4 Grids of Baseline & VCCTEF (Transition Analysis) 104
4.5 U.S STANDARD ATMOSPHERE 105

5.1 Baseline Case: Pressure and viscous contribution to C_d (M=0.7) . 126
5.2 Baseline Case: Pressure and viscous contribution to C_l (M=0.7) . 126

6.1 Transition location for Grid I,II and III at $\alpha = 0°$, $2°$ and $4°$ . . . 147
6.2 Baseline Case (Transition k-kl-omega): Pressure and viscous contribution to C_d (M=0.7) 149
6.3 Baseline Case (Transition k-kl-omega): Pressure and viscous contribution to C_l (M=0.7) 149

A.1 VCCTEF 123 Case: Pressure and viscous contribution to C_d . . . 173
A.2 VCCTEF 123 Case: Pressure and viscous contribution to C_l . . . 173
A.3 VCCTEF 222 Case: Pressure and viscous contribution to C_d . . . 174
A.4 VCCTEF 222 Case: Pressure and viscous contribution to C_l . . . 174
A.5 VCCTEF 321 Case: Pressure and viscous contribution to C_d . . . 174
A.6 VCCTEF 321 Case: Pressure and viscous contribution to C_l . . . 175

A.7 VCCTEF 33 Case: Pressure and viscous contribution to C_d 175
A.8 VCCTEF 33 Case: Pressure and viscous contribution to C_l 175
A.9 VCCTEF 6 Case: Pressure and viscous contribution to C_d 176
A.10 VCCTEF 6 Case: Pressure and viscous contribution to C_l 176

LIST OF FIGURES

1.1 Aircraft Sale Price [8] 5

1.2 Direct Operation Cost (DOC)breakdown [8] 6

1.3 Percentage contribution of different types of Drag [8] [11] 7

1.4 VCCTEF deployed on a generic transport model (GTM) [4] . . . 9

1.5 The Variable Camber Flap Control uses Shape Memory Alloy Torque Rod and Electric Drive Actuation [12] [13] 10

1.6 Geometric details of a ATRA wing [1] 11

1.7 W-ATRA (a) thickness distribution (b) twist distribution [1] . . . 12

1.8 Complete VCCTEF configuration over GTM 13

1.9 Schematic of VCCTEF 3 & 1 segment flap 14

3.1 Flow Chart for the topics in Research Methodology 33

3.2 Relation between u, $\overline{u}$, u' in a (a) Steady (b) Unsteady turbulent flow 36

3.3 Two-Dimensional Finite Volume [63] 60

3.4 (a) Two-dimensional control volume used in finite volume formulation, where the grid points are represented by solid circles with small indices of i and j and cell centers are shown by crosses represented by caps indices of I and J. (b) Calculation of normal surface vector $S_{i,j+1/2}$ [64] 61

3.5 The conservative variable $U_{I,J}$ at cell center calculated from the fluxes F and G passing through the cell boundaries in the x- and y-directions.[64] 62

3.6 Decomposed flux for the linear Riemann problem [63] 68
3.7 Flap hinge position & absolute deflection of camber segment (Not to be Scaled) 77

4.1 Log Law (Variation of u^+ with y^+) 81
4.2 Experimental results of (a) C_l vs AoA ($\alpha°$) (b) C_d vs C_l [73] . . . 84
4.3 NACA 0012 experimental results of C_p vs x/c (a) α= 0 ° (b) α= 10 ° (c) α= 15 ° [73] 85
4.4 Experimental results of NACA 63209 (a) C_l vs AoA ($\alpha°$) (b) C_d vs C_l [76] 86
4.5 Experimental results of RAE 2822 (a) C_l vs AoA ($\alpha°$) (b) C_d vs C_l [77] 87
4.6 RAE 2822 experimental results of C_p vs x/c (a) α= 2.4° (b) α= -2.18° [77] 88
4.7 Domain Size is $25\bar{c}$ 89
4.8 Baseline Coordinates 91
4.9 Coordinates comparison of Baseline and VCCTEF (SCALED COORDINATES) 93
4.10 Chord Line representation of VCCTEF 94
4.11 C_l vs number of Grid [79] 94
4.12 Grids Studied for NACA 0012 96
4.13 Present figure of mesh 660 X 150 (460 points around airfoil 25 $\bar{c}$) . 97
4.14 Near airfoil mesh for NACA 0012 98
4.15 NACA 0012 Mesh (a) with no T.E. thickness (b) with T.E. thickness 98
4.16 RAE 2822 mesh, 1122 × 200 (922 points around airfoil) 100
4.17 Near-body mesh of RAE 2822 airfoil 101
4.18 Full Grid of Baseline[692 × 150 (492 pts. around airfoil)] 102

4.19 Representative Near-Body Mesh 692 × 150 (492 points on airfoil surface) (a) Baseline (b) VCCTEF 123 (c) VCCTEF 222 (d) VCCTEF 321 (e) VCCTEF 33 (f) VCCTEF 6 103
4.20 Full grid of baseline [1122 × 200 (922 pts. around airfoil)] 104

5.1 Comparison of simulation results C_L vs. α 108
5.2 C_l vs. α 109
5.3 Comparison of simulation results C_D vs. C_L 110
5.4 C_d vs. C_l 111
5.5 C_d vs. C_l (only SA model) 111
5.6 C_d vs. α 112
5.7 C_d vs. α (only SA model) 113
5.8 C_p vs. x/c 0AoA 113
5.9 C_p vs. x/c 10AoA 114
5.10 C_p vs. x/c 15AoA 114
5.11 comparison of cf vs. x/c at 0AoA 115
5.12 Drag divergence study (Baseline) 116
5.13 C_l vs α (Baseline) 117
5.14 Variation of L/D with Mach number(Baseline) 118
5.15 C_p vs x/c at M = 0.7 118
5.16 C_p vs x/c at M = 0.744 119
5.17 C_p vs x/c at M = 0.8 120
5.18 Pressure contour 1.1 AoA (M=0.8) 120
5.19 Pressure contour of Baseline at α =-2°, M =0.7 121
5.20 Mach contour of Baseline at α =-2°, M =0.7 121
5.21 Pressure contour of Baseline at α =-1°, M =0.7 122
5.22 Mach contour of Baseline at α =-1°, M =0.7 122
5.23 Pressure contour of Baseline at α =0°, M =0.7 123
5.24 Mach contour of Baseline at α =0°, M =0.7 123
5.25 Pressure contour of Baseline at α = 1.1°, M =0.7 124

5.26 Mach contour of Baseline at $\alpha = 1.1°$, M =0.7 124
5.27 Pressure contour of Baseline at α =2°, M =0.7 125
5.28 Mach contour of Baseline at α =2°, M =0.7 125
5.29 Variation of c_d with α 127
5.30 Variation c_l with α 128
5.31 Baseline and VCCTEF comparison: drag polar 129
5.32 Baseline Case: comparison of overall drag and pressure drag . . . 129
5.33 Cp comparison of baseline with VCCTEF configuration for 0^o AoA 130
5.34 L/D variation with α 131
5.35 L/D variation with C_l 132
5.36 Theoretical and computational lift coefficient c_l comparison (SA model) 134

6.1 C_l vs. AoA (α) (NACA 63209) 137
6.2 C_d vs. C_l (NACA 63209) 138
6.3 C_n vs. α variation, RAE 2822 airfoil 139
6.4 C_d vs. α variation, RAE 2822 airfoil 140
6.5 C_p vs. x/c, α = 2.4°, RAE 2822 airfoil 141
6.6 C_p vs. x/c, α = -2.18°, RAE 2822 airfoil 141
6.7 C_l vs. Grid (M=0.7, Re = 21.6 million) 143
6.8 C_d vs. Grid (M=0.7, Re = 21.6 million) 143
6.9 L/D vs. Grid (M=0.7, Re = 21.6 million) 144
6.10 Baseline results of C_p vs. x/c using Transition k-kl-omega (a) α= 0° (b) α= 2° (c) α= 4° 145
6.11 Baseline results of C_f vs. x/c using Transition k-kl-omega (a) α= 0° (b) α= 2° (c) α= 4° 146
6.12 Baseline results of M vs. x/c using Transition k-kl-omega (a) α= 0° (b) α= 2° (c) α= 4° 148
6.13 Variation c_d with α (Transition model) 151
6.14 Variation c_l with α (Transition model) 152

6.15 Baseline and VCCTEF comparison: drag polar (Transition model) 152
6.16 Baseline Case: Comparison of overall drag and pressure drag (Transition model) 153
6.17 C_p vs. x/c comparison of baseline with VCCTEF configuration for 0^o AoA (Transition model) 153
6.18 M vs. x/c comparison of baseline with VCCTEF configuration for 0^o AoA (Transition model) 154
6.19 L/D variation with α (Transition model) 155
6.20 L/D variation with C_l(Transition model) 156
6.21 Theoretical and computational lift coefficient C_l comparison (Transition model) 157

B.1 Pressure contour of VCCTEF 123 at -2 AoA at M =0.7 177
B.2 Mach contour of VCCTEF 123 at -2 AoA at M =0.7 177
B.3 Pressure contour of VCCTEF 123 at 0 AoA at M =0.7 178
B.4 Mach contour of VCCTEF 123 at 0 AoA at M =0.7 178
B.5 Pressure contour of VCCTEF 123 at 1.1 AoA at M =0.7 179
B.6 Mach contour of VCCTEF 123 at 1.1 AoA at M =0.7 179
B.7 Pressure contour of VCCTEF 222 at -2 AoA at M =0.7 180
B.8 Mach contour of VCCTEF 222 at -2 AoA at M =0.7 180
B.9 Pressure contour of VCCTEF 222 at 0 AoA at M =0.7 181
B.10 Mach contour of VCCTEF 222 at 0 AoA at M =0.7 181
B.11 Pressure contour of VCCTEF 222 at 1.1 AoA at M =0.7 182
B.12 Mach contour of VCCTEF 222 at 1.1 AoA at M =0.7 182
B.13 Pressure contour of VCCTEF 321 at -2 AoA at M =0.7 183
B.14 Mach contour of VCCTEF 321 at -2 AoA at M =0.7 183
B.15 Pressure contour of VCCTEF 321 at 0 AoA at M =0.7 184
B.16 Mach contour of VCCTEF 321 at 0 AoA at M =0.7 184
B.17 Pressure contour of VCCTEF 321 at 1.1 AoA at M =0.7 185
B.18 Mach contour of VCCTEF 321 at 1.1 AoA at M =0.7 185

B.19 Pressure contour of VCCTEF 33 at 0 AoA at M =0.7 186

B.20 Mach contour of VCCTEF 33 at 0 AoA at M =0.7 186

B.21 Pressure contour of VCCTEF 33 at 1.1 AoA at M =0.7 187

B.22 Mach contour of VCCTEF 33 at 1.1 AoA at M =0.7 187

B.23 Presure contour of VCCTEF 6 at 0 AoA at M =0.7 188

B.24 Mach contour of VCCTEF 6 at 0 AoA at M =0.7 188

B.25 Presure contour of VCCTEF 6 at 1.1 AoA at M =0.7 189

B.26 Mach contour of VCCTEF 6 at 1.1 AoA at M =0.7 189

NOMENCLATURE

C_p	Coefficient of Pressure
C_d	Coefficient of Drag
C_l	Coefficient of Lift
C_n	Coefficient of Normal force
L/D	Lift to Drag ratio
x/c	Length to Chord Ratio
C_f	Coefficient of Friction
Cf	Flap Chord Length
α	Angle of Attack
C_{dp}	Pressure drag coefficient
C_{dv}	Viscous drag coefficient.
x	Position where velocity component normal to chord line induced by vortex sheet is found
V_∞	Free Stream Velocity
M_∞	Free Stream Mach number
α	Angle of Attack (AoA)
$\gamma(\xi)d\xi$	Strength of the vortex sheet of elemental length $d\xi$ at a distance ξ
n	Number of flap segments
x_i	The position of the i-th flap from the trailing edge.

Subscript

i	Segment of the flap

LIST OF ABBREVIATIONS

AASC	Active Aeroelastic Shape Control
AoA	Angle of Attack
ATRA	Advanced Technology Regional Aircraft
BWB	Blended Wing Body
CFD	Computational Fluid Dynamics
DOC	Direct Operation Cost
GTM	Generic Transport Model
HLFC	Hybrid Laminar Flow Control
LFC	Laminar Flow Control
LFCS	Laminar Flow Control by Suction
NLF	Natural Laminar Flow
L.E	Leading Edge
NACA	National Advisory Committee for Aeronautics
NASA	National Aeronautics and Space Administration
OEW	Operational Empty Weight
Re	Reynolds Number
SMA	Shaped memory alloy
SOB	Side of the Body
T.E	Trailing Edge
UWAL	University of Washington Aeronautical Laboratory
VC	Variable Camber

VCCTEF	Variable Camber Continuous Trailing Edge Flap
VCK	Variable Camber Krueger
W-ATRA	Wing of Advanced Technology Regional Aircraft

THESIS ABSTRACT

NAME:	Mohammed Abdul Raheem
TITLE OF STUDY:	Simulation of Variable Camber Continuous Trailing Edge Flap on Outboard Airfoil of ATRA Wing
MAJOR FIELD:	Aerospace Engineering
DATE OF DEGREE:	April 2016

Effect on the environment due to emissions can be minimized by reducing the fuel consumption of an aircraft. One way of doing this is to increase the Lift to Drag (L/D) ratio. Using Variable Camber Continuous Trailing Edge Flap (VC-CTEF) on the outboard airfoil of Wing of Advanced Technology Regional Aircraft (W-ATRA), a 7.2 % increment in L/D during cruise is achieved. Simulations were performed at an altitude of 10,000 m and cruise Mach number = 0.774, using Reynolds-Averaged Navier-Stokes equations coupled with one-equation Spalart-Allmaras model and three equations Transition k-kl-omega model available in the ANSYS Fluent software. The results suggested that VCCTEF 123 has the best L/D ratio. The computed results of incremental lift coefficients are in agreement with theoretical lift coefficient increment.

ملخص الرسالة

الاسم الكامل: محمد عبد الرحيم محمد عبد الرؤوف

عنوان الرسالة: محاكاة قلابة الحافة الخلفية متغيرة الاحديداب في المقطع العرضي الخارجي لجناح الطائرة الإقليمية ذات التقنية المتقدمة.

التخصص: هندسة الطيران والفضاء

تاريخ الدرجة العلمية: أبريل 2016

يمكن خفض تأثير الانبعاثات على البيئة عن طريق تقليل استهلاك الطائرات للوقود، أحد الطرق لتحقيق ذلك زيادة نسبة الرفع الي الإعاقة، فباستخدام قلابة الحافة الخلفية متغيرة الاحديداب في المقطع العرضي الخارجي لجناح الطائرة الإقليمية ذات التقنية المتقدمة يتم زيادة نسبة الرفع للإعاقة بمقدار 7.2% أثناء الطيران المطرد، تم إجراء محاكاة على ارتفاع 10,000متر ورقم ماخ 0.774 باستخدام معادلات نافير ستوكس المعدلة بواسطة رينولدز، والمرتبطة بنموذج سبلارت الماراز ذي المعادلة الواحدة ونموذج k-kl-ω للانتقال ذي الثلاث معادلات والمتاح في برنامج ANSYS Fluent، أشارت النتائج إلى أن محاكي قلابة الحافة الخلفية متغيرة الاحديداب في المقطع العرضي الخارجي لجناح الطائرة الإقليمية ذات التقنية المتقدمة رقم 123 يحقق افضل نسبة رفع الي إعاقة، و تتفق النتائج المحسوبة للزيادة في معاملات الرفع مع الزيادة المحسوبة نظريا لمعاملات الرفع.

CHAPTER 1

INTRODUCTION

The research in aircraft industry has always been focused on methods to make aircraft more energy-efficient. There has been a remarkable improvement in aircraft structures with the advent of materials that are lighter and have good strength-to-weight ratios. In aircraft propulsion, engines are becoming more and more efficient. A lot of research has been done in aerodynamics, as well, to increase lift and decrease drag. The study of improvement in aerodynamics by changing camber began as early as in 1916 when flaps were used on Fairey Hamble Baby aircraft and in 1919, slots were used on H.P.17 (modified Airco DH.9A aircraft). New aircraft wing configurations are designed and studied for improved performance, for example, in 1997 BWB configuration flew, which was designed by NASA for the improved payload for strategic airlift, lower noise and increased fuel efficiency. Edi et.al [1] investigated the Hybrid Laminar flow control (HLFC) wing with Variable Camber (VC) flap. The deflection of variable camber can keep the pressure distribution over the forward part of the airfoil similar (as the designed pressure distribution) along the span, even if, there is a change in C_l and M_∞ from design values [2]. With careful design of a VC flap, it can be used to reduce the wave drag penalty and to sustain attached flow in the turbulent mode [3]. Plain flap increases lift compared to baseline configuration (configuration in which there is no flap deflection) but increases drag as well. Fowler flap has higher L/D ratio compared to plain flap. The above-discussed methods, use the aerodynamic considerations only but with the advent of flexible materials in the aviation industry other constraints like structural constraints, must be considered as well, to improve aerodynamic efficiency. Aerodynamically efficient aircraft use highly efficient engines which are lightweight and use high strength materials to enhance the efficiency. One of the major development in the industry is the use of advanced composite materials that has considerably reduced the airframe operational empty weight (OEW) and structural rigidity; at the same time preserving its load carrying capacity, efficiency is increased. Forces and moments generated due to the aerodynamics of an airplane interact with aero-elastics due to the increased structural flexibility. This is decreasing the aerodynamic efficiency [4]. To get a better control over wing aeroelasticity with significant drag reduction a study entitled “Elastically Shape Future Air Vehicle Concept” was done in the year 2010 [5],[6]. This study showed that one can optimize local (Angle of Attack) AoA of wing section for improving aerodynamic efficiency by drag reduction during the cruise; improved lift performance during landing and take-off. In addition to this, wing twist and vertical bending can be controlled by aero elastically shaping highly flexible wings. Conventional flap and slats are not efficient with aeroelastic wing shaping control for drag minimization, as conventional flap and slat devices inherently generate drag as they increase lift. In order to address this issue, a new concept called Variable Camber Continuous Trailing Edge Flap (VC-CTEF) system was developed by NASA. In this type of variable camber, a three segment flap (along the chord) is used instead of a single plain flap. Along the span, the flap is divided into segments of 2 feet [4]. Each flap individually twists along the span and this result in a different twist for each flight mission such as cruise, climb and descent; this contributes to best Lift to Drag (L/D) ratio for each flight segment. The individual 2-foot span-wise flap sections are connected with a flexible covering, so that no free space exists between the flap sections, thus preventing additional drag and noise that would otherwise occur due to flow phenomena such as vortex shedding from these open spaces. The present work is the continuation of the Ph.D. work of Dr. Prasetyo Edi [1] along with the addition of VCCTEF (Variable camber continuous trailing edge flap). An attempt is made to modify the ATRA wing to reduce fuel consumption by increasing aerodynamic efficiency (L/D). This study is computationally done in ANSYS FLUENT, to find L/D ratio with and without deflection of flap for the outboard airfoil of W-ATRA wing. The same airfoil is used as an outboard airfoil along the span in W-ATRA wing after the wing break section.

The airfoil has a chord length of 3587 mm (141.2205 inches). VCCTEF overall flap chord is 30% of airfoil chord measured from the first hinge line. The results identify the most aerodynamic efficient VCCTEF configuration in cruise. The computational results of incremental lift coefficient (C_l) are validated by using thin airfoil theory (potential flow).

1.1 Motivation

There are two types of motivation, Aerodynamic and Cost motivation.

1.1.1 Aerodynamic motivation:

During the take-off and landing, one can observe the extension of flaps, usage of slats and slots. While in cruise, these are not used except when the aircraft maneuvers or deploys control surfaces during turbulence . This means that the flaps are dead weight and have no use during the cruise. The presence of flap track fairing increases drag. In this regard, Boeing Research and Technology has expressed a strong interest in future partnership with NASA to further advance the system-level concepts developed by the project; namely, the Variable camber continuous trailing edge flap (VCCTEF) and the elastic wing shaping control, for possible future aircraft applications [6].

VCCTEF not only increases lift but also reduces the drag, this gives an increased Lift to drag (L/D) ratio. Fuel consumption is dependent on the L/D ratio [7]. Equation 1.1 show that fuel consumption rate is inversely dependent on the change in aerodynamic efficiency. Thus increasing the L/D ratio reduces the fuel consumption, providing an increased fuel efficiency.

$$d\bar{W}_f = -d\bar{E} \tag{1.1}$$

E: aerodynamic efficiency L/D,

$\bar{E}$: change in E, percent,

$\bar{W}_f$: fuel consumption rate, %.

1.1.2 Cost motivation:

As shown in Fig. 1.1, "Research, Testing Project design" represents 5 % of the aircraft sale price which in turn is 40 % of the direct operation cost(see Fig. 1.2). Hence, "Research, Testing Project design" forms 2 % (5 % × 40 %) of the Direct Operation Cost (DOC). Fuel constitutes for 20 % of DOC and 10 % of fuel saving implies 2 % (10 % × 20 %) reduction of DOC. It is worth to almost double the total research effort[8] .

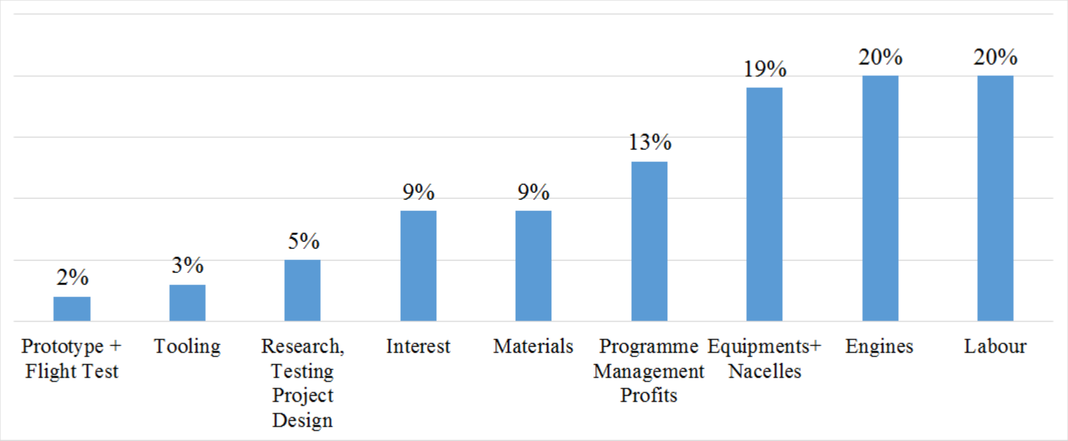

Figure 1.1: Aircraft Sale Price [8]

The fuel savings are not only linked to the improvement of engines but are also linked to drag reduction, in a global efficiency improvement approach. This justifies the importance of research effort carried out by the industry and by the research establishments, and the relatively large amount of money dedicated to this efficiency topic by the European Union in the successive aeronautical cooperative programs.

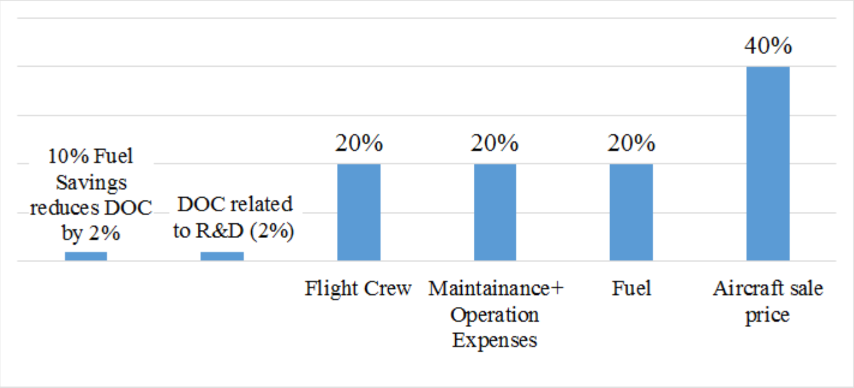

Figure 1.2: Direct Operation Cost (DOC)breakdown [8]

Glenn et.al [9] suggests that an important factor in the operation of airlines is the aircraft efficiency. Modern, long-range wide-body transport aircraft can have up to 50% of its total expenses due to the fuel cost. If one can reduce the consumption of fuel by 3% then there can be a saving of $ 300,000 in a year.

Fig. 1.2 shows that aircraft sale price is about 40% of the Direct Operation Cost (DOC), this figure was drawn from the data of Marec[8] which extracts the EUROMART study information figures.

1.2 Background

The wing of an airplane provides the lift for the aircraft. The wing must be designed such that, the coefficient of lift (C_l) is high enough during take-off and landing. During cruise they must give the best Lift to drag (L/D) ratio. Higher C_l is produced by varying camber during take-off and landing. Lift increases or decreases as the distance between camber line and the chord line increases or decreases. If there is a negative distance between camber and the chord line, then the lift becomes negative i.e. if the chord line is above the camber line the lift is negative. It was Sir George Cayley who first described the benefits of the camber in early 19^{th} Century.[10] . Fig. 1.3 shows the percentage contribution of various drags is reproduced from Green et.al[11] and Marec et.al [8]. Reduction in frictional and induced drag offers a good amount of chance to reduce the total amount of drag.

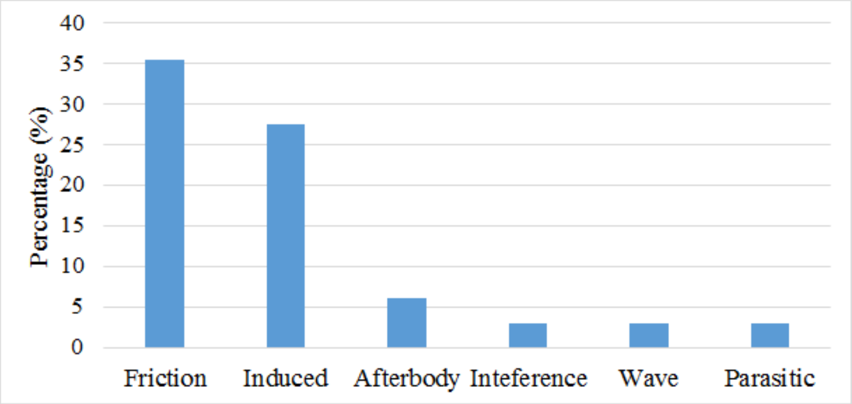

Figure 1.3: Percentage contribution of different types of Drag [8] [11]

Laminar flow has less skin friction drag compared to turbulent flow; hence delaying the transition point and making the flow laminar is one of the methods for drag reduction. At high Mach numbers and at a higher angle of attacks (AoA), when there is shock formation, the contribution of the frictional component of drag reduces and pressure component of the drag increases. Thus, flow largely behaves as an inviscid flow.

1.2.1 Variable Camber Continuous Trailing Edge Flap (VCCTEF)

The initial study indicates that VCCTEF system can be used to have a significant fuel saving by reducing drag. As part of the wing shaping control strategy, an approach for high lift devices is to be considered, while meeting all other performance requirements, to have drag reduction by aeroelastic wing shaping control and by active span load. Experimental study shows that VCCTEF can achieve a drag reduction of up to 6.31% and an improvement in the lift-to-drag ratio (L/D) of up to 4.85%.

Fig. 1.4 illustrates the VCCTEF deployed on a generic transport model. NASA and Boeing are currently conducting a joint study to develop the VCCTEF further under the research element Active Aeroelastic Shape Control (AASC) within the Fixed Wing project . VCCTEF is developed for an airframe similar to B757 i.e. NASA Generic Transport model (GTM) in which for actuation light weight Shaped Memory Alloy (SMA) is employed and three segments are made along the chord for varying camber. This cambered flap is expected to have a reduction in drag compared to the single flap which is conventionally used. Along

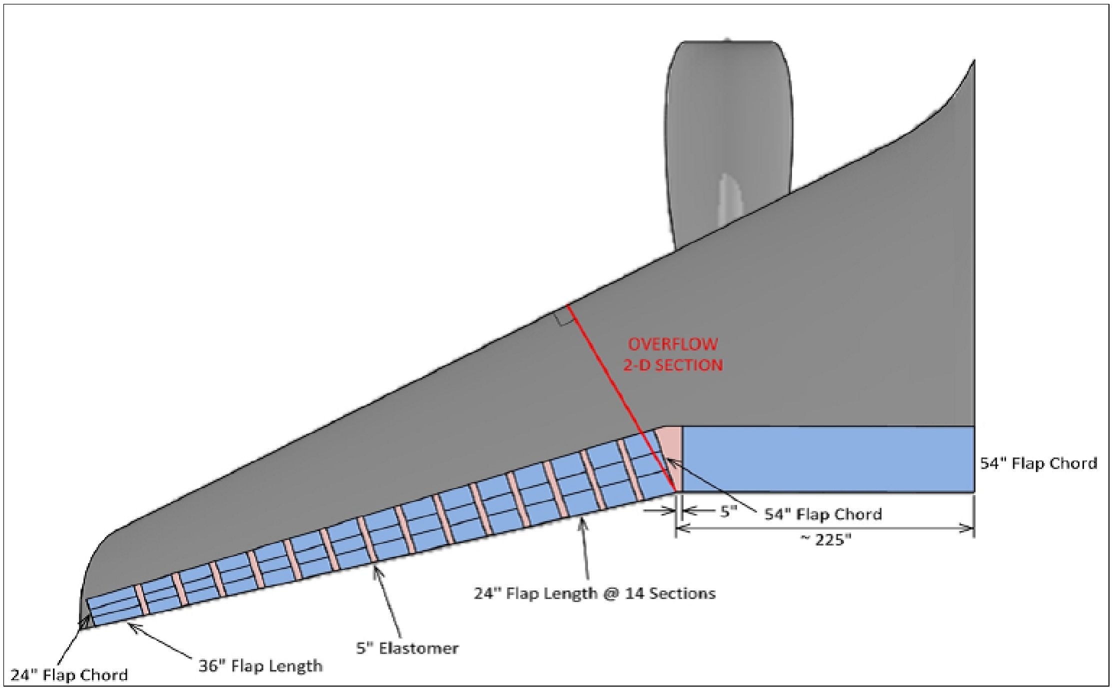

Figure 1.4: VCCTEF deployed on a generic transport model (GTM) [4]

the span the flaps are divided into segments of 2 feet, this allows each flap along the span to have a different setting. Hence, a twist of the wing is a function of the span, resulting in a different twist for each mission (Take-off and landing, cruise etc.), achieving the best lift-to-drag (L/D) ratios.

Figure 1.5 shows a schematic representation of the outer wing flap section, each having three camber components. First and second camber flap segments are driven by SMA actuators; while the third one is driven by an electrical motor that can act fast. With a slow rate of deflection, SMA actuators can deliver large hinge moments. To suppress the aeroelastic wing structural dynamic modes, outer wing flap is used as a control device and a roll command effector. The full span of the third segment of outer wing flap is used for this purpose and to deflect it at a higher rate an electric actuator is used[12] [13]. VCCTEF along with the

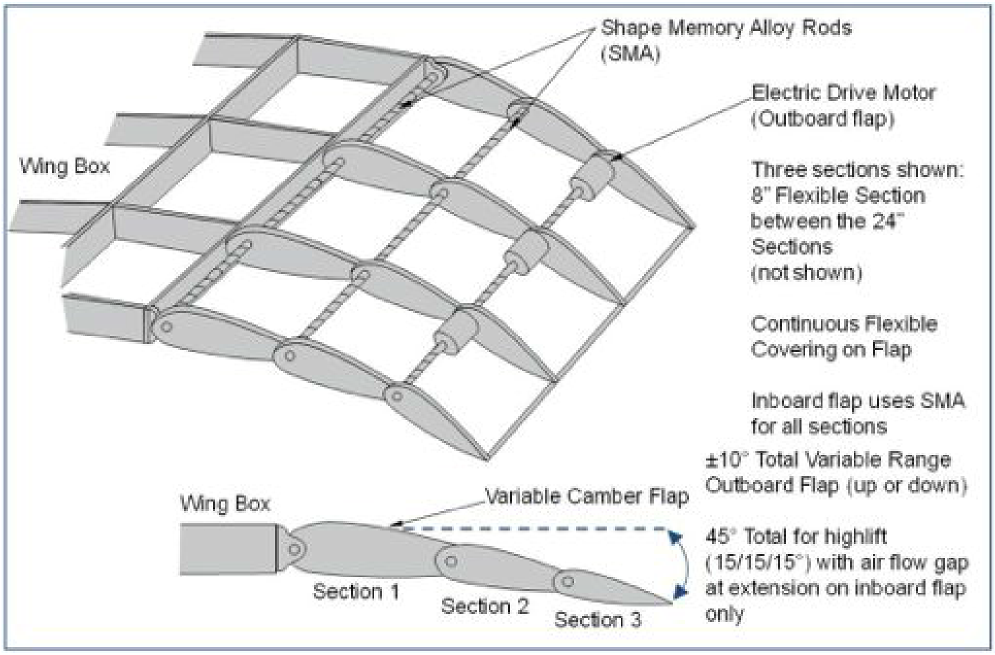

Figure 1.5: The Variable Camber Flap Control uses Shape Memory Alloy Torque Rod and Electric Drive Actuation [12] [13]

truss-braced wings has also proven to be a promising concept in weight reduction [14].

1.3 Present Approach

1.3.1 Wing of Advanced Technology Regional Aircraft(W-ATRA)

In the present study,the wing of advanced technology regional aircraft (W-ATRA) is taken from the work of Edi et al. [1] shown in Figure 1.6.

Three airfoils are used, while creating the above geometry namely root wing Side of the body (SOB), Inboard (INB) and Outboard (KINK) airfoil. In order to have an easier design process, the outboard wing profile is maintained constant.

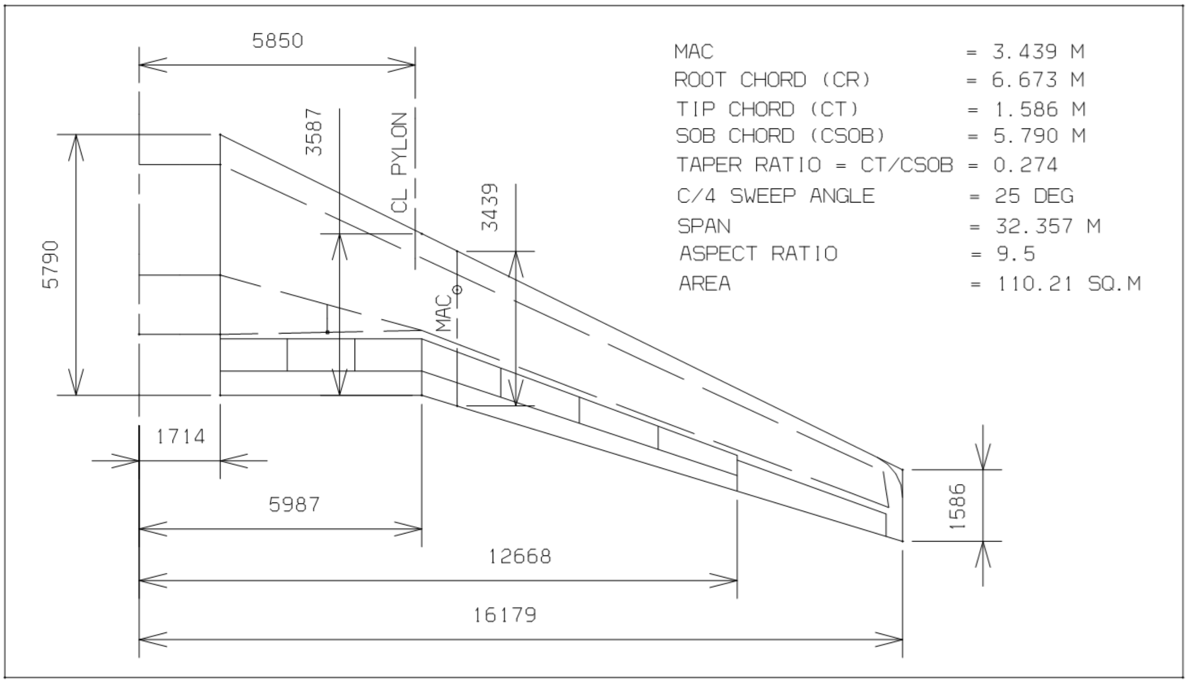

Figure 1.6: Geometric details of a ATRA wing [1]

This profile has the least thickness to chord ratio among the three. It has a max thickness of 9.1% at 40.2% chord,the max camber of 1.5% at 77.8% chord. Fig. 1.7 shows the variation of the wing twist and wing thickness from the wing root to the wing tip.

The outboard airfoil is at a distance of 5.987 m from the centerline of the fuselage, the airfoil incidence at this profile is 1.1° and thickness to chord (t/c) ratio is 9.23%. Same t/c ratio is maintained, until the wing tip, however, the angle of incidence varies linearly until $-2°$.

1.3.2 Addition of VCCTEF to W-ATRA

After discussing the W-ATRA in above section, a question arises, what portion of the wing should use the VCCTEF configuration? Should it be used over the

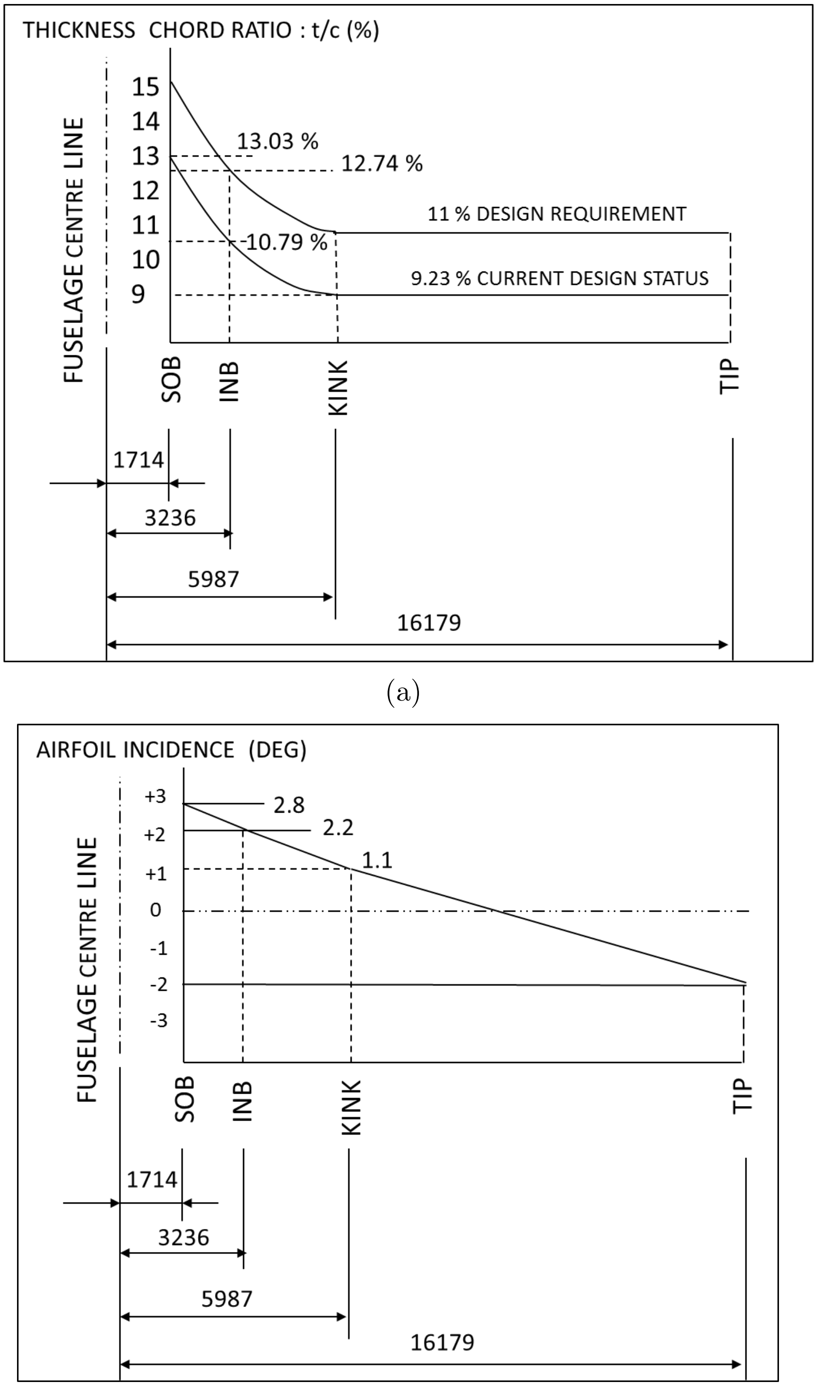

(a)

(b)

Figure 1.7: W-ATRA (a) thickness distribution (b) twist distribution [1]

entire span or until a certain position along the span?

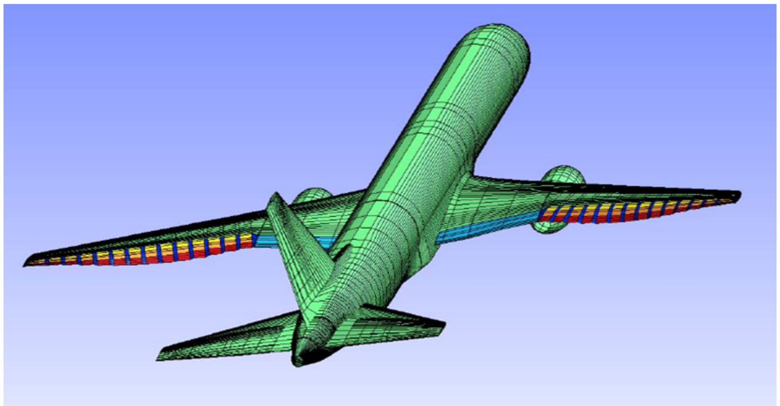

Figure 1.8: Complete VCCTEF configuration over GTM

As shown in Fig. 1.8, VCCTEF configuration is used after the wing break section (i.e. position where initial continuity in the wing is lost). Outboard/kink airfoil is used for making ATRA wing after the wing break section, which is the reason why only outboard airfoil is used with different VCCTEF configuration in the present study.

Table 1.1: VCCTEF configurations in study [4]

VCCTEF Configuration	number of segments (n)	Flap 1 (deg)	Flap 2 (deg)	Flap 3 (deg)
VCCTEF 123	3	1	2	3
VCCTEF 222	3	2	2	2
VCCTEF 321	3	3	2	1
VCCTEF 33	2	3	3	-
VCCTEF 6	1	6	-	-

Table 1.1 shows the various VCCTEF configurations on which simulations are done. All the configurations sum to 6°, for example, VCCTEF 123 is $1^\circ+2^\circ+3^\circ=6^\circ$. One of the reasons for taking this angle of 6° is, Kaul et.al [4] has done work on these configurations, but with another wing section of GTM wing. Another

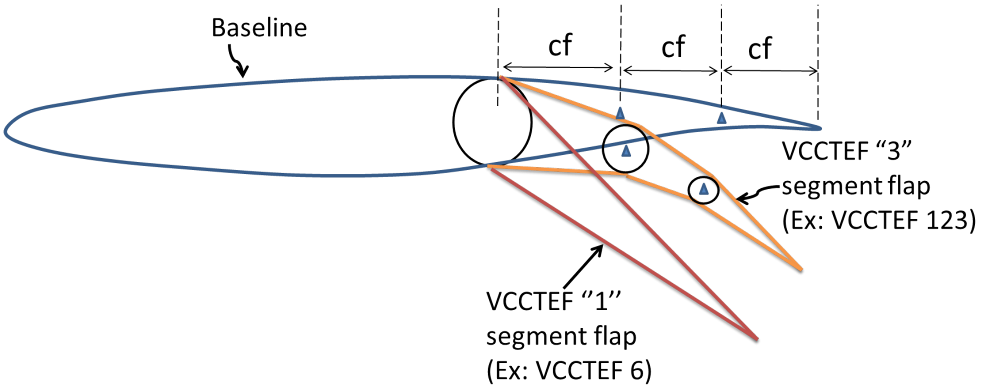

Figure 1.9: Schematic of VCCTEF 3 & 1 segment flap

reason, is that the fixed wings are designed based on the cruise segment and the present computations are done for the cruise segment, in which there is little incidence angle of the wing section. Thus, it will be interesting to see how the wings will behave at relatively higher wing incidence angles.

Fig. 1.9 shows the schematic of a three segmented flap each having flap chord length (cf). Since the total flap length is 30% of the chord(c), each cf is 10% of the total chord length. The baseline is the configuration in which there are no flap deflected. VCCTEF 123 implies that there are three segments of flap and the first segment is deflected at 1° relative to the horizontal line, the second segment is deflected at 2° relative to the first segment and the third segment is deflected at 3° relative to the second segment. The same applies for VCCTEF 222 and VCCTEF 321. For VCCTEF 33 configuration, there are two segments each deflected at 3° with respect to the horizontal and first segment respectively. VCCTEF 6 is a variable camber flap with single deflection of 6° with respect to the horizontal.

An aircraft's flight from take-off to landing involves various maneuvers such as climb, descent, cruise, rolling and banking, etc. Cruise is the longest flight segment, during which aircraft usually travels straight at constant altitude. The commercial airliners want to use less fuel during this flight segment. A steady straight and level flight provide the optimum condition to use less fuel with increased range and endurance. ln steady straight and level flight Thrust (T)= Drag (D) and Lift (L) = Weight (W). Flight conditions that help to achieve the steady straight and level flight are speed =constant; AoA = constant and dynamic pressure = constant along with the flight path angle (γ) = 0. The constraints that apply to steady level flight are $\alpha < \alpha_{max}$ and T<T_{max}[15]. During cruise if flight path angle(γ) is not equal to zero, then we loose the straight and level flight. For a slightly positive flight angle(γ) the optimum conditions are acquired by keeping the velocity and AoA constant[16]. The main benefit of VCCTEF is that the wing can always have optimum L/D for different C_l at constant AoA (cabin floor attitude constant). This is done by optimizing spanwise camber distribution (by VCCTEF deflections) in order to have optimum spanload distribution (elliptical) which have minimum induced drag . Thus, the flow can be maintained steady during the cruise for optimum fuel consumption.

The present study on the outboard airfoil of ATRA wing is for the cruise segment during which flow is expected to have steady laminar-transition-turbulent flow (on design). Computational study on outboard/kink airfoil is done at an altitude of 10,000 m, Mach number (M) equal to 0.7 and Reynold's number (Re) equal to 21.6 million. In case the wing can not develop laminar flow (off-design), the flow will be fully turbulent. To find the performance in this worst condition a study for turbulent flow is also included.

1.4 Objectives

The objectives of the present work are,

1. To reduce the aircraft's fuel consumption and thereby lessen the impact on the environment due to harmful emissions.
2. To improve the cruise aerodynamic efficiency (L/D) of an outboard airfoil of ATRA wing compared to the baseline.
3. To identify the VCCTEF configuration that has the highest L/D ratio.

1.5 Thesis Outline

This thesis is organized in a total of 6 chapters and their brief content is illustrated below,

Chapter 1 discusses the introduction and objective along with the aerodynamic and cost motivation. A brief background of the VCCTEF and W-ATRA is discussed.

Chapter 2 addresses the literature review briefly on laminar flow control techniques and comprehensively upon VCCTEF. This chapter highlights the gaps in the previous research and importance of the present research work.

Chapter 3 gives detailed study on the governing equations of fluid flow. How the averaging of Navier-Stokes equations leads to the turbulent closure problem is presented. Turbulence models are described briefly that solves the issue of turbulent closure. A numerical method for discretization i.e. finite volume method is briefly presented. The formulation of theoretical lift increment is also presented.

Chapter 4 deals with the guidelines for generating the mesh and the considerations for a near wall grid. NACA 0012, NACA 63209 and RAE 2822 experimental results are discussed. A method of creation of the geometry of NACA 0012 airfoil, NACA 63209, RAE 2822, outboard airfoil and various VCCTEF configurations is presented along with the grids generated for these airfoils. Finally, the flight and boundary conditions are discussed.

Chapter 5 contains the results and discussions of fully turbulent flow on various grids that are generated and shown in chapter 4. A comparison of computational and theoretical lift coefficient increment is also discussed.

Chapter 6 presents the results and discussion of flow having laminar transition and turbulent zones using Transitional k-kl-omega model. A comparison of computational and theoretical lift coefficient increment is again studied.

Chapter 7 concludes the work highlighting the future work and recommendations in this area.

CHAPTER 2

LITERATURE REVIEW

2.1 Review of previous work

To enhance the flow dynamics over the wing of an aircraft, a variety of methods can be used. One can either change the geometry of the wing section or introduce ingestions for boundary layer control. These methods focus on having better aerodynamic efficiency. Earlier in Sec. 1.1.1, it was seen that aerodynamic efficiency is lift to drag ratio (L/D) thus, the increment in it can be achieved by increasing lift or reducing drag or achieving both.

Drag comprises of two major components; pressure and viscous drag. Reducing either of them can reduce the overall drag. On a subsonic transport aircraft, viscous drag can be 50% of total aircraft drag [17] [18] [19]. The various methods by which one can reduce drag includes Laminar flow control (LFC) , Natural laminar flow (NLF) and Hybrid Laminar flow control (HLFC). These methods tend to delay the transition point and reduce the skin friction drag. In another method, turbulent skin friction can be reduced by the manipulation of turbulent boundary layer [20]. Devices such as Riblets [21] and Large Eddy Break-Up Devices (LEBUs) [22] can be used for this purpose. Riblets have V-shaped grooves that are longitudinally aligned along the stream. In LEBUs, wing-like devices which are surface-parallel, is used to periodically streamwise the boundary layer flow. Riblets are more important than LEBUs [23] and have been studied widely [24] [25]. Though both of these devices reduce drag, however the increased cost of manufacturing and maintenance is a concern [18] .

Vortex generators re-energize the boundary layer (by generating vortices) for delaying the separation. But, the use of vortex generators cause frictional and vortex drag. An advancement of it is a smart vortex generator that produces lesser drag than its previous counterpart. Smart vortex generator uses small vortex generating devices. Both mechanical [26] as well as pneumatic[27] devices with small jets are proposed for smart vortex generator. A more recent study on Vortex generators suggests that drag is sensitive to increase in Vortex generator's height than lift and increment in the length of generator reduces lift and increases drag [28]. An experimental study has not shown any improvement in the flow with the help of vortex generators. [29].

Drag reduction can also be achieved by altering the flow behavior by the use of additives such as particle, surfactant, bubble and polymer solutions [30].

Reduction in drag by the use of aforementioned methods (local skin friction drag reductions of 5-30%) is of considerable importance, but it is not as high as

LFC (50-80% reduction in skin friction drag).

Laminar flow control techniques (LFC) tend to delay the transition point, keeping the flow laminar for a certain portion of the wing. The start of use of this technique dates back to 1930 [31]. By use of LFC, one can keep the flow laminar in the regions which are generally termed as transitional or turbulent in the absence of LFC. The considerations that are to be taken for the use of LFC include manufacturing tolerance and insect contamination. Natural laminar flow (NLF) technique changes the shape of the airfoil such that thickest point of the airfoil is as aft as possible and is less thick [32].

HLFC is proved to be significant in the development of Laminar flow control (LFC) [31]. The advantages of the airfoil design, based on the HLFC criteria surpasses the limitations of Natural Laminar Flow (NLF) and Laminar Flow Control By Suction (LFCS). It has a good design performance in turbulent mode [31]. It also reduces the system complexity and cost relative to the NLF and LFCS [33]. A drag reduction of 10 - 11 % is expected to be reached by this approach [2]. For small aircraft having Reynold's number up to 20 $\times 10^6$ and low sweep angle of wing ($< 20°$) , one can achieve laminar flow by use of NLF technique (i.e.shaping the airfoil). However at higher sweep angle in addition to rapidly falling pressure (steep initial gradient) given by NLF (which is helpful in preventing attachment line transition [34]), a suction at the leading edge is needed [19]. This shows the need of HLFC technique compared to NLF in large transport aircraft.

Practical use of HLFC requires that laminar flow is maintained through a range of cruise lift coefficients and Mach numbers. There can be a loss of laminar flow if there is variation in lift coefficient and Mach number because of the change in the designed pressure distribution. Another method, that can be employed along with the HLFC must be studied to make the pressure distribution similar to that of designed for optimum benefit.

The deflection of Variable camber (VC) can keep the pressure distribution over the forward part of the airfoil similar to the design pressure distribution, although the C_l and M_∞ will differ from design values[2]. Variable camber is nothing but the deflection of the flap at a lower angle. With careful design of a VC flap, one can reduce the wave drag penalty and sustain attached flow in the turbulent mode [3].

Methods based on the combination of Hybrid Laminar flow control (HLFC) and variable camber for the improved performance of the wing during the cruise can be adapted in order to develop a methodology for the design of the transonic transport aircraft wing from an aerodynamic perspective. Design of an airfoil and twist distribution along the span can be done in SWEPTDES [1] [35]. ATRA wing is designed on the principle of the HLFC using the airfoils and twist distribution generated with above method. This wing upon the analysis in RAMPANT has shown that a combination of HLFC - VC wing technology is feasible for a transport wing, however, large effort is needed to demonstrate it for flying. The efforts in this direction are made for a reduction in fuel cost.

Modern, long-range wide-body transport aircraft can have up to 50 % of its total expenses due to the fuel cost. If one can reduce the consumption of fuel by 3%, there can be a saving of $ 300,000 in a year[9]. Less fuel corresponds to fewer emissions. The future growth of the aircraft industry depends on various environment factors such as air pollution and noise [36]. In aircraft design, the effect on environment plays a huge factor. European commission launched vision 2020 which aimed to have a cut of 80% in emissions of nitrogen oxide and 50% in CO_2 emissions/ passenger kilometer (this implies a 50% reduction in consumption of fuel by 2020 in new aircraft) . Although there are significant savings due to drag reduction with HLFC; it is not just about the drag reduction.

Boeing 787-9 was the first Boeing aircraft to have HLFC in its tailplane and fin [37] in the year 2014 after it began flight testing in 2011[38]. By the year 2015, news of Boeing ditching the HLFC on 777X started coming and 787-9 was under review. The reduction in drag due to HLFC did not justify its inclusion in 777X [39]. There may be various reasons for it. The reduction in drag has to justify the additional cost it brings. The weight of its mechanism, manufacturing and maintenance cost could potentially dampen the benefits that HLFC brings along with it. To solve this problem one has to look for breakthrough methods/techniques that bring weight and cost reduction along with them or, at least, their inclusion will bring the benefits that surpass other liabilities that come along with them. NASA took a lead role in green aviation, an initiative via. which new aviation systems are developed that can take the challenge of improvement in environment-friendly and lesser fuel consuming aircraft. A report entitled "Elastically Shaped Air Vehicle Concept (2010)" is the finding of NASA Innovation Fund project [5]. The report presented some revolutionizing concepts that are realizable. The lightweight composite airframe designs have a good load carrying capability, structural rigidity and they have relatively higher flexibility compared to their previous counterparts. A very good example is Boeing 787 Dreamliner Aircraft. Methods or new systems/techniques can be developed to leverage aerodynamic efficiency with this high flexibility. Elastically shaping airframe designs are inspired by birds. During flight with the use of control systems, high flexible wings can be shaped elastically such that wing will twist, thus, changing its local AoA (required according to the flight segment) causing lesser drag and hence less fuel consumption. Structurally flexible wing can help to get a better drag reduction compared to straight wing designs. Three new themes are developed in this report,the first theme proposes three new concepts, which are,drooped wing (5.3% drag reduction) , squashed fuselage drooped wing (15% drag reduction) and inflicted wing (3.5% drag reduction) vehicle concepts. The second theme addresses the issue of the adverse effect of aeroelastic wing shape on drag. The advancement in the flexibility of the wings causes more deflection than their predecessors. To understand this, let's see this example, Boeing 777 and 787 have almost similar wingspans, which is approximately 200 feet [40] [41] [42]. Boeing 787 is an all-composite wing, whereas, its predecessor 777 is an all-alloy wing. Tip deflection of 787 is 10% [43] of its semi-span, whereas, 777 has tip deflection of 6.4 ft [44] or 3.2% of its semi-span. Therefore, the second theme proposes the use of active controls, aero elastically changing the wing shape.

Compared to drooped wing concept proposed in the first theme, a 17% drag reduction can be achieved by the second theme. In order to realize this fully, a third theme is presented in which new type of control surfaces are developed that are referred to as Variable Camber Continuous Trailing Edge Flap (VCCTEF). The conventional flaps or other control surfaces are independent of one another and have discontinuities in between them. VCCTEF overcomes these problems and gives up to 50% drag reduction compared to conventional flaps/control surfaces by not having a discontinuity in control surfaces [6].

A second study [45] in 2012 was conducted jointly by Boeing and NASA Subsonic Fixed Wing (SFW) project. The study for the development of VCCTEF on an airframe similar to B757 [46] i.e. on NASA Generic Transport Model (GTM) suggested that, for actuation, lightweight shaped memory alloy (SMA) are to be employed as they have the advantage of lightweight. The geometry of the flap was determined and the flap was divided into three segments along the chord for varying camber. This study was further developed in 2013 [12] together with Boeing and NASA under research element Active Aeroelastic shape control (AASC) with the aim to optimize the high lift and cruise lift to drag ratios. A VCCTEF system was designed and the flaps were divided into 2-foot segments along the span allowing to have a different twists for different flight segments.The least amount of induced drag is generated from the elliptical wings as they can have elliptic wing loading and during cruise VCCTEF can achieve elliptic wing loading via.

change in twist.The additional benefits VCCTEF brings along with the use of aeroelastic change in wing shape, can not be achieved by conventional flaps. The weight reduction, that comes along with the use of shape memory alloy augmented with electric actuator [47], is an advantage over the conventional flap screw jack actuators.

Experimental investigation of VCCTEF on GTM was performed in 2014 [13]. The tests were conducted in Univerity of Washington Aeronautical Laboratory (UWAL) upon a 10% scaled model. For having flexibility, the model was constructed with foam core and woven fabric composites. One of the main features of the VCCTEF is the elastomeric material that is used to fill the gaps between the flaps. This material makes the trailing edge flap continuous. The results indicated an increment of L/D ratio by 4.85% and drag reduction by 6.31%. The experiment was performed in low-speed incompressible flow conditions. Further investigation was needed before fully accessing the benefit of VCCTEF in high speed. Kaul et.al [4] addressed this by the computational analysis on the airfoil of NASA GTM. The simulations were performed at higher Mach number having fully compressible flow regime. The VCCTEF flap having 1, 2 and 3 segments were tested and it was found that compared to other flap segments, VCCTEF segment having circular arc gives the best aerodynamic efficiency (L/D ratio) compared to other segments. All the simulation that were performed are fully turbulent. It was also seen that as the AoA increases, the pressure component of the drag increases and the contribution of the viscous component of drag becomes less. Kaul et.al has asserted that, increase in wing flexibility has a negative impact on the aerodynamic efficiency, as flexible wing aeroelastic interaction with aerodynamic moments and forces can alter aerodynamics on the wing. This can be avoided with the active control of high flexible wing's vertical bending and twist by elastically shaping the aerodynamic surface of the wing.

Hence, the aeroelastic analysis of a flexible wing in a wind tunnel is of extreme importance. This study is presented by Nguyen et.al [48]. A low-cost model was used for the study, parts of which were made with three-dimensional (3-D) printing. This study suggests that lift curve slope is a better indicator for comparing lift prediction. This is because any uncertainty in deflection of VCCTEF can cause a constant offset in the coefficient of lift. This study was done with the same model upon which earlier experimental study showed an increment of L/D ratio by 4.85% and drag reduction by 6.31%. An aeroelastic testing program for low-cost and low-speed wind tunnel is developing at the University of Washington for the infrastructure, design methods and mathematical modeling done by NASA and Boeing [49]. In addition to the outer VCCTEF, fowler flap and leading edge slats were added to the wing. This can be said, as the Phase II for VCCTEF having an aim of developing the experimental database for the validation of mathematical modeling done by NASA. The results of aerodynamic efficiency (L/D ratio) vs. AoA, show that at lower AoA (0°-2°), L/D ratio is maximum in cruise. Because of the limitation of budget and schedule, the experimental studies were conducted based on the two-dimensional (2-D) design of the flaps. Hence, one can never underestimate the importance of 2-D analysis,as, a large amount of information can be abstracted from them. However, tuning of the design using experimental study is a must.

An experimental study with VCCTEF on NASA GTM flexible wing high lift configuration was performed in UWAL [29]. In addition to the VCCTEF on the outboard airfoil, high lift devices were added which include a trailing edge flap with fowler motion and a leading edge device, Variable Camber Krueger (VCK). The inboard flap which was having fowler motion was tested with two flaps; one having the plain flap and the another one having the three segment cambered flap . The outboard VCCTEF flap had no fowler motion. Instead, it was dependent on the actuating mechanism of Shape Memory Alloy (SMA) and electric motors. A reason for not giving the fowler motion in outboard airfoil is the addition of weight due to the flap track mechanism and the fairing cover. This has the potential to reduce the overall benefit of VCCTEF. This study was for high lift configurations at Mach number 0.067 and Reynold's number 8.9 $\times 10^5$. A 2-D analysis was performed to design the flap, based on the results of which wind tunnel testing was done on the designed flaps. The study showed that cambered flaps achieved a C_{Lmax} of 2.09 compared to 2.13 of the plain flap and an increase in L/D by 6%. By proper design of a control system and keeping the constraints of actuation mechanism, the benefit of VCCTEF can be optimized [50] [51] [52]. The use of vortex generators did not give any improvement in the flow. In fact, rigging the slats helped in attaining the required performance. This study was for high lift configurations, but it can also give an insight of how the flow will behave during the cruise in which slats or vortex generators are usually not used. During cruise, in order to simplify drag reduction technique, the best viable option is VCCTEF. In this flaps are made continuous by the use of elastomer. To study the effect of various elastomers VCCTEF 222 was selected based on the previous 2-D study of Kaul et.al.. Four different types of elastomer were studied and all of them obtained a similar L/D ratios,which were less then the previous 2-D results[53]. Upon viewing the trend, it was seen that 2-D and 3-D results followed a similar trend. However, the presence of 3D relief effect, made the pressure rise due to shock, gradual rather than sudden.

The aerodynamic loads on the wing will deform the shape of the wing. After finding these aerodynamic loads, the shape of the deformed wing is obtained, using aeroelastic analysis. Instead of doing this work alternatively, a viscous code solver (Overflow) was integrated with an existing framework used for aeroelastic analysis [43]. Initially, a deformed wing shape was found based on the aerodynamic loads developed from Cart3D (inviscid solver) and then using Overflow, aerodynamic loads of deformed shape were found. This study showed that it is twisting and not bending that is causing a decrease in the lift for AoA $< 16^\circ$. However, lift increases for AoA $> 16^\circ$ [54]. This study was done for high lift configuration at lower Mach number. For Cruise, the study has to be at higher Mach number. But the result seems to give us insight into the reason of lift reduction with flexible wings. Another problem with highly flexible wings is flutter due to reduced stiffness. Controllers for VCCTEF are subjected to many constraints and they must be designed for optimal parameters taking into consideration, the wing disturbances for drag minimization. This work is done by a project entitled Drag Identification and Reduction Technology (DIRECT), which on-line estimates the state of aeroservoelastic and uses the information to suppress flutter [55] .

The use of VCCTEF can be extended to formation flight to improve cruise aerodynamics [56] by 1.5 - 2.5% reduction in induced drag causing a block fuel savings of 0.64%.

2.2 Conclusion

A lot of work is being done towards a clean environment by achieving the reduction in fuel consumption. Increasing the aerodynamic efficiency (L/D ratio) during the cruise can increase the fuel efficiency, thus minimizing the fuel consumption. Less fuel consumption implies little emissions. Increasing lift inherently increases drag. Thus, the major focus is towards a reduction in drag by various techniques. HLFC - VCW technique has the potential of drag reduction but the recent advancement in composite materials has developed less stiffness and high flexible wings. This interacts with the aerodynamic forces and moments causing a reduction in lift and increase in drag. Active control of bending and wing twist in high flexible wings can be done by elastically shaping the aerodynamic surfaces. Since conventional flaps inherently increase drag with increase in lift, new type of control surfaces are developed i.e. VCCTEF which is currently studied on NASA GTM turbulent wing. ATRA wing is designed on HLFC criteria but does not use VCCTEF on the outboard airfoil. A combination of wing section designed on HLFC criteria (outboard airfoil of W-ATRA) and VCCTEF is not done until now, since the inception of VCCTEF in 2010. This gives us an opportunity to study this topic.

CHAPTER 3

RESEARCH METHODOLOGY & THEORETICAL LIFT INCREMENT

3.1 Introduction

Turbulence consists of random fluctuations in various properties such as velocity, density, pressure and temperature. For this reason, the DNS (Direct Numerical Solutions) approach requires a very fine mesh. For a channel flow, a number of grid points required can be obtained from the expression [57].

$$N_{DNS} = (3Re_{\tau})^{\frac{9}{4}} \tag{3.1}$$

N_{DNS} : number of grid points required

If turbulent Reynolds number (Re_τ) = 10^4, then a number of grid points required are 30^9, which is a very fine mesh and hence increasing Re_τ more can increase computational time more. In order to solve the aforementioned problem all the properties can be expressed as the sum of fluctuating and mean parts, this gives time-averaged Navier-Stokes equation. This procedure was introduced by Reynolds in 1895 and is a statistical approach. Five governing equations(one continuity, three momentum, one energy) and an ideal gas equation forms a group of six equations that can be solved to get six unknowns (P,T,ρ,u,v,w,). However, Reynolds averaging leads to additional terms and these additional terms needs additional equations which are given by Turbulence modeling. The problem of defining a number of equations for the number of unknowns is referred to as closure problem. In this chapter, the basics of Reynolds and Favre‘s averaging are described. The governing equations and its averaged form are included along with turbulence modeling. Fig. 3.1 shows the flow chart for the topics that will be covered in research methodology.

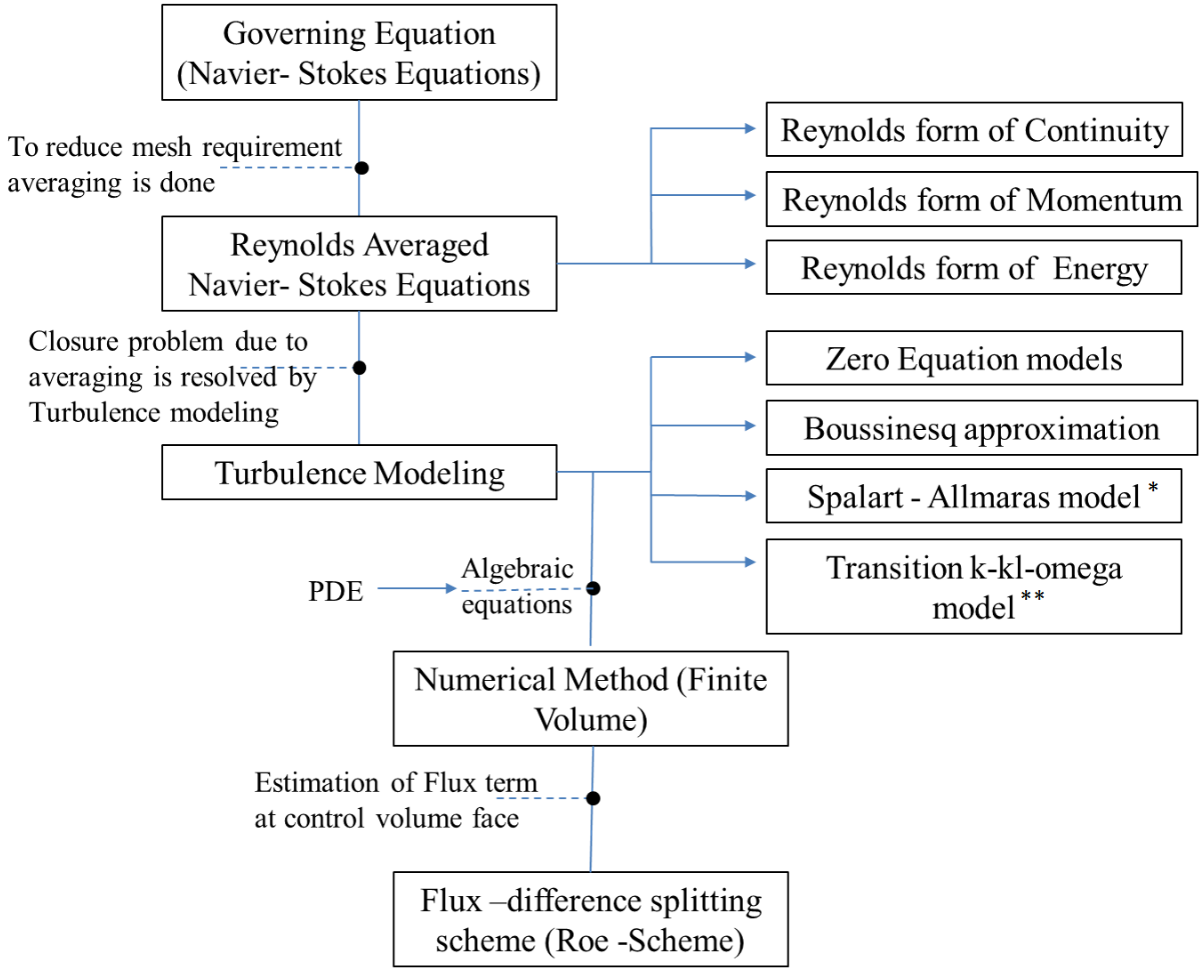

Figure 3.1: Flow Chart for the topics in Research Methodology

.

* Fully turbulent simulations are performed using Spalart-Allmaras model.

** Transition simulations are performed using Transition k-kl-omega model.

3.2 Navier-Stokes equations

Tensor notation for compressible flows of the instantaneous continuity, momentum and energy equations are written as,

$$
\begin{aligned}
\frac{\partial \rho}{\partial t} + \frac{\partial}{\partial x_i}(\rho u_i) &= 0 && (3.2) \\
\frac{\partial}{\partial t}(\rho u_i) + \frac{\partial}{\partial x_j}(\rho u_i u_j) &= -\frac{\partial p}{\partial x_i} + \frac{\partial t_{ij}}{\partial x_j} && (3.3) \\
\frac{\partial}{\partial t}[\rho(e + 1/2 u_i u_i)] + \frac{\partial}{\partial x_j}[\rho u_j (h + 1/2 u_i u_i)] &= \frac{\partial}{\partial x_j}(u_i t_{ij}) - \frac{\partial}{\partial x_j} q_j && (3.4)
\end{aligned}
$$

Here ρ is the density of fluid, p is the pressure, u_i is instantaneous velocity in the i direction (i = 1, 2, 3), and t_{ij} is the Viscous shear stress acting on a fluid element, e is Specific internal energy, h=e+p/ρ is Specific enthalpy, and q_j is the Scalar heat flux. The Left Hand Side (LHS) of Eq. 3.2, 3.3 and 3.4 represents the unsteady and convective transport terms. The terms on Right Hand Side (RHS) of Eq. 3.3 represent the pressure forces and viscous forces. The first term on RHS of Eq. 3.4 gives the work done due to shear stress, where t_{ij} is governed by Newton‘s law of viscosity as,

$$
t_{ij} = 2\mu s_{ij} - \zeta \frac{\partial u_k}{\partial x_k} \delta_{ij} \qquad (3.5)
$$

wherein s_{ij} is instantaneous strain rate tensor and ζ is second viscosity. The ζ is related to molecular viscosity μ as ζ = -2/3 μ, where the molecular viscosity μ variation with temperature is calculated from Sutherlands formula [58] of viscosity (for air) as,

$$\mu = [\frac{(1.45 \times T^{6/2})}{(T + 110)} \times 10^{-6}] \tag{3.6}$$

Here T is temperature in Kelvin and δ is the Kronecker delta function defined as $\delta_{ij} = 1$ if i = j and $\delta_{ij} = 0$ if $i \neq j$. The second term in RHS of Eq. 3.4 represents the heat flux due to conduction and is calculated from Fourier's law as,

$$q_j = -\kappa \frac{\partial T}{\partial x_j} = -\mu \times Pr_L \frac{\partial h}{\partial x_j} \tag{3.7}$$

where κ is thermal conductivity of the fluid and the Prandtl number is given as $Pr_L = C_p\mu/\kappa$. In many fluid flow cases, the intermolecular forces between the molecules are neglected and the fluid is assumed to be a perfect gas which satisfies the following equation of state.

$$p = \rho RT \tag{3.8}$$

$$e = C_v T \tag{3.9}$$

$$h = C_p T \tag{3.10}$$

where R is characteristic gas constant, C_v and C_p are the specific heats at constant volume and pressure respectively. The characteristic gas constant can be expressed as the ratio of universal gas constant R, and molecular weight M, of gas as, $R = \overline{R}/M$. The universal gas constant has same value of 8.314 J/(K mol) for all gases. The value of R is different for different gases and for air its value is equal to 287.1 J/K.

3.3 Reynolds averaging

Reynolds decomposition is given by the Eq. 3.11 in which mean terms that are given by a bar on their top (first term in the RHS) are separated from the fluctuating term (second term in the RHS). The decomposition of fluctuating quantity $u_i(\vec{x}, \vec{y}, \vec{z}, t)$ would be,

$$u_i(\vec{x}, \vec{y}, \vec{z}, t) = \overline{u}_i(\vec{x}, \vec{y}, \vec{z}, t) + u_i'(\vec{x}, \vec{y}, \vec{z}, t) \tag{3.11}$$

where,

$\overline{u}_i(\vec{x}, \vec{y}, \vec{z}, t)$ denotes the mean component or steady component (remember the time average of the mean component is mean component itself) , and $u_i'(\vec{x}, \vec{y}, \vec{z}, t)$ denotes fluctuating part (or perturbations). The time average of perturbations is equals zero.

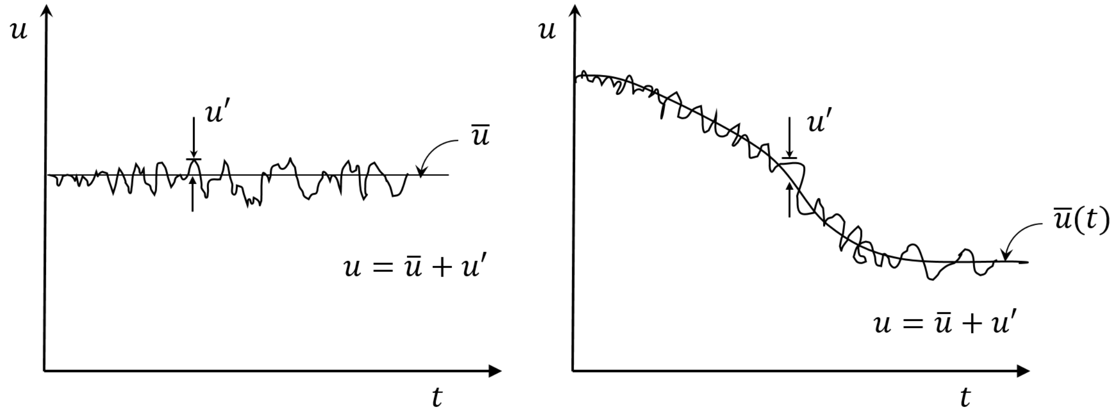

(a)

(b)

Figure 3.2: Relation between u, $\overline{u}$, u' in a (a) Steady (b) Unsteady turbulent flow

Fig. 3.2 shows that in both steady and unsteady flow the summation remains same. If the flow doesn't change with time then the flow is said to be steady and if it changes with time than the flow is said to be unsteady. The bar term or steady component is given by Reynolds averaging. Averaging concepts were introduced by Reynolds in 1895, which assumes a variety of forms involving summation or integrals. Three forms most relevant in turbulence model research are:

1. Time Average (Inhomogeneous turbulence)
2. Spatial Average (Homogeneous turbulence)
3. Ensemble Average (General type of Averaging)

Time Averaging is a most appropriate for stationary turbulence i.e. a turbulence that on average doesn't change with time. For such a flow if instantaneous flow variable is expressed as $u_i(x,t)$,then its time average $\overline{u_i}(x,t)$ is defined by,

$$\overline{u}_i(\vec{x}) = \lim_{T\to\infty} \tfrac{1}{T} \textstyle\int_t^{t+T} u_i(\vec{x},t)dt \tag{3.12}$$

In real life, $T \to \infty$ means, the value of T is large relative to the max. period of velocity fluctuation .In conventional Reynolds decomposition, the Randomly changing flow variables are replaced by time averages plus fluctuations about the average. For a Cartesian system it can be written as,

$$\begin{gathered} u = \overline{u} + u', \quad v = \overline{v} + v', \quad w = \overline{w} + w', \quad p = \overline{p} + p' \\ h = \overline{h} + h', \quad T = \overline{T} + T', \quad H = \overline{H} + H', \quad \rho = \overline{\rho} + \rho' \end{gathered} \tag{3.13}$$

In addition to velocity and pressure fluctuations (no ρ,T fluctuations in incompressible), one must also account for density and temperature fluctuations when the medium is compressible fluid. Hence, the concept of mass-weighted averaging is introduced .

$$\tilde{u}_i(\vec{x},\vec{y},\vec{z}) = \tfrac{1}{\rho}\lim_{T\to\infty}\int_t^{t+T}\rho(\vec{x},\vec{y},\vec{z},t)u_i(\vec{x},\vec{y},\vec{z},t)dt \tag{3.14}$$

In Favre averaging the instantaneous variables are mass weighted averaged. For statistically steady and stationary compressible turbulence flow, the instantaneous variables are written as,

$$\begin{aligned} \tilde{u} = \overline{\rho u}/\overline{\rho}, \quad \tilde{v} = \overline{\rho v}/\overline{\rho}, \quad \tilde{w} = \overline{\rho w}/\overline{\rho}, \\ \tilde{h} = \overline{\rho h}/\overline{\rho}, \quad \tilde{T} = \overline{\rho T}/\overline{\rho}, \quad \tilde{H} = \overline{\rho H}/\overline{\rho}, \end{aligned} \tag{3.15}$$

While using Favre averaging, it is customary to decompose the instantaneous velocity u into the mass- averaged part $\tilde{u}_i$ and fluctuating part u''.

$$\begin{aligned} u = \tilde{u} + u'' \quad v = \tilde{v} + v'' \quad w = \tilde{w} + w'' \\ T = \tilde{T} + T'' \quad H = \tilde{H} + H'' \quad h = \tilde{h} + h'' \end{aligned} \tag{3.16}$$

3.4 Reynolds-Averaged Navier-Stokes equation

In this section Reynolds-Averaged form of various governing equations viz. continuity, momentum and energy are studied.

While in fluid mechanics, momentum equation is Navier-Stokes equation, in CFD all the governing equations are called as Navier-Stokes Equation. The basic thing here, for obtaining a Reynolds-Averaged form of an equation is to decompose the fluctuating quantities and then Reynolds average (Time average or mass weighted average) them .The time averaging of the fluctuating component is '0' i.e.

$$\overline{u_i'} = 0 \tag{3.17}$$

the same is applicable for all fluctuating quantities.However, one must remember that

$$\overline{u_i''} \neq 0 \tag{3.18}$$

the above equation is valid until $\rho' = 0$.

3.4.1 Reynolds form of the continuity equation

In the continuity equation, written in Cartesian coordinate system, first decompose the variable into the conventional time averaged variable plus fluctuating components as given by Eq. 3.13. The entire equation is time averaged , yielding continuity equation in conventionally averaged variables

$$\frac{\partial \overline{\rho}}{\partial t} + \frac{\partial}{\partial x_j}(\overline{\rho u_j} + \overline{\rho' u_j'}) = 0 \tag{3.19}$$

Substituting the mass weighted averaged variables plus double primed fluctuations given by Eq. 3.16 and after some mathematical calculations it can be written as,

$$\frac{\partial \overline{\rho}}{\partial t} + \frac{\partial}{\partial x_j}(\overline{\rho}\tilde{u}_j) = 0 \tag{3.20}$$

The Eq. 3.20 is in more compact form than(3.19). For incompressible flows $\rho' = 0$,and the difference between the conventional and mass-weighted variable vanishes, so that continuity can be written as,

$$\frac{\partial \overline{u_j}}{\partial x_j} = 0 \tag{3.21}$$

3.4.2 Reynolds form of the momentum equation

Upon starting the momentum equation in conservation law form and then substituting Eq. 3.13 and time averaging it,several terms get disappear and some terms are grouped together and made zero by use of continuity equation.

The complete Reynolds momentum equations (all three components) can be written as,

$$\frac{\partial}{\partial t}(\overline{\rho}\ \overline{u_i} + \overline{\rho' u_i'}) + \frac{\partial}{\partial x_j}(\overline{\rho}\ \overline{u_i}\ \overline{u}_j + \overline{u_i}\overline{\rho' u_j'}) = -\frac{\partial \overline{p}}{\partial x_i} + \frac{\partial}{\partial x_j}(\overline{\tau}_{ij} - \overline{u_j}\overline{\rho' u_i'} - \overline{\rho}\overline{u_i' u_j'} - \overline{\rho' u_i' u_j'}) \tag{3.22}$$

where,

$$\overline{\tau_{ij}} = \mu \left[\left(\frac{\partial \overline{u}_i}{\partial x_j} + \frac{\partial \overline{u}_j}{\partial x_i} \right) - \frac{2}{3}\delta_{ij}\frac{\partial \overline{u_k}}{\partial x_k} \right] \tag{3.23}$$

To develop the Reynolds momentum equation in mass-weighted variables, start with conservative form of momentum equation by Favre‘s decomposition as given by Eq. 3.16, upon substitution ,

$$\frac{\partial}{\partial t}(\overline{\rho}\tilde{u}_i) + \frac{\partial}{\partial x_j}(\overline{\rho}\tilde{u}_i\tilde{u}_j) = -\frac{\partial \overline{p}}{\partial x_i} + \frac{\partial(\overline{t}_{ij} - \tau_{ij})}{\partial x_j} \tag{3.24}$$

The first term in the RHS of Eq. 3.24 represents the pressure force and the second and the third term represents forces due to average viscous stress $\overline{t}_{ij}$ and Reynolds stresses term τ_{ij}, which are given as

$$\overline{t}_{ij} = 2\mu(S_{ij} - \frac{1}{3}\delta_{ij}\frac{\partial \tilde{u}_k}{\partial x_k}) + \mu\left[\left(\frac{\partial \overline{u_i''}}{\partial x_j} + \frac{\partial \overline{u_j''}}{\partial x_i}\right) - \frac{2}{3}\delta_{ij}\frac{\partial \overline{u_k''}}{\partial x_k}\right] \tag{3.25}$$

The second term in above Eq. 3.25 is so small that it can be neglected. Thus in Eq. 3.24 there is only one term in fluctuating variables given by Eq. 3.26 below,

$$\tau_{ij} = -\overline{\rho u_i'' u_j''} \tag{3.26}$$

The term S_{ij} is Favre Averaged strain rate expressed in terms of favre mean variable as,

$$S_{ij} = \frac{1}{2}\left[\left(\frac{\partial \tilde{u}_i}{\partial x_j}\right) + \left(\frac{\partial \tilde{u}_j}{\partial x_i}\right)\right] \tag{3.27}$$

$\delta_{ij} = 0$ when i$\neq j$ and

. =1 when i=j.

The term $\frac{\partial \tilde{u}_k}{\partial x_k}$ is the divergence term i.e.$\bigtriangledown.\vec{V}$

For incompressible flow, the momentum equation can be written in the simpler form

$$\frac{\partial}{\partial t}(\rho\,\overline{u_i}) + \frac{\partial}{\partial x_j}(\rho\,\overline{u_i}\,\overline{u_j}) = -\frac{\partial \overline{p}}{\partial x_i} + \frac{\partial}{\partial x_j}(\overline{\tau}_{ij} - \rho\overline{u_i' u_j'}) \tag{3.28}$$

where,

$$\overline{\tau_{ij}} = \mu\left(\frac{\partial \overline{u}_i}{\partial x_j} + \frac{\partial \overline{u}_j}{\partial x_i}\right) \tag{3.29}$$

It was noted earlier in continuity equation that, there is no difference between the mass weighted and conventional variables for incompressible flow

3.4.3 Reynolds form of the energy equation

$$\begin{aligned}\frac{\partial}{\partial t}(\bar{\rho}\tilde{E}) + \frac{\partial}{\partial x_j}(\bar{\rho}\tilde{u}_j\tilde{H}) \quad &= \quad -\frac{\partial}{\partial x_j}(q_{L_j}) - \frac{\partial}{\partial x_j}(q_{T_j}) + \frac{\partial}{\partial x_j}(\tilde{u}_i\bar{t}_{ij}) + \frac{\partial}{\partial x_j}(\tilde{u}_i\tau_{ij}) \\ &\quad -\frac{\partial}{\partial x_j}\overline{\rho u_i'' u_i'' u_j''} + \frac{\partial}{\partial x_j}\overline{(t_{ij}u_i'')} \end{aligned} \tag{3.30}$$

Here $\tilde{E}$ and $\tilde{H}$ represent the total energy and total enthalpy which are given as,

$$\tilde{E} = \tilde{e} + \frac{1}{2}\tilde{u}_i\tilde{u}_i + k \tag{3.31}$$

$$\tilde{H} = \tilde{h} + \frac{1}{2}\tilde{u}_i\tilde{u}_i + k \tag{3.32}$$

$$\tilde{e} = C_v\tilde{T} \tag{3.33}$$

$$\tilde{h} = \tilde{e} + \bar{p}/\bar{\rho} \tag{3.34}$$

where,

$$k = \frac{1}{2}\frac{\overline{\rho u_i'' u_i''}}{\overline{\rho}} \tag{3.35}$$

is the turbulent kinetic energy. The LHS terms of Eq. 3.20, 3.24 and 3.30 represent the transient and convective transport terms.

The first and second terms on RHS of Eq. 3.30 represent the conduction heat flux and turbulent heat flux. The conduction heat flux is calculated from Fourier's assumption of heat conduction which is given as,

$$q_{L_j} = -\frac{\mu}{Pr_L}\frac{\partial \tilde{h}}{\partial x_j} = -\frac{\mu C_p}{Pr_L}\frac{\partial \tilde{T}}{\partial x_j} = -\kappa\frac{\partial \tilde{T}}{\partial x_j} \tag{3.36}$$

and the turbulent heat flux vector is defined as,

$$q_{T_j} = \overline{\rho u_j'' h''} \tag{3.37}$$

In terms of mean variables the equation of state for perfect gas is expressed as

$$\overline{p} = \overline{\rho} R \tilde{T} \tag{3.38}$$

The above equations can be solved to obtain the mean flow variables, but these equations are not closed as described in later equations.

3.4.4 Need for turbulence modeling

The above section dealt with the Averaging and Decomposition concepts and they generate the Reynolds stress term and another fluctuating term. It is known that before averaging the equations (governing and ideal gas) and unknowns were 6/6.

The additional terms after averaging require additional equations, the question which arises now is how to obtain the additional equations. Let‘s find the answer in subsequent sections. The appearance of the Reynolds stress terms make the problem of turbulence more tougher, that’s because though it is a stress term but the physics of it different from viscous stress. One reason why they are different is, the relation between a viscous term and the other flow properties can be given by establishing equations, which are dependent only on the properties of the fluid. In the closure approximation, time scales and characteristic length average are smaller than those of the concerned flows and larger than the concerned length and scales, which describes the molecular interaction causing momentum transfer. This closure idea works well for the viscous term. Let us now look at the closure problem of the Reynolds stress term. The fluctuating terms of interest are the terms, that are giving rise to the Reynolds stress term (remember, this term arises from flow itself). Thus, the closure idea that drove for the viscous term does not suit for the Reynolds stress term and one can not form any equation further to predict the flow physics. One can not wait to see aircraft prototype being made and it fails, costing a huge sum. Also, that may involve lives of people working in it. If a turbulence model is made, that can predict the flow physics, so perfect that building of product is based on the results of it, this will save a lot of amount. However, one can not eliminate the use of wind tunnel.

3.5 Introduction to turbulence modeling

In this section, Boussinesq approximation and modeling of Eddy viscosity by various equation model will be discussed. The need for turbulent modeling was pointed out in an earlier section. In order to predict the turbulent flows with the help of numerical solutions to Reynolds-Averaged equations, it is necessary to make closing assumptions about the Reynolds stresses and Heat Flux quantities. Unfortunately, there is no turbulence model which can be said as complete for all the turbulent equations. An ideal turbulence model will be the one, which has an accuracy (fast solution + less time taken for convergence) in the limited conditions available. The Turbulence model must be verified by comparing with the experimental results and additional care has to be taken interpreting predictions of the models for defining new conditions which are not experimented and can't be verified with experimental results. The purpose of this section is to present the terminology used, various models such as zero, one and three equation models and the limitations of these models.

3.5.1 Turbulent closure

Boussinesq (1877) suggested that the Reynolds shear stresses might be related to the rate of mean strain through an apparent scalar turbulent or eddy viscosity. For the general Reynolds stress tensor, the Boussinesq assumption gives,

$$\tau_{ij} = -\overline{\rho u_i'' u_j''} = 2\mu_T \left(S_{ij} - \frac{1}{3}\frac{\partial \tilde{u}_k}{\partial x_k}\delta_{ij} \right) - \frac{2}{3}\overline{\rho} k \delta_{ij} \tag{3.39}$$

where μ_T is the turbulent or eddy viscosity and S_{ij} is the Favre averaged strain rate expressed in terms of mean variables as,

$$S_{ij} = \frac{1}{2}\left[\left(\frac{\partial \tilde{u}_i}{\partial x_j}\right) + \left(\frac{\partial \tilde{u}_j}{\partial x_i}\right)\right] \tag{3.40}$$

The turbulent heat flux vector is modeled as,

$$q_{T_j} = \overline{\rho u_j'' h''} = -\frac{\mu_T}{Pr_T}\frac{\partial \tilde{h}}{\partial x_j} = -\frac{\mu_T C_p}{Pr_T}\frac{\partial \tilde{T}}{\partial x_j} = -\kappa_T \frac{\partial \tilde{T}}{\partial x_j} \tag{3.41}$$

Here the turbulent Prandtl number is defined as $Pr_T = (\mu_T C_p)/\kappa_T$, where μ_T is eddy viscosity and κ_T is turbulent conductivity, $Pr_T = 0.9$ is used in turbulent boundary layer flows and a value of 0.7 is used for free shear flows. The third and fourth terms in Eq. 3.30 RHS represent the work done due to viscous stresses and work done due to turbulent stresses. The fifth and sixth terms represent the turbulent transport of turbulent kinetic energy and viscous diffusion of turbulent kinetic energy and are modeled as,

$$-\overline{\rho u_i'' u_i'' u_j''} \quad = \quad \mu_T \frac{\partial k}{\partial x_j} \tag{3.42}$$

$$\frac{\partial}{\partial x_j}\overline{(t_{ij} u_i'')} \quad = \quad \mu \frac{\partial k}{\partial x_j} \tag{3.43}$$

The last term is due to compressible effects and is neglected.

In the above Eq. 3.39, 3.41, 3.42 and 3.43 it is needed to calculate μ_T and k

for which turbulence models are used, of which only zero, one and three equation model are discussed in coming sections.

3.5.2 Classification of Turbulence Models:

Turbulence models can be divided into two categories, based on the use of Boussinesq assumption. Models using the Boussinesq assumption will be referred to as *Category I*, or turbulent viscous models. These are also known as first-order models. Most models currently employed in engineering calculations are of this type. Experimental evidence indicates that the turbulent viscosity hypothesis, is a valid one, in many flow circumstances. There are exceptions, however, and there is no physical requirement that it hold for all cases. Models that affect closure to the Reynolds equations without this assumption will be referred to as *Category II* models and include those known as Reynolds stress or stress-equation models. The stress equation models are also referred to as second-order or second-moment closures. The other common classification of models is according to the number of supplementary partial differential equations that must be solved in order to supply the modeling Parameters. This number ranges from zero for the simplest algebraic models to 12 for the most complex of the Reynolds stress models (Donaldson and Rosenbaum, 1968). *Category III* models will be defined as those that are not based entirely on the Reynolds equations. Large-eddy simulations fall into this category since it is a filtered set of conservation equations that is solved instead of the Reynolds equations.

3.5.3 Algebraic or Zero- Equation Models

Algebraic turbulence models or zero-equation turbulence models are models that do not require the solution of any additional equations and are calculated directly from the flow variables. As a consequence, zero equation models may not be able to properly account for history effects on the turbulence, such as convection and diffusion of turbulent energy. These models are often too simple for use in general situations, but can be quite useful for simpler flow geometries or in start-up situations (e.g. the initial phases of a computation in which a more complicated model may have difficulties) one of the most successful of this type of model was suggested by Prandtl in the 1920s:

$$\mu_T = \rho l^2 \mid \frac{\partial u}{\partial y} \mid \tag{3.44}$$

where l, a "mixing length", can be thought of as a transverse distance over which particles maintain their original momentum, somewhat on the order of a mean free path for the collision or mixing of globules of fluid. The product $l \mid \frac{\partial u}{\partial y} \mid$ can be interpreted as the characteristic velocity of turbulence, ν_T. In Eq. (3.44), u is the component of velocity in the primary flow direction, and y is the coordinate transverse to the primary flow direction.

3.5.4 Boussinesq approximation

Turbulence modeling is the construction and use of a model to predict the effects of turbulence. Averaging is often used to simplify the solution of the governing equations of turbulence, but models are needed to represent scales of the flow that are not resolved.

A closure problem arises in the Reynolds-averaged Navier-Stokes (RANS) equation because of the non-linear term $\overline{v_i'v_j'}$ from the convective acceleration, known as the Reynolds stress,

$$R_{ij} = \overline{v_i'v_j'} \tag{3.45}$$

Closing the RANS equation requires modeling the Reynold's stress R_{ij}.

Boussinesq proposed relating the turbulence stresses to the mean flow to close the system of equations. Here the Boussinesq hypothesis is applied to model the Reynolds stress term. Note that a new proportionality constant $\nu_t > 0$, the turbulence eddy viscosity, has been introduced. Models of this type are known as eddy viscosity models or EVM's.

$$-\overline{v_i'v_j'} = \nu_t(\frac{\partial \overline{v_i}}{\partial x_j} + \frac{\partial \overline{v_j}}{\partial x_i}) - \frac{2}{3}(k + \nu_t(\frac{\partial \overline{v_k}}{\partial x_k}))\delta_{ij} \tag{3.46}$$

Which can be written in shorthand as

$$-\overline{v_i'v_j'} = 2\nu_t S_{ij} - \frac{2}{3}K\delta_{ij} \tag{3.47}$$

where S_{ij} is the mean rate of strain tensor. ν_t is the turbulence eddy viscosity. K is the turbulence kinetic energy and δ_{ij} is the Kronecker delta.

In this model, the additional turbulence stresses are given by augmenting the molecular viscosity with an eddy viscosity. This can be a simple constant eddy viscosity (which works well for some free shear flows such as axisymmetric jets, 2-D jets, and mixing layers).

3.5.5 One equation Spalart-Allmaras model

In one equation Spalart-Allmaras or SA Model [59] the eddy viscosity ν_T is related to the intermediate variable, $\tilde{\nu}$ by a damping function, f_{v1} as $\nu_T = \tilde{\nu} f_{v1}$, and the equation for $\tilde{\nu}$ is written as,

$$\frac{\partial \overline{\rho}\tilde{\nu}}{\partial t} + \frac{\partial \overline{\rho}\tilde{\nu}\tilde{u}_j}{\partial x_j} = c_{b1}\overline{\rho}\tilde{S}\tilde{\nu} - c_w f_w \overline{\rho}\left(\frac{\tilde{\nu}}{d}\right)^2 + \frac{1}{\sigma}\frac{\partial}{\partial x_k}\left[(\mu + \overline{\rho}\tilde{\nu})\frac{\partial \tilde{\nu}}{\partial x_k}\right] + \frac{c_{b2}\overline{\rho}}{\sigma}\frac{\partial \tilde{\nu}}{\partial x_k}\frac{\partial \tilde{\nu}}{\partial x_k} \tag{3.48}$$

In shorthand this is written as,

$$\frac{D\overline{\rho}\tilde{\nu}}{Dt} = \mathrm{Prod}(\tilde{\mathrm{S}}, \overline{\rho}\tilde{\nu}, \mathrm{d}) - \mathrm{Dest}(\overline{\rho}\tilde{\nu}, \mathrm{d}) + \frac{1}{\sigma}\left[\nabla.((\mu + \overline{\rho}\tilde{\nu})\nabla\tilde{\nu}) + \mathrm{c_{b2}}\overline{\rho}(\nabla\tilde{\nu})^2\right] \tag{3.49}$$

Here,

$$f_w = g\left[\frac{1 + c_{w3}^6}{g^6 + c_{w3}^6}\right], \quad f_{v1} = 1 - \left[\frac{\chi^3}{\chi^3 + c_{v1}^3}\right], \quad f_{v2} = 1 - \frac{\chi}{1 + \chi f_{v1}} \tag{3.50}$$

where,

$$\chi = \frac{\tilde{\nu}}{\nu}, \quad g = r + c_{w2}(r^6 - r), \quad r = \frac{\tilde{\nu}}{\tilde{S}\kappa^2 d^2}, \quad \tilde{S} = \bar{S} + \frac{\tilde{\nu}}{\kappa^2 d^2} f_{v2} \tag{3.51}$$

d is the normal distance from the wall and the vorticity magnitude is represented as $\bar{S} = \sqrt{2\Omega_{ij}\Omega_{ij}}$, in which the rotation tensor is given as $\Omega_{ij} = \frac{1}{2}\left[(\partial\tilde{u}_i/\partial x_j) - (\partial\tilde{u}_j/\partial x_i)\right]$ and the constants are given as $c_{b1} = 0.1355$, $c_{b2} = 0.622$, $c_{v1} = 7.1$, $\sigma = 2/3$, $\kappa = 0.41$, $c_{w1} = c_{b1}/\kappa^2 + (1 + c_{b2})/\sigma$, $c_{w2} = 0.3$, $c_{w3} = 2$.

The terms on the LHS of Eq. 3.48 represent the transport terms. The first and second terms on RHS of Eq. 3.48 represent the production and destruction of eddy viscosity. The last two terms on RHS represent the molecular and eddy diffusivity terms. The quantities embraced within them represents the major variables dependency of these source terms.

3.5.6 Boundary conditions for Spalart Allmaras model

The free stream and wall boundary conditions for various turbulence models are stated below with subscript ∞ and w representing the free stream and wall conditions.

$\tilde{v}_\infty = \frac{0.1\mu_\infty}{\bar{\rho}_\infty}$ and

$(v_{Tw}) = 0$

3.5.7 Transition k-kl-omega

The k-kl-omega model has three transport equation for laminar kinetic energy (k_L), turbulent kinetic energy (k_T) and inverse turbulent time scale (ω). It is a three equation eddy viscosity type [60].

$$\frac{D\rho k_L}{Dt} = \rho(P_{K_L} - R - R_{NAT} - D_L) + \frac{\partial}{\partial x_j}\left(\mu \frac{\partial k_L}{\partial x_j}\right) \tag{3.52}$$

$$\frac{D\rho k_T}{Dt} = \rho(P_{K_T} + R + R_{NAT} - \omega k_T - D_T) + \frac{\partial}{\partial x_j}\left[\left(\mu + \frac{\rho \alpha_T}{\alpha_k}\right)\frac{\partial k_T}{\partial x_j}\right] \tag{3.53}$$

$$\begin{aligned}\frac{D\rho\omega}{Dt} = \rho[C_{\omega 1}\frac{\omega}{k_T}Pk_T - \left(\frac{C_{\omega R}}{f_W} - 1\right)(R + R_{NAT}) - C_{\omega 2}\omega^2 \\ + C_{\omega 3} f_\omega \alpha_T f_\omega^2 \frac{\sqrt{k_T}}{d^3}] + \frac{\partial}{\partial x_j}\left[\left(\rho + \frac{\rho \alpha_T}{\alpha_k}\right)\frac{\partial \omega}{\partial x_j}\right]\end{aligned} \tag{3.54}$$

For Incompressible flow, the density term will be constant and the three equations will be given by Eq. 3.55 - Eq. 3.57. [61]

$$\frac{Dk_L}{Dt} = P_{K_L} - R - R_{NAT} - D_L + \frac{\partial}{\partial x_j}\left(\upsilon \frac{\partial k_L}{\partial x_j}\right) \tag{3.55}$$

$$\frac{Dk_T}{Dt} = P_{K_T} + R + R_{NAT} - \omega k_T - D_T + \frac{\partial}{\partial x_j}\left[\left(\upsilon + \frac{\alpha_T}{\alpha_k}\right)\frac{\partial k_T}{\partial x_j}\right] \tag{3.56}$$

$$\begin{aligned}\frac{D\omega}{Dt} = C_{\omega 1}\frac{\omega}{k_T}P_{k_T} - \left(\frac{C_{\omega R}}{f_W} - 1\right)(R + R_{NAT}) - C_{\omega 2}\omega^2 \\ + C_{\omega 3} f_\omega \alpha_T f_\omega^2 \frac{\sqrt{k_T}}{d^3} + \frac{\partial}{\partial x_j}\left[\left(\upsilon + \frac{\alpha_T}{\alpha_k}\right)\frac{\partial \omega}{\partial x_j}\right]\end{aligned} \tag{3.57}$$

Where,

P_{k_T} [Turbulent production term (due to turbulent fluctuation)] = $v_{T,s}S^2$,

$v_{T,s} = f_v f_{INT} C_\mu \sqrt{k}_{T,s} \lambda_{eff}$, $C_\mu = \frac{1}{A_0] + A_s(S/\omega)}$,$f_v = 1 - exp\left[-\frac{\sqrt{Re_T,s}}{A_v}\right]$,$f_{INT} = MIN\left[\frac{K_L}{C_{INT}k_{TOT}}, 1\right]$,$R_{eT,s} = \frac{f_W^2 K_T}{v\omega}$, $\lambda_{eff} = MIN(C_\lambda d, \lambda_T)$, $\lambda_T = \frac{\sqrt{k}}{\omega}$.

K_T, s [Small scale energy] = $f_{ss} f_W K_T$, $f_W = \frac{\sqrt{k}}{\omega}$, $f_{ss} = exp\left[-\left(\frac{c_{ss}v\Omega}{k}\right)^2\right]$

$k_{T,l}$ [Large Scale energy] =k_T - $K_{T,s}$

P_{k_L} [Laminar Kinetic energy term (due to turbulent fluctuation)] =$v_{T,s}S^2$

R [Effect(averaged) of streamwise fluctuations breaking down into turbulence during bypass transition] = $C_R \beta_{BP} k_L \omega / f_W$, $\beta_{BP} = 1 - exp\left[-\frac{\phi_{BP}}{A_{BP}}\right]$, $\phi_{BP} = MAX\left[\left(\frac{k_T}{v\Omega} - C_{BP,crit}\right), 0\right]$

R_{NAT} [Breaking down into turbulence due to instabilities] = $C_{R,NAT}\beta_{NAT}K_L\Omega$, $\beta_{NAT} = 1 - exp\left[-\frac{MAX(\phi_{NAT} - C_{NAT,crit}/f_{NAt,crit,0}))}{A_{NAT}}\right]$, $f_{NAT,crit} = 1 - exp\left[C_{NC}\frac{\sqrt{K_L}d}{v}]\right]$

The model is including the laminar and turbulent fluctuations on the energy equation and mean flow via. total thermal diffusivity and eddy viscosity equations

$$\overline{-u_i\theta} = \alpha_{theta,TOT}\frac{\partial\theta}{\partial x_i} \tag{3.58}$$

$$\overline{-u_iu_j} = v_{TOT}\left[\frac{\partial U_i}{\partial x_j} + \frac{\partial U_j}{\partial x_i}\right] - \frac{2}{3}k_{TOT}\delta_{ij} \tag{3.59}$$

3.5.8 Boundary conditions for Transition k-kl-omega model

The boundary conditions for the transition model are given below,

Table 3.1: Model Constants for Transition k-kl-omega [60]

$A_0 = 4.04$	$C_{INT} = 0.75$	$C_{\omega 1} = 0.44$
$A_S = 2.12$	$C_{TS,crit} = 1000$	$C_{\omega 2} = 0.92$
$A_V = 6.75$	$C_{RNAT} = 0.02$	$C_{\omega 3} = 0.3$
$A_{BP} = 0.6$	$C_{11} = 3.4 \times 10^{-6}$	$C_{\omega R} = 1.5$
$A_{NAT} = 200$	$C_{12} = 1.0 \times 10^{-10}$	$C_{\lambda} = 2.495$
$A_{TS} = 200$	$C_R = 0.12$	$C_{\mu,std} = 0.09$
$C_{BPcrit} = 1.2$	$C_{\alpha\theta} = 0.035$	$P_{r\theta} = 0.85$
$C_{NC} = 0.1$	$C_{SS} = 1.5$	$\sigma_k = 1$
$C_{NATcrit} = 1250$	$C_{\tau,1}$=4360	$\sigma_\omega = 1.17$

At solid boundaries,

$$k_T = k_L = 0$$

Normal gradient is zero, (η is wall normal coordinate direction)

$$\frac{\partial \omega}{\partial \eta} = 0$$

The turbulent Kinetic energy is related to the free stream turbulent intensity (Tu_∞) and free stream velocity U_∞ as,

$$Tu_\infty = \frac{\sqrt{\frac{2}{3} k_T}}{U_\infty}$$

3.6 Numerical method

The governing equations for any fluid flow can be expressed in the form of partial differential equations or integral equations. The exact analytical solutions of these equations are difficult to obtain for complex flows such as shock-wave turbulent boundary-layer interactions and high-speed cruise flow. As an engineering approach, these partial differential equations or integral equations are discretized to system of algebraic equations. Generally, Taylor series is used to approximate the partial differential equations to a system of algebraic linear equations. There are different discretization techniques like finite difference, finite element and finite volume. In this chapter, finite volume method approach is used. Reynolds-Averaged Navier-Stokes (RANS) equations [57] can be used for solving the high-speed supersonic or transonic flows. Basically, the terms in RANS equations can be viewed as three terms, the inviscid or convective terms, the viscous terms and the source terms.

The shock wave/turbulent boundary-layer interaction includes different high gradient regions such as separation bubble, shock waves, expansion waves, shear-layer and boundary-layer flow separation point and re-attachment point and, all of these physical features in the flow field has to be captured accurately using appropriate CFD methods. For the steady-state solution of the transonic and supersonic flows the hyperbolic and elliptic nature dominate the flow [62]. For supersonic steady flows, the convective terms dominate in the inviscid regions and the flow is hyperbolic in nature in space. For boundary-layer flows and separated flows the diffusive terms dominate. In a separation bubble, the flow is diffusive in nature hence the information can flow in all the directions and the flow posses elliptic nature in this confined region. The central difference scheme can be used to discretize the viscous terms.

Reynolds-averaged Navier-Stokes equations are used in either two-dimensional, three-dimensional or axisymmetric flow. The Spalart-Allmaras turbulence model was included in the simulation. The governing equations are discretized in a finite volume formulation where the inviscid fluxes are computed using Roe scheme. The turbulence model equations are fully coupled to the mean flow equations. In the following, finite volume formulation and Roe scheme are briefly discussed, for solving RANS equations using Spalart-Allmaras model for a perfect gas.

3.6.1 Generic form of governing equations

In this section, standard one-equation Spalart-Allmaras model [59] is used to calculate the eddy viscosity. In two-dimensional RANS equations are solved for one continuity, two momentum, one energy and one transport equation of viscosity equation along with turbulent closure equations. A total of six equations are solved simultaneously to obtain five conservative variables $\overline{\rho}, \overline{\rho}\tilde{u}, \overline{\rho}\tilde{v}, \overline{\rho}\tilde{E}$ and $\overline{\rho}\tilde{\nu}$. From these conservative variables, the six primitive mean flow quantities are derived as, $\tilde{u}$, and $\tilde{v}$, density $\overline{\rho}$, temperature $\tilde{T}$, and $\tilde{\nu}$. The mean pressure $\overline{p}$ is calculated from the perfect gas law. The two-dimensional system of RANS equations can be written by single equation in conservation form by,

$$\frac{\partial U}{\partial t} + \nabla.(\vec{F} + \vec{G}) = Q \tag{3.60}$$

Where U is the set of conservative vector variables, $\vec{F}$ is the flux vector in x-direction and $\vec{G}$ is the flux vector in the y-direction and Q is the source term. The total fluxes are written as inviscid part and viscous part. The subscripts I and V represent the inviscid and viscous terms. These equations are written in Cartesian form.

$$\frac{\partial U}{\partial t}+\frac{\partial F}{\partial x}+\frac{\partial G}{\partial y}=Q \tag{3.61}$$

$$F=F_I+F_V; \qquad G=G_I+G_V \tag{3.62}$$

$$U \quad = \quad \begin{bmatrix}\overline{\rho} & \overline{\rho}\tilde{u} & \overline{\rho}\tilde{v} & \overline{\rho}\tilde{E} & \overline{\rho}\tilde{\nu}\end{bmatrix}^T \tag{3.63}$$

$$F_I=\begin{bmatrix}\overline{\rho}\tilde{u}\\ \overline{\rho}\tilde{u}^2+\overline{p}+\frac{2}{3}\overline{\rho}k\\ \overline{\rho}\tilde{u}\tilde{v}\\ (\overline{\rho}\tilde{E}+\overline{p}+\frac{2}{3}\overline{\rho}k)\tilde{u}\\ \overline{\rho}\tilde{\nu}\tilde{u}\end{bmatrix}; \qquad G_I=\begin{bmatrix}\overline{\rho}\tilde{v}\\ \overline{\rho}\tilde{u}\tilde{v}\\ \overline{\rho}\tilde{v}^2+\overline{p}+\frac{2}{3}\overline{\rho}k\\ (\overline{\rho}\tilde{E}+\overline{p}+\frac{2}{3}\overline{\rho}k)\tilde{v}\\ \overline{\rho}\tilde{\nu}\tilde{v}\end{bmatrix} \tag{3.64}$$

$$F_V = \begin{bmatrix} 0 \\ \bar{t}_{xx} + \tau_{xx} \\ \bar{t}_{xy} + \tau_{xy} \\ (\bar{t}_{xx} + \tau_{xx})\tilde{u} + (\bar{t}_{xy} + \tau_{xy})\tilde{v} + (\kappa + \kappa_T)\frac{\partial \tilde{T}}{\partial x} + (\overline{\mu} + \sigma\mu_T)\frac{\partial k}{\partial x} \\ (\frac{1}{\sigma}\left[(\mu + \overline{\rho}\tilde{\nu})\right] + \frac{c_{b2}\overline{\rho}}{\sigma}\tilde{\nu})\frac{\partial \tilde{\nu}}{\partial x} \end{bmatrix} \quad (3.65)$$

$$G_V = \begin{bmatrix} 0 \\ \bar{t}_{xy} + \tau_{xy} \\ \bar{t}_{yy} + \tau_{yy} \\ (\bar{t}_{xy} + \tau_{xy})\tilde{u} + (\bar{t}_{yy} + \tau_{yy})\tilde{v} + (\kappa + \kappa_T)\frac{\partial \tilde{T}}{\partial y} + (\overline{\mu} + \sigma\mu_T)\frac{\partial k}{\partial y} \\ (\frac{1}{\sigma}\left[(\mu + \overline{\rho}\tilde{\nu})\right] + \frac{c_{b2}\overline{\rho}}{\sigma}\tilde{\nu})\frac{\partial \tilde{\nu}}{\partial y} \end{bmatrix} \quad (3.66)$$

$$Q = \begin{bmatrix} 0 & 0 & 0 & 0 & (\mathrm{Prod}(\tilde{\mathrm{S}}, \overline{\rho}\tilde{\nu}, \mathrm{d}) - \mathrm{Dest}(\overline{\rho}\tilde{\nu}, \mathrm{d}) \end{bmatrix}^T \quad (3.67)$$

3.6.2 Finite volume method

The governing equations of fluid dynamics can be expressed in differential form. A numerical scheme is applied to these equations to divide the domain into grid points and finite difference equations are solved. An alternate approach is to solve the integral form. In this approach, the physical domain is divided into small areas. 2-D case is shown in Fig. 3.3 (reproduced from [63]) . Dependent variables are evaluated either at the centers of the volume or at the corners of the volumes.

In finite volume method, the physical domain is subdivided to small volumes(useful when the domain is highly irregular and complicated). No coordinate transformation is required. Mass, momentum and energy are automatically conserved, since the integral form of the equations is solved. Another advantage of the finite volume method is that it is easily formulated to allow for unstructured meshes.

In order to explain finite volume method, consider a 2-D model equation

$$\frac{\partial U}{\partial t}+\frac{\partial F}{\partial x}+\frac{\partial G}{\partial y}=0 \tag{3.68}$$

Integrating over finite volume abcd (unit depth) gives

$$\int\int\int_{abcd}(\frac{\partial U}{\partial t}+\frac{\partial F}{\partial x}+\frac{\partial G}{\partial y})\mathrm{d}\,\upsilon=0 \tag{3.69}$$

Where $\mathrm{d}\,\upsilon=\mathrm{d}\,x\times\mathrm{d}\,y\times(1)$ Applying Greens theorem gives,

$$\frac{\partial}{\partial t}\int\int\int_{abcd}U(1)\,\mathrm{d}\,x\,\mathrm{y}+\oint\oint H.n\,\mathrm{d}\,S=0 \tag{3.70}$$

Where n is unit vector normal surface S of the control volume. H can be expressed as $H=Ei+Ej$ for a 2-D geometry

$$H.n\,\mathrm{d}\,S=(E\,\mathrm{d}\,y-F\,\mathrm{d}\,x)(1) \tag{3.71}$$

The solution can be solved to

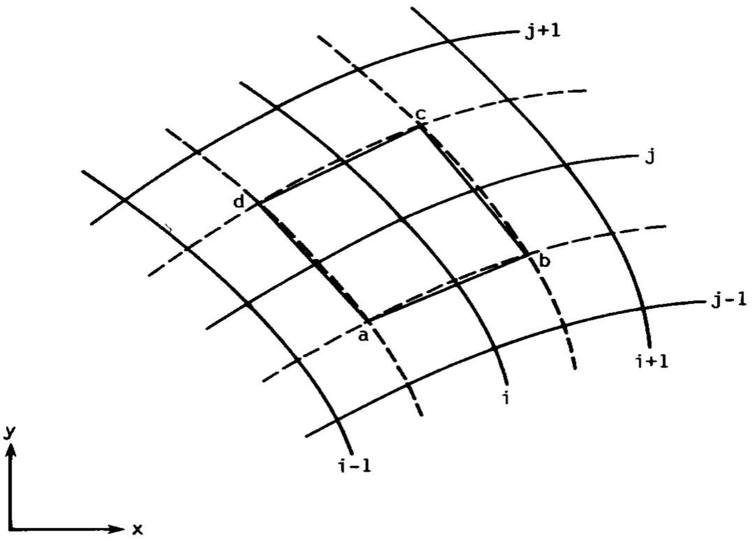

Figure 3.3: Two-Dimensional Finite Volume [63]

$$\frac{\partial}{\partial t}\int\int_{abcd} U(1)\,\mathrm{d}\,x\,\mathrm{y} + \oint_{abcd}(E\,\mathrm{d}\,y - F\,\mathrm{d}\,x) = 0 \tag{3.72}$$

This can be approximated to

$$\begin{aligned}\frac{(U_{i,j}^{n+1} - U_{i,j}^{n})}{t}S_{abcd} &+ (E_{i,j-1/2}\triangle y_{ab} + E_{i-1/2,j}\triangle y_{bc} + E_{i,j+1/2}\triangle y_{cd} + E_{i+1/2,j}\triangle y_{da}) \\ &-(F_{i,j-1/2}\triangle x_{ab} + F_{i-1/2,j}\triangle x_{bc} + F_{i,j+1/2}\triangle x_{cd} + F_{i+1/2,j}\triangle x_{da}) = 0\end{aligned} \tag{3.73}$$

Where S is the surface area of the quadrilateral, U in the average value in the quadrilateral. This method is called the cell-centered finite volume method. The dependent variables can also be evaluated at the vertices of the cell, this is known as nodal point finite volume scheme.

The Eq. 3.60 is integrated over the control surface area (CS) of control volume

(CV) in figure 3.4

$$\frac{\partial}{\partial t}\iiint\limits_{CV} U dV + \iint\limits_{CS}\Big[(\vec{F_I}+\vec{G_I})+(\vec{F_V}+\vec{G_V})\Big].(\hat{j}ndS) = \iiint\limits_{CV} Q dV \tag{3.74}$$

$$\frac{\partial U}{\partial t} = -\frac{1}{V_{i,j}}\Big[\vec{F}_{i+1/2,j}.\vec{S}_{i+1/2,j}+\vec{F}_{i-1/2,j}.\vec{S}_{i-1/2,j}+\vec{G}_{i,j+1/2}.\vec{S}_{i,j+1/2}+\vec{G}_{i,j-1/2}.\vec{S}_{i,j-1/2}\Big]+Q \tag{3.75}$$

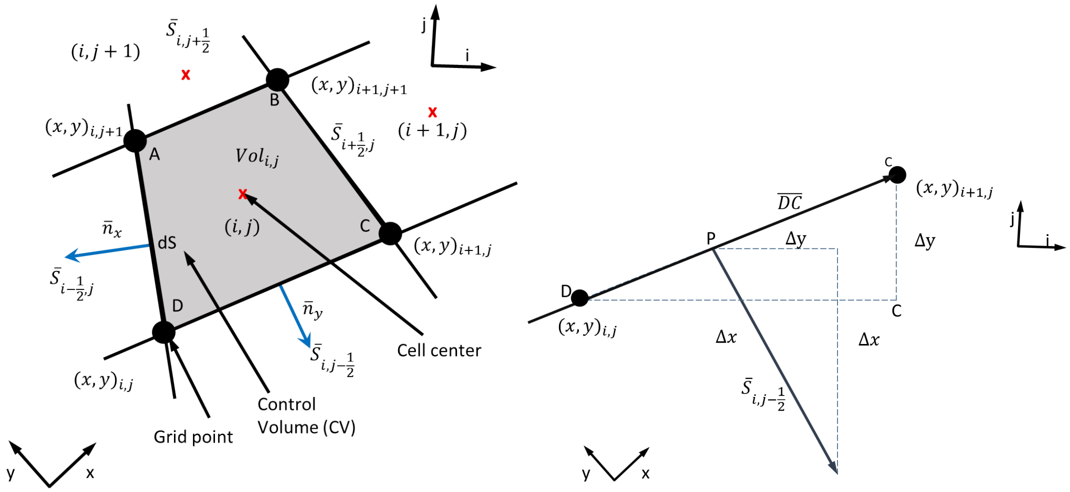

(a) (b)

Figure 3.4: (a) Two-dimensional control volume used in finite volume formulation, where the grid points are represented by solid circles with small indices of i and j and cell centers are shown by crosses represented by caps indices of I and J. (b) Calculation of normal surface vector $S_{i,j+1/2}$ [64]

$$\begin{aligned}\vec{S}_{i+1/2,j} &= +(y_{i+1,j+1}-y_{i+1,j})\hat{i}-(x_{i+1,j+1}-x_{i+1,j})\hat{j}\\ \vec{S}_{i-1/2,j} &= -(y_{i,j+1}-y_{i,j})\hat{i}+(x_{i,j+1}-x_{i,j})\hat{j}\end{aligned} \tag{3.76}$$

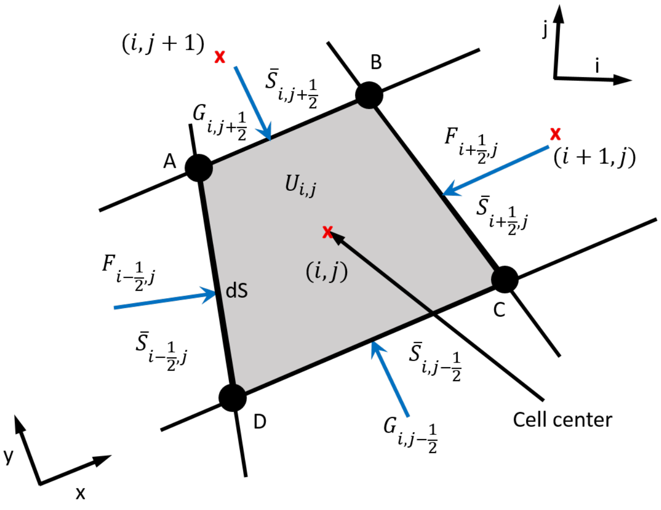

Figure 3.5: The conservative variable $U_{I,J}$ at cell center calculated from the fluxes F and G passing through the cell boundaries in the x- and y-directions.[64]

$$\begin{aligned} V_{i,j} = [&|(x_{i,j} - x_{i+1,j})y_{i+1,j+1} + (x_{i+1,j} - x_{i+1,j+1})y_{i,j} + (x_{i+1,j} - x_{i,j})y_{i+1,j}| \\ &+|(x_{i,j} - x_{i+1,j+1})y_{i,j+1} + (x_{i+1,j+1} - x_{i,j+1})y_{i,j} + (x_{i,j+1} - x_{i,j})y_{i+1,j+1}|] \end{aligned} \tag{3.77}$$

$\hat{n}$ is the unit normal vector to surface area dS as shown in Fig. 3.4 (reproduced from Amjad [64]) . Here $\vec{S}_{i+1/2,j}$ and $S_{i-1/2,j}$ are the surface area vectors and,$\hat{i}$ and $\hat{j}$ are unit vectors in i and j direction. x and y are the coordinates of the grid points and $V_{i,j}$ is the control volume. The evaluation of $S_{i-1/2,j}$ is shown in Fig. 3.4. The vector $\vec{DC} = \Delta x\hat{i} + \Delta y\hat{j}$. where $\Delta x = x_{i+1,j} - x_{i,j}$ and $\Delta y = y_{i+1,j} - y_{i,j}$. Hence the normal vector is calculated as $\vec{S}_{i,j-1/2} = \Delta y\hat{i} - \Delta x\hat{j}$. Similarly $\vec{S}_{i,j+1/2}$ is evaluated. The control volume in Fig. 3.5 is calculated as summation of area of triangles ABD and BCD.

There are several methods for evaluation of fluxes using finite volume method. In the below section, a brief formulation of Roe flux-difference splitting scheme is discussed.

3.6.3 Flux-difference splitting scheme

The main challenge in constructing methods for solving the Euler equations is to find ways of estimating the flux terms at the control volume faces. The flux quantities at the cell interface using flux-difference splitting have been interpreted as being caused by a series of waves. The wave interpretation is derived from the characteristic field of the Euler equations. The problem of computing the cell-face fluxes for a control volume is viewed as a series of l-D Riemann problems along the direction normal to the control volume faces. One way of determining these fluxes is to solve the Riemann problem using Godunov's method. Of course, the solution in the present case would be a generalized problem with arbitrary initial states. Because some of the details of the exact solution, obtained at a considerable cost, are lost in the cell-averaged representation of the data, the solution of the full Riemann problem is usually replaced by methods referred to as approximate Riemann solvers. The Roe method (Roe, 1980) and the Osher scheme (Osher, 1984) are the most well-known of these schemes. Owing to its simplicity, the Roe scheme and its many variations have evolved as the method of choice among flux-difference splitting schemes. In the next section, Roe's scheme will be discussed as applied to the Euler equations. This technique is another way of calculating the flux values at the control volume boundaries in the finite-volume approach.

3.6.4 Roe scheme

In view of the fact that the Riemann problem requires a solution of a non-linear system, a significant gain in efficiency can be realized if a solution to a linear problem approximating the original Riemann problem can be obtained. This is the basis for Roe's scheme. Consider the original Riemann problem in the form

$$\frac{\partial U}{\partial t} + \frac{\partial E}{\partial x} = 0 \tag{3.78}$$

$$U\{x, 0\} = \begin{cases} U_L & x < 0 \\ U_R & x > 0 \end{cases}$$

Roe's linear approximation to the Riemann problem is written

$$\frac{\partial U}{\partial t} + [\hat{A}]\frac{\partial U}{\partial x} = 0 \tag{3.79}$$

where the initial conditions are the same as those in the nonlinear problem and$[\hat{A}]$ is Roe's averaged matrix and is assumed to be a constant in this formulation. Recall that the original Jacobian was defined by

$$[\hat{A}] = \frac{\partial E}{\partial x} \tag{3.80}$$

The Jacobian matrix is replaced by $[\hat{A}]$ in this system. The components of the $[\hat{A}]$ matrix are evaluated using averaged values of U at the interface separating the two states. This is indicated by writing

$$[\hat{A}] = [\hat{A}(U_L, U_R)] \tag{3.81}$$

The Roe-averaged matrix $[\hat{A}]$ is chosen to satisfy certain conditions so that a solution of the linear problem becomes an approximate solution of the nonlinear Riemann problem. These conditions include the following.

1. A linear mapping relates the vector space U to the vector space E.
2. As U, approaches U_R, i.e., as an undisturbed state is reached,

   $$[\hat{A}(U_L, U_R)] \Longrightarrow [\hat{A}]$$

   when

   $$U_L \to U_R \to U$$

   where $[A]$ is the Jacobian of the original system.
3. For any two values U_L, U_R, the jump condition across the interface must be correct, i.e.,

   $E_R - E_L = [\hat{A}](U_L, U_R)$
4. The eigenvalues of $[\hat{A}]$ are real and linearly independent.

Consider the system of equations given by Eq. 3.79. This is a hyperbolic system that may be diagonalized by writing the constant matrix [A] as

$$[\hat{A}] = [\hat{T}][\hat{\wedge}][\hat{T}]^{-1} \tag{3.82}$$

The original equations can then be cast in the form

$$\frac{\partial U}{\partial t} + [\hat{T}][\hat{\wedge}][\hat{T}]^{-1}\frac{\partial U}{\partial x} = 0 \tag{3.83}$$

Pre-multiplying by $[\hat{T}]^{-1}$ and defining the vector W as

$$W = [\hat{T}]^{-1}U \tag{3.84}$$

leads to the linear problem

$$\frac{\partial W}{\partial t} + [\hat{\wedge}]\frac{\partial W}{\partial x} = 0 \tag{3.85}$$

where the matrix of eigenvalues $[\hat{\wedge}]$ is a diagonal matrix. This produces an uncoupled hyperbolic system. The numerical method may be applied to each of the uncoupled equations of this system, and the result transformed back to the original variables. For a single linear equation, the value of W is constant along the characteristic defined by $dx/dt = \lambda_k$. As each of the waves associated with the eigenvalues of the system is crossed, the values of the dependent variables experience a jump. Consequently, the values of W_k are constant between each pair of waves in the domain. Mathematically, this can be stated as

$$W_k = const$$

when

$$\lambda_{k-1} \leq \frac{x}{t} \leq \lambda_k \tag{3.86}$$

Consequently, the value of W at any point may be written

$$W_k = W_1 + \sum_{j=2}^{k} (W_j - W_{j-1}) \tag{3.87}$$

Again, since $[\hat{A}]$ is a constant matrix,

$$U_k = U_1 + \sum_{j=2}^{k} (U_j - U_{j-1}) \tag{3.88}$$

and the final result is that the flux changes may be written

$$E_k = E_1 + \sum_{j=2}^{k} \delta E_j \tag{3.89}$$

where the flux increments are associated with the crossing of each wave in the system. If the entire wave system is traversed and the left and right states are identified with appropriate subscripts, then

$$E_R = E_L + [\hat{A}](U_L, U_R) \tag{3.90}$$

As shown in the previous section, the $[\hat{A}]$ matrix may be split, corresponding to changes that occur across negative and positive waves. Consequently, splitting the calculation of the fluxes into contributions across negative and positive waves to determine appropriate formulas for the cell-face fluxes in the linear Riemann problem. Referring to Fig. 3.6 (reproduced from Pletcher et.al [63]) one notes that the interface flux can be computed by starting at either the left or the right state.

Starting at the left state, one can write

$$\begin{aligned} \tilde{E}_{i+\frac{1}{2}} &= E_L + [\hat{A}^-](U_L, U_R) \\ E_R &= \tilde{E}_{i-\frac{1}{2}} + [\hat{A}^-](U_L, U_R) \end{aligned} \tag{3.91}$$

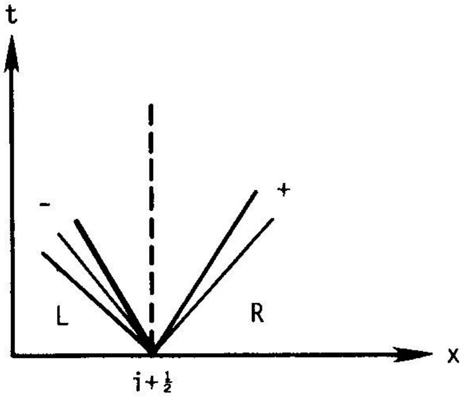

Figure 3.6: Decomposed flux for the linear Riemann problem [63]

A symmetric result is used in applications of computational fluid dynamics, and this may be obtained by averaging the cell-face flux formulas to obtain the following appropriate expression:

$$\tilde{E}_{i+\frac{1}{2}} + \frac{1}{2}\{(E_L + E_R) - [|\hat{A}|](U_L, U_R)\} \tag{3.92}$$

In this equation, $[\hat{A}] = [\hat{T}][\wedge][\hat{T}]^{-1}$ is the diagonal matrix whose entries are the absolute values of the eigenvalues. The numerical flux expression incorporates upwind influence through the addition of contributions across positive and negative waves. Condition 3 and the subsequent expressions for the interface flux given by Eq. 3.91 show that the change across any wave depends upon the change in state variables across all waves. This point can be noted by recalling that a diagonalization of the system leads to uncoupled equations providing the changes across each wave in a modified set of variables derived by multiplication by $[\hat{T}]^{-1}$. When the flux values are recovered by multiplying by $[\hat{T}]$, the change in flux across each wave is seen to depend upon the change in U across the entire system of waves. The Roe-averaged matrix may be constructed by noting that U and E are quadratic functions of the variable z, defined as

$$z = \sqrt{\rho} \begin{bmatrix} 1 \\ u \\ H \end{bmatrix} \tag{3.93}$$

The conservative variables may be written in terms of the z variable as

$$U = \begin{bmatrix} z_1^2 \\ z_1 z_2 \\ \frac{z_1 z_2}{\gamma} + \frac{1}{2}\frac{\gamma-1}{\gamma} z_2^2 \end{bmatrix} \tag{3.94}$$

where the vector of conservative variables U is defined for the 1-D case where u = w = 0. The flux term may also be written as

$$E = \begin{bmatrix} z_1 z_2 \\ \frac{\gamma-1}{\gamma} z_1 z_3 + \frac{1}{2}\frac{\gamma-1}{\gamma} z_2^2 \\ z_1 z_3 \end{bmatrix} \tag{3.95}$$

Arithmetic average of any quantity is defined with an overbar symbol in the following manner

$$\overline{x}_{i+1/2} = \frac{1}{2}(x_i + x_{i+1}) \tag{3.96}$$

and note the exact expansion formula:

$$\Delta(xy)_{i+1/2} = \overline{x}_{i+1/2}\Delta y_{i+1/2} + \overline{y}_{i+1/2}\Delta x_{i+1/2} \tag{3.97}$$

Applying this expansion formula results in conservative variable and flux formulas of the form

$$U_{i+1} - U_i = [B](z_{i+1} - z_1) \tag{3.98}$$

and

$$E_{i+1} - E_i = [C](z_{i+1} - z_1) \tag{3.99}$$

where

$$[B] \;=\; \begin{bmatrix} 2\overline{z}_1 & 0 & 0 \\ \overline{z}_2 & \overline{z}_1 & 0 \\ \frac{\overline{z}_3}{\gamma} & \frac{\gamma-1}{\gamma}\overline{z}_2 & \frac{\overline{z}_1}{\gamma} \end{bmatrix} \tag{3.100}$$

and

$$[C] \;=\; \begin{bmatrix} \overline{z}_2 & \overline{z}_1 & 0 \\ \frac{\gamma-1}{\gamma}\overline{z}_3 & \frac{\gamma+1}{\gamma}\overline{z}_2 & \frac{\gamma-1}{\gamma}\overline{z}_1 \\ 0 & \overline{z}_3 & \overline{z}_2 \end{bmatrix} \tag{3.101}$$

with the result that

$$E_{i+1} - E_i = [C][B]^{-1}(U_{i+1} - U_1) \tag{3.102}$$

The matrix $[C][B]^{-1}$ is identical to the Jacobian matrix [A] if the original variables are replaced by an average weighted by the square root of the density. If

$$R_{i+1/2} = \sqrt{\frac{\rho_{i+1}}{\rho}} \tag{3.103}$$

then

$$\hat{\rho}_{i+1/2} = R_{i+1/2}\rho_i \tag{3.104}$$

$$\hat{u}_{i+1/2} = \frac{R_{i+1/2}u_{i+1} + u_i}{1 + R_{i+1/2}} \tag{3.105}$$

$$\hat{H}_{i+1/2} = \frac{R_{i+1/2}H_{i+1} + H_i}{1 + R_{i+1/2}} \tag{3.106}$$

where the quantity $\hat{H}$ is the averaged total enthalpy and H is defined by

$$H = \frac{E_t + p}{\rho} \tag{3.107}$$

The development of the averaged matrix has used the so-called parameter vector approach. This Roe-averaged state may be directly obtained by solving Eq. 3.91 for the state variables. This follows because the correct averaged matrix is the only one that will provide the correct relationship satisfying these equations. The numerical flux for the first-order Roe scheme is then written in the form

$$\tilde{E}_{i+1/2} = \frac{1}{2}\left\{E_i + E_{i+1} - [\hat{T}_{i+1/2}][|\hat{\Lambda}_{i+1/2}|][\hat{T}_{i+1/2}]^{-1}(U_{i+1/2} - U_i)\right\} \tag{3.108}$$

This may be used to calculate the first-order solution using the standard explicit or implicit techniques for advancing the solution in time. In this formula, the problem of expansion shocks must be considered. By way of review, recall that the formulation of the Roe scheme admits an expansion shock as a perfectly appropriate solution of the approximate problem. As a consequence, stationary expansion shocks are not dissipated by this method. An appropriate entropy fix, but one that does not distinguish between shocks and expansions, is easily implemented by replacing the components of $[|\hat{\Lambda}|]$ by $\beta(\hat{\lambda}^{l}_{i+1/2})$, where

$$[|\hat{\Lambda}_{i+1/2}|] = \begin{bmatrix} |\hat{\lambda}^{1}_{i+1/2}| & 0 & 0 \\ 0 & |\hat{\lambda}^{2}_{i+1/2}| & 0 \\ 0 & 0 & |\hat{\lambda}^{3}_{i+1/2}| \end{bmatrix} \tag{3.109}$$

and

$$\beta(\hat{\lambda}) = \begin{cases} |\hat{\lambda}| & |\hat{\lambda}| \geq \epsilon \\ \frac{(\hat{\lambda}^2+\epsilon^2)}{2\epsilon} & |\hat{\lambda}| < \epsilon \end{cases}$$

In this set of expressions, the Roe average is implied by the circumflex symbol with subscript $i + \frac{1}{2}$.

3.7 Theoretical Lift Increment

Research methodology presented in the previous section forms the basis for finding computed lift coefficient. This section deals with the theoretical formulation that will enable us to compare theoretical and computed lift increments.

Vortex flow is the one where streamlines are all concentric about a given point and strength of which is given by circulation (Γ). If this point vortex is extended along a straight line such that the line passes through the center then such line is called straight vortex filament,the flow induced by the filament in a plane perpendicular to the filament itself have the strength of the point vortex i.e. Γ. An infinite number of vortex filament when placed side by side forms a vortex sheet, the circulation around this sheet is given by $\Gamma = \int_a^b \gamma(s)$ ds, where "s" is the distance measured along the sheet in the edge view and edge view of sheet starts from “a” and ends at “b”. Ludwig Prandtl in 1912-1932 proposed a theory in which he suggested replacing the surface of the airfoil with a thin vortex sheet such that the surface of the airfoil is now a streamline and in turn circulation is found around it, which gives us the lift around it by, Kutta-joukowski theorem, $L' = \rho_\infty\ V_\infty \Gamma$. Thin airfoil theory was proposed by a friend of Prandtl and a great American-German mathematician Max Munk [65], which is supported and polished by British aerodynamicist Hermann Glauert and others. This theory proposes that for airfoil which are very thin the vortex sheet can be placed on the camber line and then chord line such that camber line becomes streamline and vortex sheet is placed on the camber line. $\gamma(s)$ is found such that camber line is streamline and Kutta-condition, γ(T.E)=0 on the chord line. The fundamental equation of thin airfoil theory is given by the equation,

$$\frac{1}{2\pi}\int_0^c \frac{\gamma(\xi)d\xi}{x-\xi} = V_\infty\left(\alpha - \frac{dz}{dx}\right) \tag{3.110}$$

where,

dz/dx = Slope of camber line at a point x (airfoil is in ZX plane),

x=Position where velocity component normal to chord line induced by vortex sheet is found,

V_∞ = Free Stream Velocity,

α = Angle of Attack (AoA),

$\gamma(\xi)d\xi$= strength of the vortex sheet of elemental length $d\xi$ at a distance ξ

from the leading edge.

From the Eq.3.110 we obtain the theoretical lift coefficient and hence slope of lift curve for a thin airfoil with the inviscid and incompressible flow.

$$C_{l\alpha} = 2\pi \tag{3.111}$$

with the correction for compressible flow, the above equation is given by,

$$C_{l\alpha} = \frac{2\pi}{\sqrt{1-(M_\infty)^2}} = \frac{2\pi}{\sqrt{1-(0.7)^2}} = 8.798\, radians \tag{3.112}$$

Kaul et.al [4] deduced the equations for calculating the theoretical increment of the lift due to the VCCTEF flap segment using potential flow theory given in John D. Anderson[66]. In order to find the incremental lift coefficient which is given by,

$$\Delta C_l = C_{l\alpha}\Delta\alpha = C_{l\alpha}\sum_{i=1}^{n}\frac{\partial\alpha}{\partial\delta_i}\delta_i \tag{3.113}$$

Where, $C_{l\alpha}$ is slope of the lift curve and $\frac{\partial\alpha}{\partial\delta_i}$ is control derivative of each camber segment of absolute deflection δ_i(deflection of i_th flap segment from the horizontal line). This control derivative is given by,

$$\frac{\partial\alpha}{\partial\delta_i} = \left.\frac{cos^{-1}(-c^*) - \sqrt{1-c^{*2}}}{\pi}\right|_{c_i^*}^{c_{i+1}^*}$$

$$= \left[\frac{cos^{-1}(-c_{i+1}^*) - \sqrt{1-c_{i+1}^{*2}}}{\pi}\right] - \left[\frac{cos^{-1}(-c_i^*) - \sqrt{1-c_i^{*2}}}{\pi}\right] \tag{3.114}$$

c_i^* = 1 - 2 $\frac{x_i}{c}$, in which x_i is the hinge position of the i_th flap segment and c is the total chord.

The position of the hinge point of the i_th segment of flap is measured from trailing edge and is given by the equation,

$$x_i = (n + 1 - i) \times cf \tag{3.115}$$

where,

n= number of flap segments,

x_i = position of the i th flap from the trailing edge,

cf = length of the flap chord segment, which is, flap chord(total)/n.

The position of the first hinge flap is x_1=n×cf, since i=1, and the position of the last hinge of the flap is cf and the position of T.E is 0.

Let us consider that we are having 3 segment flap (n=3) namely, VCCTEF 123. The total flap chord length is 30 % of chord(c). Length of each flap segment is cf=0.1c. The hinge point of each flap segment is given in Fig.3.7, which shows flap hinge position from the trailing edge measured normal to the hinge axis.The first flap is at a distance of total flap chord length. While taking absolute deflection one must be careful regarding its measurement, it is measured with respect to horizontal line as shown in the Fig.3.7.

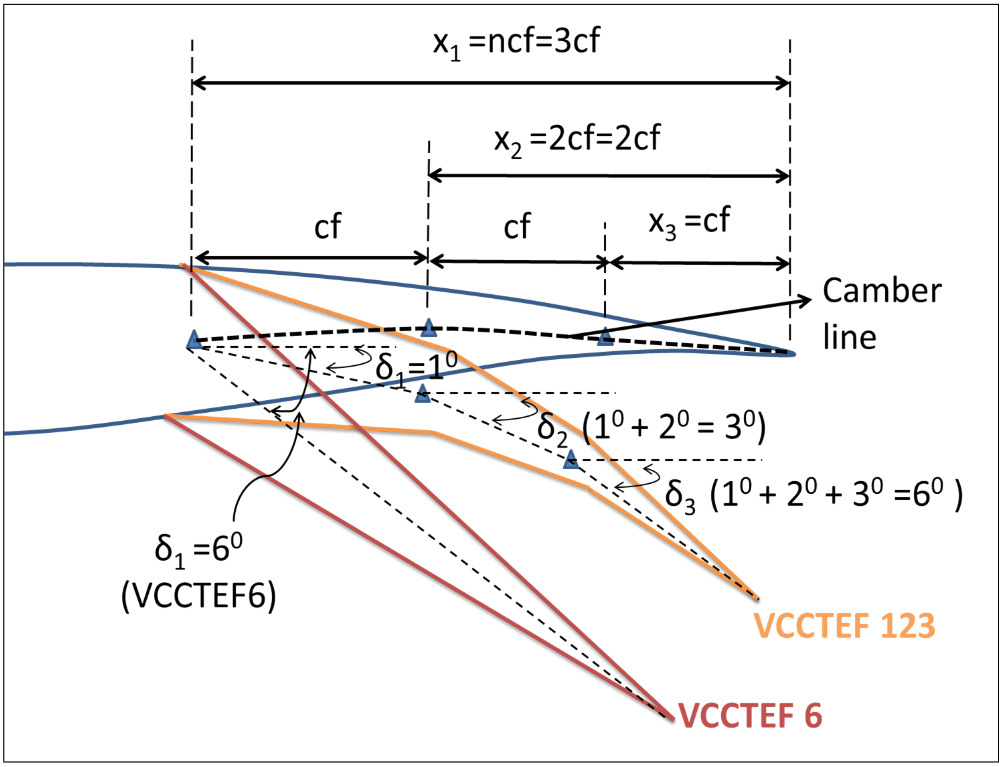

Figure 3.7: Flap hinge position & absolute deflection of camber segment (Not to be Scaled)

3.8 Conclusion

Navier-Stokes equations are the governing equations in computational fluid dynamics. The averaged equations, known as Reynolds-Averaged Navier - Stokes (RANS) equations has an advantage over Direct Numerical Simulation (DNS) in terms of grid size requirement. But the averaging concept, which is supposed to be a boon, turns in to a bane by giving rise to Reynolds stress term which doesn't allow the system to close, thus giving rise to closure problem. Turbulence modeling solves the closure problem by suitable approximations. Once the number of equations is equal to number of unknowns, a set of Partial Differential Equations (PDE) is obtained. Analytical solution of PDE is difficult, so they are converted into a set of the algebraic equation which can be discretized numerically using finite volume method. In the finite volume method flux difference splitting (Roe Scheme) scheme can be used to estimate flux terms at the face of the control volume. RANS equations have the capability of solving the high-speed flows. In the end, a theoretical formulation is obtained to compare computed and theoretical lift increments.

CHAPTER 4

GRID GENERATION & SIMULATION METHODOLOGY

4.1 Grid Generation guidelines

Grid generation is an important part of computational fluid dynamics. The entire region of study is divided into a small sets of control volumes. The grid quality plays an important role in getting the solution, which is more consistent when the grid is well constructed. However, computational time also plays an important role in getting the solution. Ones prime objective must be to get better result in less computational time. To reduce the mesh size one must create a fine grid only around the place where the flow matters the most. When dealing with the flows around airfoil the most important region is closest to the wall/airfoil. The wake region is an important decider for drag, so mesh must be finer in this region as well. The near wall mesh guidelines will be dealt in 4.2.

4.2 Considerations for Near Wall Mesh

Near the wall,the mesh must be fine enough to capture the flow properly.The question which arises is the acceptable distance between the wall and the near wall cell centroid. This distance is decided by the law of wall which was proposed by Theodore von Karman (1930) [67]. In the field of fluid dynamics, this law states that the average velocity at a given point say A, is directly proportional to the log of the distance between point A and wall or fluid region boundary. The log-law, which is abided by fully developed flows and equilibrium boundary layers, provides an extreme limit on the acceptable value of y (the distance between the wall and near-wall cell centroid).

The velocity profile as estimated by the log law in the log layer

$$u^+ = \frac{1}{\kappa}\ln(y^+) + B \tag{4.1}$$

Where, u^+ (Dimensionless velocity) = $\frac{u}{u_\tau}$; u_τ (frictional vel.)=$\sqrt{\frac{\tau_w}{\rho}}$; τ_w : wall shear stress; ρ: fluid density,κ (Von Karman's const.) $\approx$ 0.41, B(Const.) $\approx$ 5.1

y^+ (Dimensionless distance) = =$\frac{y\,u_\tau}{\nu}$

where, y is the distance from the wall and u is the velocity parallel to the wall, which is a function of y i.e. u=u(y).

Close to the wall in the viscous sublayer $u^{+} = y^{+}$

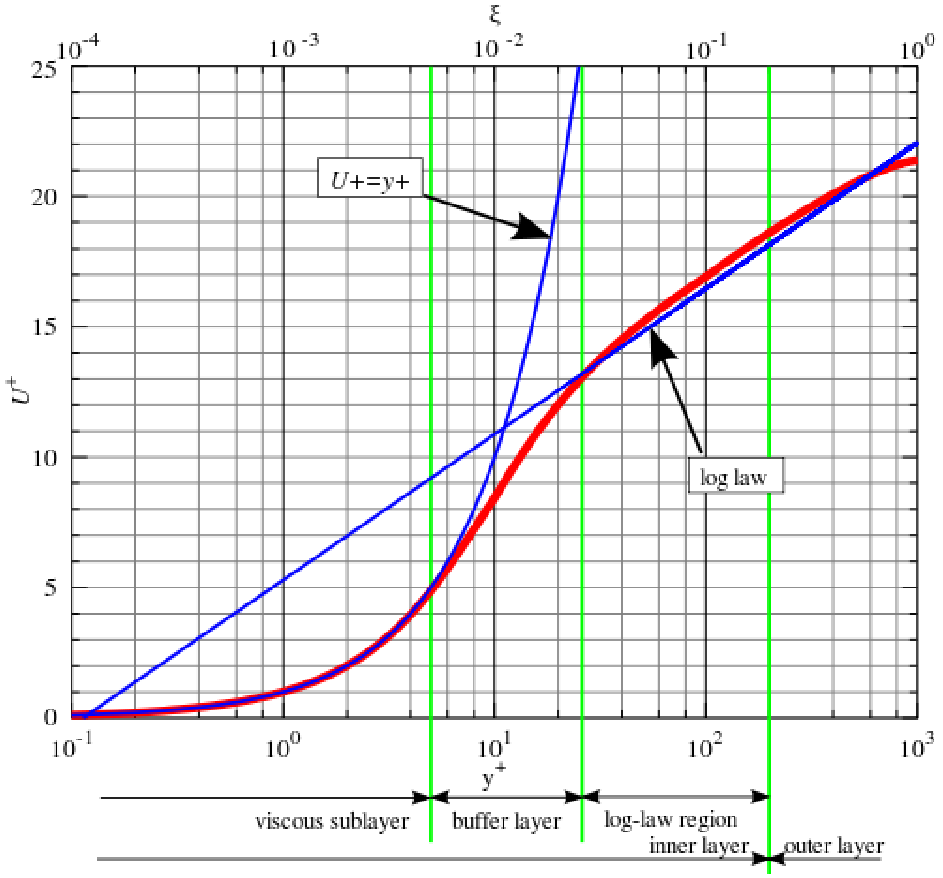

Figure 4.1: Log Law (Variation of u^{+} with y^{+})

There are some estimations of u^{+} below the regions of applicability of log law, where viscous sublayer and buffer layer u^{+} are present.[68]

In the Viscous sublayer,

For, $y^{+} < 5$

$u^{+} = y^{+}$

We can extend the approximation beyond 5 wall units but the error at $y^{+} = 12$ is around 25%.

In the buffer layer,

For, $5 < y^+ < 30$

$u^+ \neq y^+$

$u^+ \neq \frac{1}{\kappa} \ln y^+ + B$

Cell's centroid adjacent to the walls should be set inside the log-law layer $30 < y^+ < 300$ for the non-equilibrium or standard wall functions. A y^+ value near the lower limit ($y^+ \approx 30$) is suitable. Though wall function can be used for $y+ < 11.2$ [69] one should abstain from using it because of the less accuracy of the wall function. Also, lower Reynolds-number effects can not be accounted by the turbulence models. A rule to keep in mind while setting near wall distance of the mesh is to make it either too coarse such that y+ is above the upper limit of 30 or fine enough to have y+ below a limit of 5.The upper limit of the log layer depends on Reynolds number and pressure gradients. It increases as the Reynold's number increases and the higher values of y^+ are not desirable because wake component becomes considerably large above log layer.Hence, it is important to have few mesh cells in the boundary layer.

4.2.1 Spalart-Allmaras (SA) Model

SA model is best suited for the meshes that properly resolve the viscosity-effected region. In its complete implementation it is to be used when the meshes made can properly resolve the viscosity-affected region. This make this model, a low-Reynolds-number model.This model can attenuate the turbulent viscosity in a viscous sub-layer.

The implemented boundary conditions for the SA model make this model capable of working with coarser meshes, that are suitable for the wall function approach. If one is using a coarse mesh, then the steps/guidelines described in section 4.2 has to be followed.

In summary, to achieve the better results with the SA model, one must use a mesh with $y^+ \geq 30$ or a fine near-wall mesh $y_\rho^+ = 1$ for the first near-wall cell center.

4.2.2 Transition Model (Transition k-kl-omega)

For a better transition prediction, an appropriate mesh refinement and specification of the inlet turbulence levels is critical .A low Reynold's number mesh having a sufficient stream-wise resolution can accurately resolve the transition region. Additional mesh considerations are to be taken while using the transition model. Solution by transition model is largely affected by the good prediction of transition location which is in turn is affected by the estimation of decay of turbulence from inlet to leading edge of the device.

4.3 Validation Cases

This section gives the detail of various experimental data used for the validation of Spalart-Allmaras (SA) and Transition k-kl-omega models.

4.3.1 Validation of SA model

For the validation of fully turbulent results, NACA 0012 airfoil experimental results are chosen. NACA 0012 airfoil experimental values at Reynold‘s number 3 million and 6 million are given by Abbott and Von Doenhoff (untripped data) [70], Ladson (tripped data) [71] and Gregory and O’Reilly (tripped data) [72]. Clearly, there is a variation in the results near the stall in the aforementioned experiments. NASA Langley Research Centre [73] provides the computational validation results using the CFD codes available with them. Drag data is affected by the Reynolds number, $C_{D,0}$ at 3 and 6 million Reynolds number has a 10% difference between them, latter being the smaller. In order to compare the drag results for the fully turbulent case, tripped experimental results are more appropriate. C_p vs x/c data and hence the lift data are not affected more with the change in the Reynolds number as it can be seen in the Fig. 4.3. Ladson data is chosen for comparison of force data of fully turbulent simulation. Out of all these experimental results

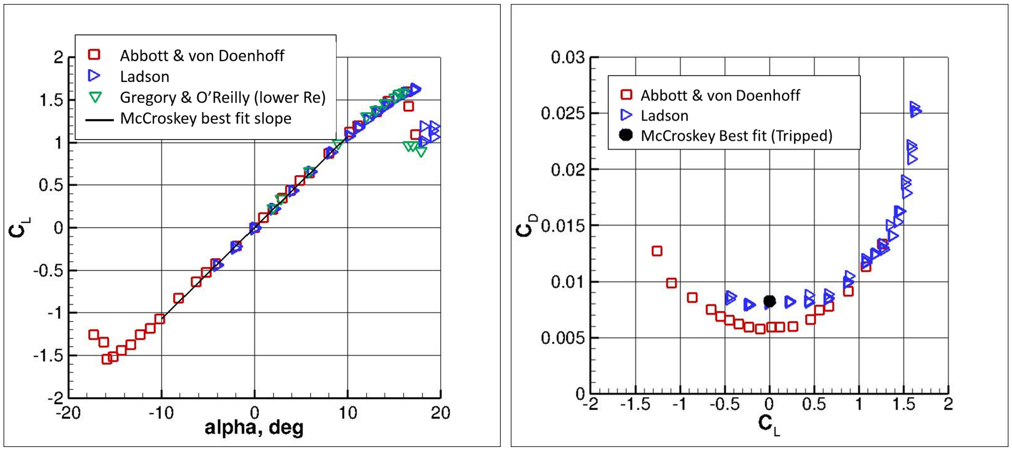

(a) (b)

Figure 4.2: Experimental results of (a) C_l vs AoA ($\alpha°$) (b) C_d vs C_l [73]

Ladson et. al did not resolve the peak upper surface pressure at the leading edge. Whereas the Gregory and O'Reilly data of coefficient of pressure at Reynolds number 3 million are well resolved. However there are differences in Gregory and Ladson data for 10 and 15 degrees AoA until x/c $\simeq 0.1$. For C_p vs. x/c comparison, Gregory data is selected as they are more likely to be 2-D and suitable for validation.

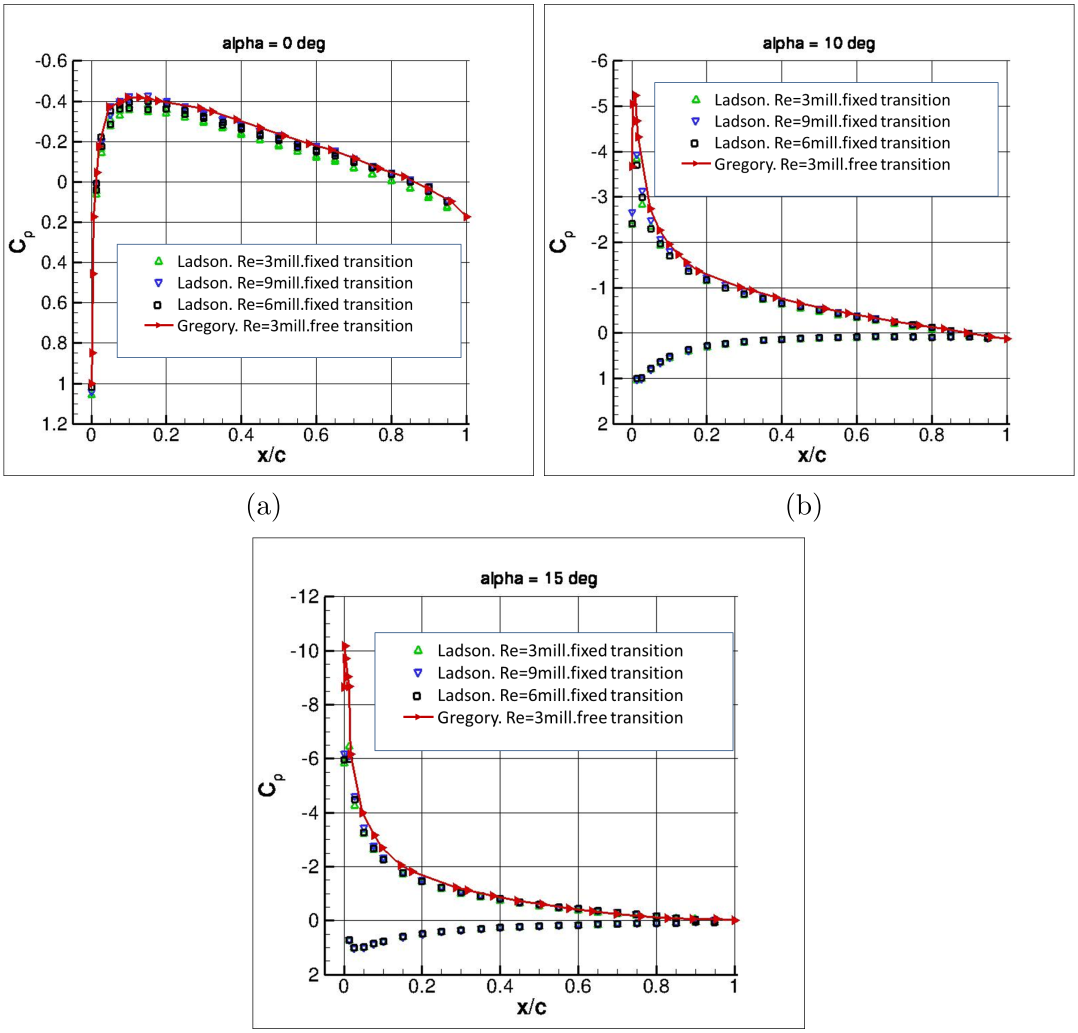

(a) (b)

(c)

Figure 4.3: NACA 0012 experimental results of C_p vs x/c (a) $\alpha = 0$ ° (b) $\alpha = 10$ ° (c) $\alpha = 15$ ° [73]

4.3.2 Validation of Transition k-kl-omega model

For the validation of the Transition k-kl-omega model, NACA 63209 and RAE 2822 experimental cases are selected.

NACA 63209

This airfoil is selected because, NACA 6 digit airfoils were designed for keeping the laminar portion maximum, over the surface of the airfoil [74], for reducing the drag. Another reason is that, the geometry of this airfoil is similar to that of the outboard airfoil and NACA 63 digit airfoils are still in use [75]. NACA 63209 experimental results are available at Reynolds number of 3, 6 and 9 million [70]. The results at Reynolds number of 15, 20 and 25 million are given by Laurence et.al [76]. The measurement of lift was done by the difference in the pressure reaction upon the ceiling and the floor of the wind tunnel. Whereas, the drag measurement was done by the wake-survey method. Only lift and drag coefficient are given in the report and the results at Re = 20 million are shown in Fig. 4.4.

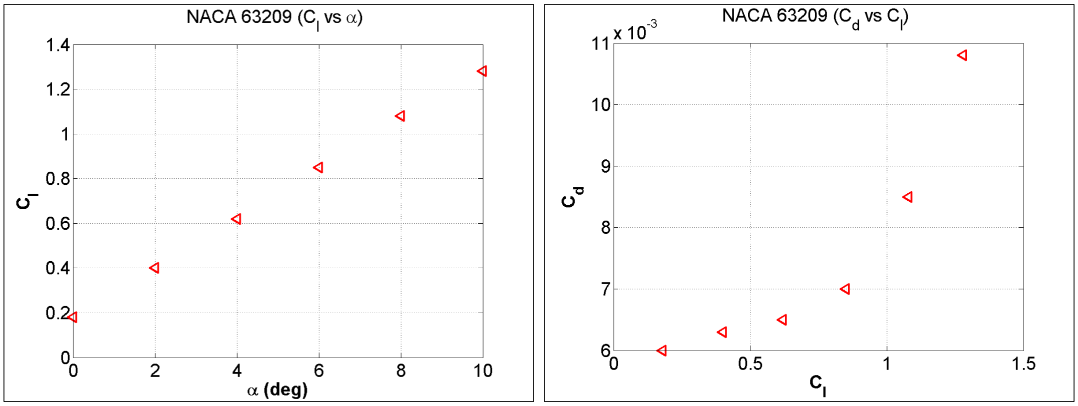

(a) (b)

Figure 4.4: Experimental results of NACA 63209 (a) C_l vs AoA ($\alpha°$) (b) C_d vs C_l [76]

RAE2822

The experimental results of the RAE 2822 are given by Cook et.al [77] in J. Barche's "AGARD advisory report" [78]. Results at different Mach number are given, of which the results having laminar portion are selected. Pitot static probes were used for measurement of the pressure variation over the surface of the airfoil. The experimental results at Reynolds number 5.7 million for the coefficient of normal force (C_n) are given rather than coefficient of lift (C_l) as shown in Fig 4.5.

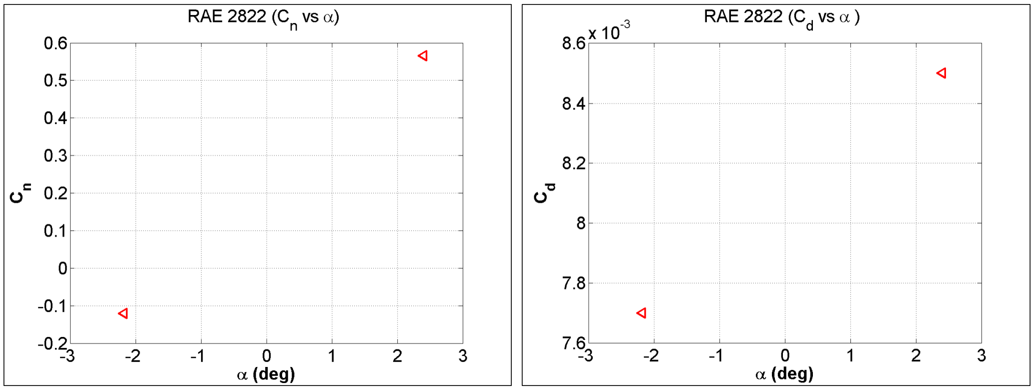

(a) (b)

Figure 4.5: Experimental results of RAE 2822 (a) C_l vs AoA ($\alpha°$) (b) C_d vs C_l [77]

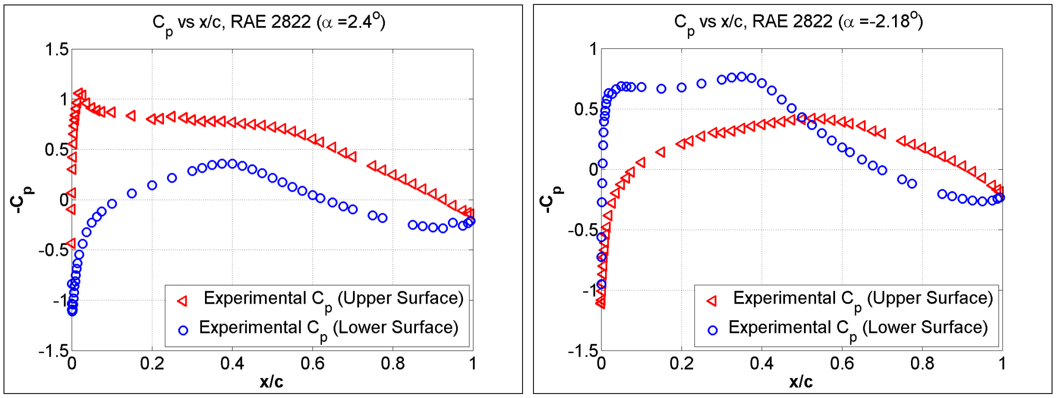

(a) (b)

Figure 4.6: RAE 2822 experimental results of C_p vs x/c (a) α= 2.4° (b) α= -2.18° [77]

4.4 Modeling geometries of present study

4.4.1 Modeling NACA 0012, Size & Shape of Domain

The coordinates of the NACA 0012 airfoil are slightly adjusted from the original coordinates so that the airfoil closes at chord length = 1 with a sharp trailing edge. Exact NACA 0012 formula is given by Eq. 4.2.

$$y = \pm 0.6[0.2969 * \sqrt{x} - 0.1260 * x - 0.3516 * x^2 + 0.2843 * x^3 - 0.1015 * x^4] \quad (4.2)$$

With this equation, Leading Edge(L.E) is at x=0 and the sharp T.E. location is at x=1.008930411365. Airfoil is created in a normal way and then it is scaled down exactly by 1.008930411365. The result is a perfectly scaled copy of the 0012, with maximum thickness of 11.894 %(approx.) relative to its chord. As the name suggest NACA 0012 has a maximum thickness of 12% relative to the blunted chord. It is also having maximum thickness 11.894% when the chord is extended to 1.0008930411365. Thus, the revised definition is:

$$y = \pm 0.594689181[0.298222773 \times \sqrt{x} - 0.127125232 \times x$$

$$-0.357907906 \times x^2 + 0.291984971 \times x^3 - 0.105174606 \times x^4] \qquad (4.3)$$

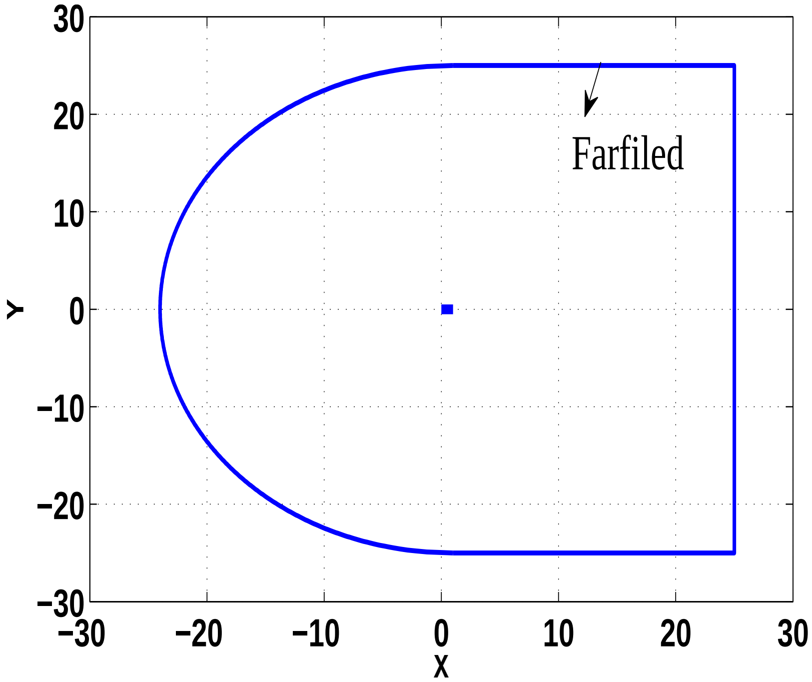

Figure 4.7: Domain Size is $25\bar{c}$

The size of domain taken by the Langley Research Center is 500 chords [73]. Whereas, Kaul et.al [4] and Eleni et.al [79] uses a domain size of 25 chords as shown in the Fig. 4.7. Shape of the flow domain is another consideration that needs to be taken before running the simulations. The flow domain of the NACA 0012 case is ”C-shaped” in front of the airfoil and has a rectangular shape behind the airfoil [73]. This shape is used by other researchers as well [79] [80] [81] . Domain shape and size that will be used for all the airfoils in the present study is

"C-shaped" flow domain and 25 chord size around the airfoil.

4.4.2 Modeling NACA 63209 and RAE 2822

NACA 63209

The coordinates of NACA 63209 are given by Laurence et.al [76]. The airfoil has a leading edge radius of 0.631 and the slope of radius through leading edge is 0.0842. Using CATIA V5, the geometry of airfoil was generated and new coordinates were extracted from the ".igs" file generated in CATIA V5. The coordinates were imported to GAMBIT software and by using Non-Uniform Rational Basis Spline (NURBS) surface of the airfoil was generated.

RAE 2822

Coordinates of RAE 2822 are given by Cook et.al [77] in J. Barche's "AGARD advisory report" [78]. AGARD report provided two types of coordinates, designed airfoil coordinates and measured airfoil coordinates. Due to manufacturing limitations, there is a negligible error in magnitudes of measured and designed airfoil coordinates.The measured coordinates are used for the present study. The coordinates were imported to GAMBIT and using the NURBS command, surface of the airfoil was generated. Since the number of coordinates were enough to produce a smooth surface of the airfoil, increasing the number of coordinates was not needed.

4.4.3 Modeling Baseline and VCCTEF

Non-Uniform Rational Basis Spline (NURBS) is used in representing and generating, surfaces and curves. It offers good flexibility and preciseness for handling both modeled shapes and analytic shapes (shapes that have common mathematical formula) [82].The available coordinates of the outboard airfoil are 32 while creating the edge using NURBS command in the GAMBIT (according to the user guide [83] and on-line available tutorials) the coordinates proved to be insufficient for having a smooth curve.

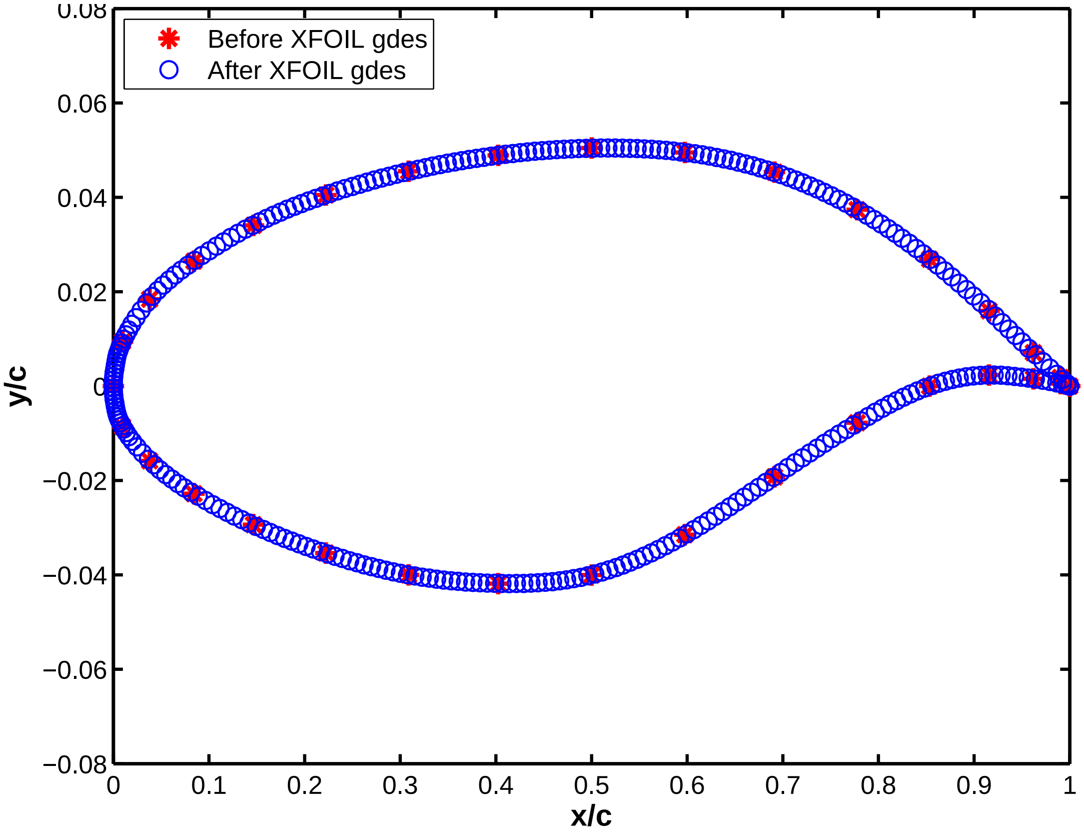

Figure 4.8: Baseline Coordinates

In order to have a smooth curve, it was required to increase the number of coordinates. Directly using the MATLAB commands like “splines” and “interp” helped in increasing the coordinates but near the leading edge, they failed to increase the coordinates which can be used to make smooth leading edge nose. To analyze the airfoil geometries the commonly used programming codes are XFOIL [84] and Eppler's PROFILE [85]. XFOIL has the option of "GDES" and "CADD", which are simple to use and increases the maximum number of coordinates to 300. The various GDES commands can be used for altering leading edge radius, thickness and camber-line etc. Along with CADD routine/command they suffice for most geometry modification tasks to increase the number of coordinates.

In order, to make geometry of VCCTEF one can either use CATIA V5 or GAMBIT preprocessor. However, obtaining the coordinates list was important and was done by using the simple mathematical rules which translates the (x, y) cartesian coordinates to polar coordinates (r, θ).

$$\begin{aligned} r &= \sqrt{x^2 + y^2} \\ \theta &= \arctan x/y \end{aligned} \tag{4.4}$$

Once we get θ, the next thing is to subtract the required angle of deflection (δ) from θ ($\theta_{new} = \theta - \delta$). θ_{new} is re-transformed to the cartesian coordinates by using,

$$\begin{aligned} x &= r\ cos(\theta_{new}) \\ y &= r\ sin(\theta_{new}) \end{aligned} \tag{4.5}$$

Fig. 4.9 shows the comparison of baseline coordinates along with the various VCCTEF coordinates. To get the coordinate for VCCTEF 123, flap is rotated about three center of deflections (O, A and B) as shown in the Fig. 4.10. Initially, the flap is rotated about O by 1°. This transforms the coordinates A, B and T.E to A', B' and T.E' respectively. Then the flap is rotated about A'(by 2°), this gives the new coordinates B" and T.E". Finally rotation of 3° about B" gives T.E"'.

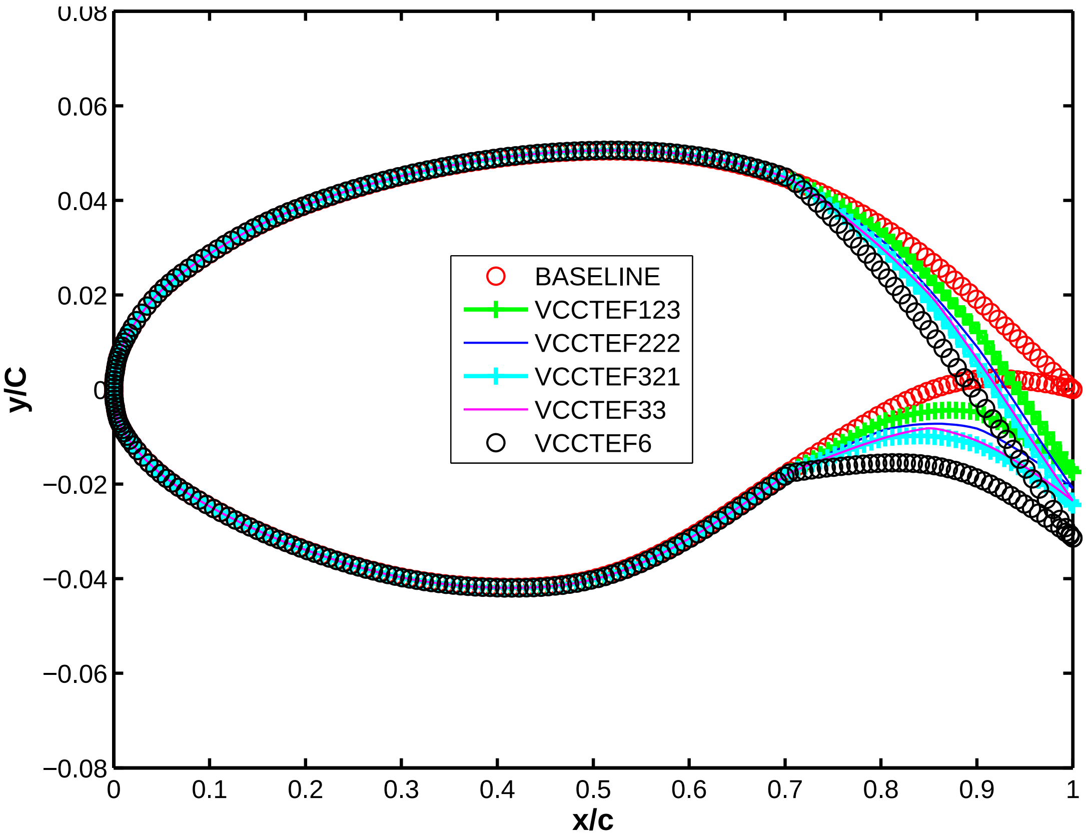

Figure 4.9: Coordinates comparison of Baseline and VCCTEF (SCALED COORDINATES)

It can be noticed here that, T.E"' is rotated about O by $6°(1° + 2° + 3°)$.

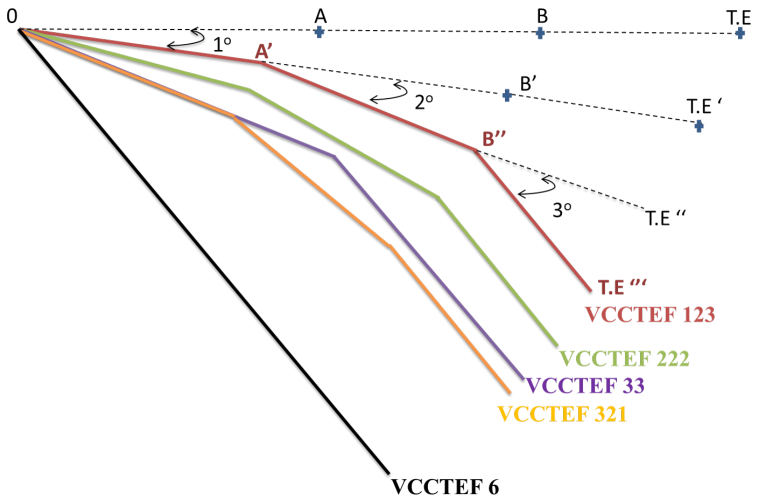

Figure 4.10: Chord Line representation of VCCTEF

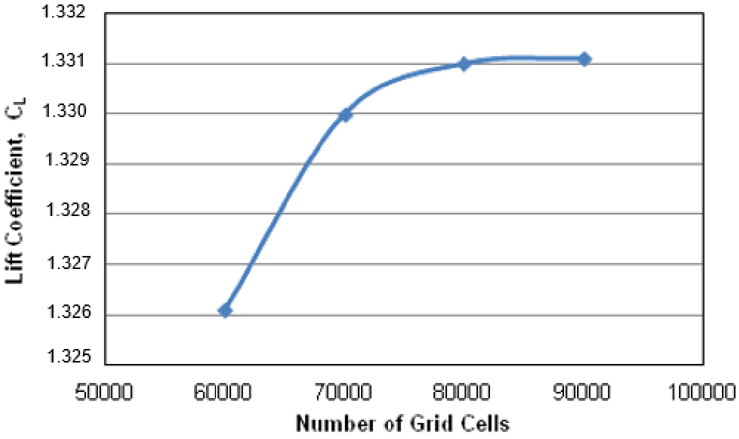

Figure 4.11: C_l vs number of Grid [79]

4.5 Grids Generated

4.5.1 NACA 0012 Grids Generated

Eleni et.al [79] generated results with 80,000 cells and 25 chord fluid domain taking care of the refinement of the grid near the wall/ airfoil in order to envelop the boundary layer. Fig 4.11 shows that from 60000 cells to 90000 cells the variation in coefficient of lift is less than 0.5 %.

The various grids studied are given in the Fig. 4.12. Gambit preprocessor was used in creating these meshes and all the grids generated were map type quad elements. With the increase in the number of cells, the percentile error in lift coefficient was reduced as shown in Fig. 4.11. As more than 80,000 cells gave good results [79], the number of cells in Mesh 3 were increased directly to 99000 from 15750 cells (Mesh 2). For Mesh 3, the difference in C_l value is under 2%. The near wall mesh distance for this mesh was 2×10^{-06} m, which gave a $y^+ < 1$. The calculation of y^+ was done by an online calculator [86]. The percentage (%) error in C_l obtained from Mesh 4 was increased compared to Mesh 3 even though the number of cells were increased from 99000 to 105900 cells. This increase in the error is due to change in near wall distance and the boundary conditions. Near wall distance for the Mesh 4 was 1×10^{-4} and boundary conditions used were velocity inlet and pressure outlet. However, increase in error is just under 5 %. Mesh 1 and 2 are coarse grids, whereas Mesh 3 is the finest grid (relatively), having least near wall distance.

F.L = First length, I.C = Interval count,L.L = Last Length, I.S =Interval Size

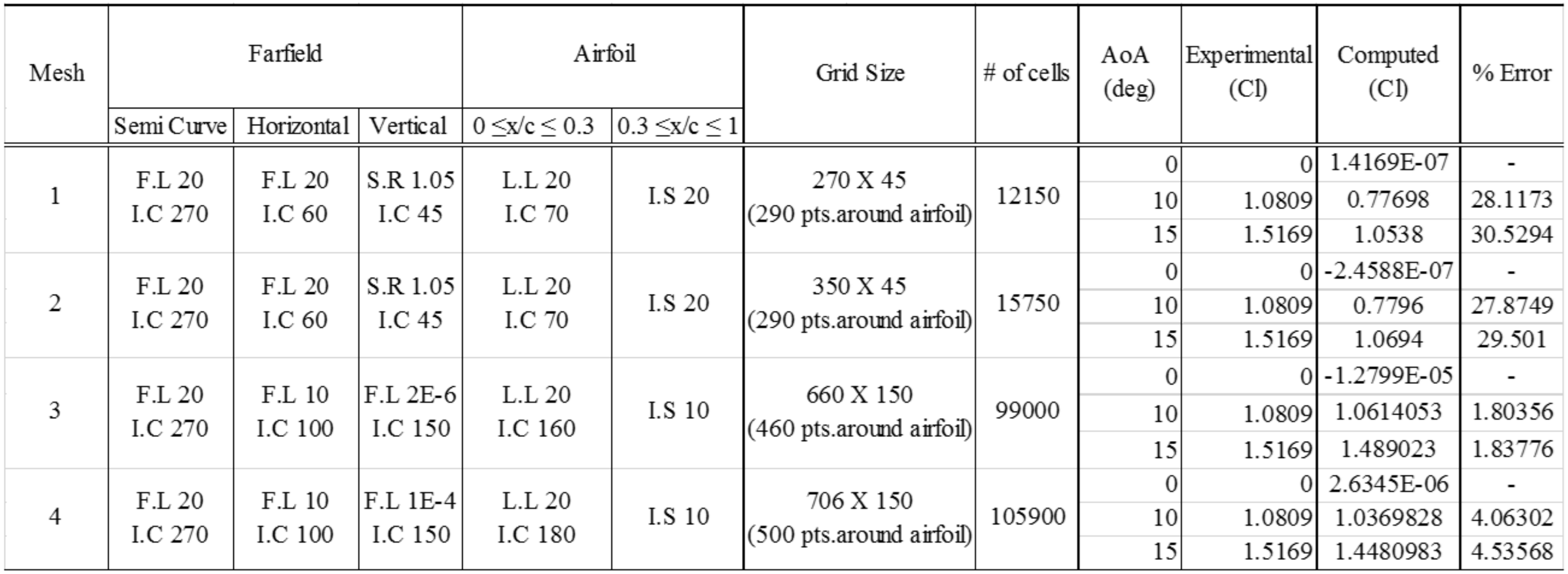

Mesh	Farfield			Airfoil		Grid Size	# of cells	AoA (deg)	Experimental (Cl)	Computed (Cl)	% Error
	Semi Curve	Horizontal	Vertical	0 ≤x/c ≤ 0.3	0.3 ≤x/c ≤ 1						
1	F.L 20 I.C 270	F.L 20 I.C 60	S.R 1.05 I.C 45	L.L 20 I.C 70	I.S 20	270 X 45 (290 pts.around airfoil)	12150	0	0	1.4169E-07	-
								10	1.0809	0.77698	28.1173
								15	1.5169	1.0538	30.5294
2	F.L 20 I.C 270	F.L 20 I.C 60	S.R 1.05 I.C 45	L.L 20 I.C 70	I.S 20	350 X 45 (290 pts.around airfoil)	15750	0	0	-2.4588E-07	-
								10	1.0809	0.7796	27.8749
								15	1.5169	1.0694	29.501
3	F.L 20 I.C 270	F.L 10 I.C 100	F.L 2E-6 I.C 150	L.L 20 I.C 160	I.S 10	660 X 150 (460 pts.around airfoil)	99000	0	0	-1.2799E-05	-
								10	1.0809	1.0614053	1.80356
								15	1.5169	1.489023	1.83776
4	F.L 20 I.C 270	F.L 10 I.C 100	F.L 1E-4 I.C 150	L.L 20 I.C 180	I.S 10	706 X 150 (500 pts.around airfoil)	105900	0	0	2.6345E-06	-
								10	1.0809	1.0369828	4.06302
								15	1.5169	1.4480983	4.53568

Figure 4.12: Grids Studied for NACA 0012

As discussed in the Sec. 4.4.1, the flow domain for the created meshes is "C-shaped". Simulations were done with coarser mesh and then the mesh was made fine.

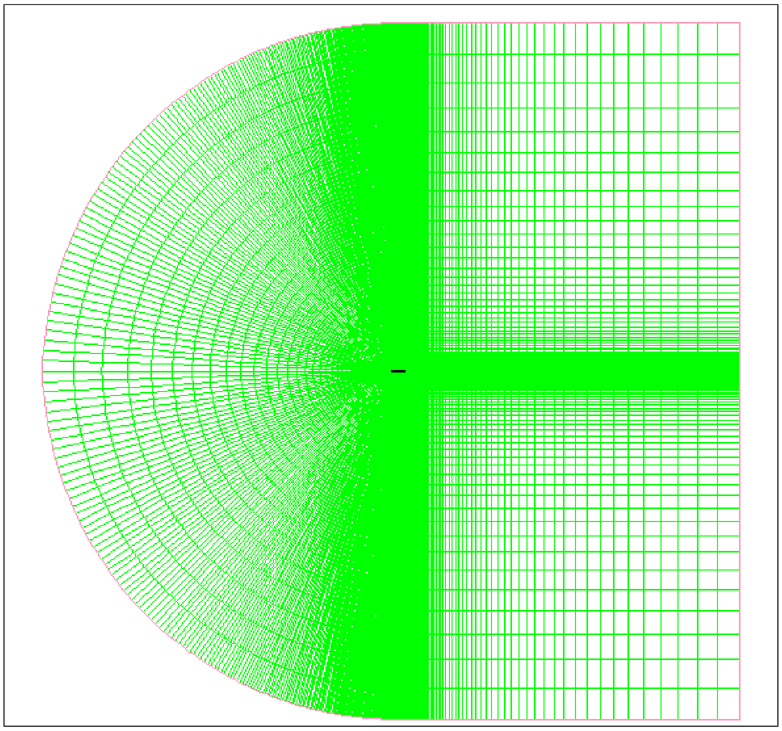

Figure 4.13: Present figure of mesh 660 X 150 (460 points around airfoil 25 $\bar{c}$)

Mesh 3 is shown in Fig. 4.13 , which has a flow domain of 25 $\bar{c}$ around the airfoil in all directions. The size of the grid is 660 X 150, with 460 node/mesh points around the airfoil . All the grids generated are along the same line because of the validated grid methodology. (The results of this can be seen in Chapter 5: Results and Discussion). Fig. 4.14 shows a representative near-body mesh of the NACA 0012 airfoil. The mesh figure shows a fine mesh near the airfoil body and as the mesh moves away from the airfoil the size of the mesh increases.

A comparison of the mesh for the airfoils, with and without trailing edge thickness is shown in Fig. 4.15. Mesh requirement for the airfoil with trailing edge

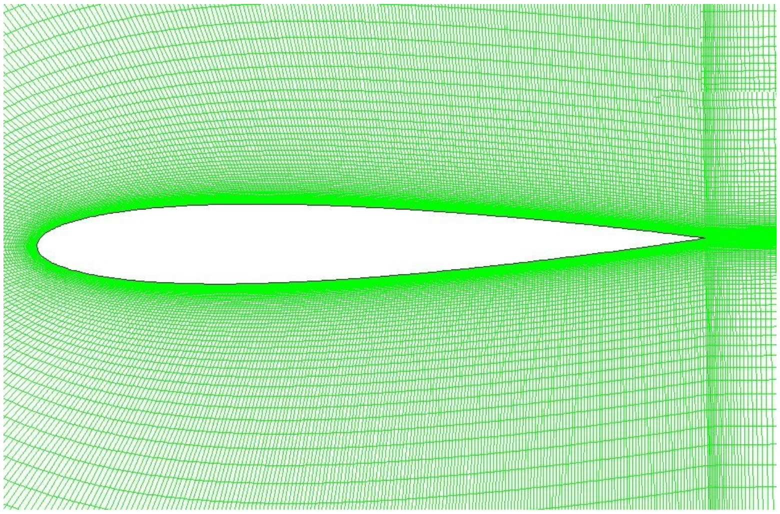

Figure 4.14: Near airfoil mesh for NACA 0012

thickness is higher compared to the one which does not have a trailing edge thickness. The number of cells in the mesh of the airfoil with trailing edge thickness as shown in Fig. 4.15(b) is 155400, which shows an increase in 56400 cells (57 % increment) compared to Mesh 3 shown in the Fig . 4.15(a). This increase in the number of cells increases the computation time.

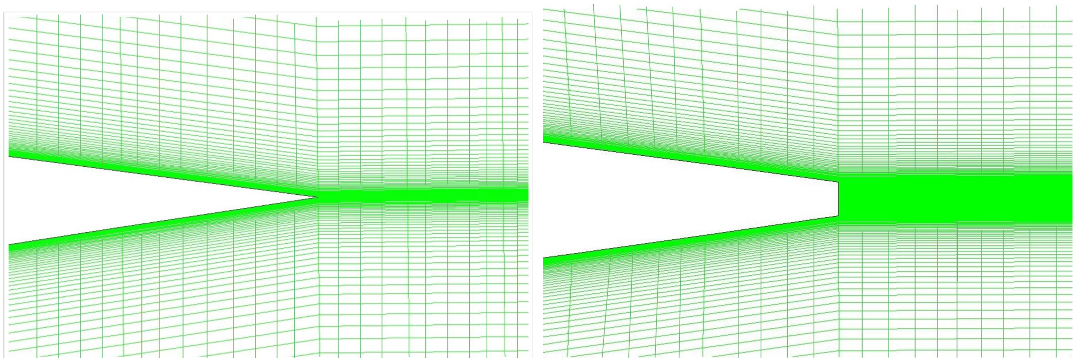

(a) (b)

Figure 4.15: NACA 0012 Mesh (a) with no T.E. thickness (b) with T.E. thickness

Table 4.1 shows the percentage (%) error after using the airfoil with trailing edge thickness. Since it is showing high error relative to Mesh 3 and uses more

Table 4.1: NACA 0012 with T.E thickness

# of cells	AOA (deg)	EXPERIMENTAL CL	COMPUTATIONAL CL	% ERROR
155400	10	1.0809	1.141429	5.599843

computation time, use of this airfoil for validation was discontinued.

4.5.2 NACA 63209 AND RAE 2822 Grid

NACA63209

The grid requirement for Transition k-kl-omega model was given in Section 4.2.2. NACA 63209 airfoil was generating negative cell area while using the same grid generation methodology as NACA 0012. A new type of mesh generation methodology is adopted, in which a small face is created around and near the airfoil. This face is split from the rest of the flow domain using "FACE SPLIT" command in GAMBIT. Mesh was generated separately in the split face and rest of the face. The grid points were adjusted properly such that, the mesh progressed smoothly from one face to another.

Table 4.2: Grid of NACA 63209

Airfoil	Grid Size	# of cells
NACA 63209	1122 × 200 (922 points around airfoil)	224400

Table 4.2 show the grid size generated for NACA 63209, where 1122 represents the number of grid points on the flow domain and 200 represents the number of grid points normal to the airfoil. Total of 922 points were taken on the airfoil

surface.

RAE 2822

A grid generation methodology similar to that described for NACA 63209 is used for generating the mesh of RAE 2822.

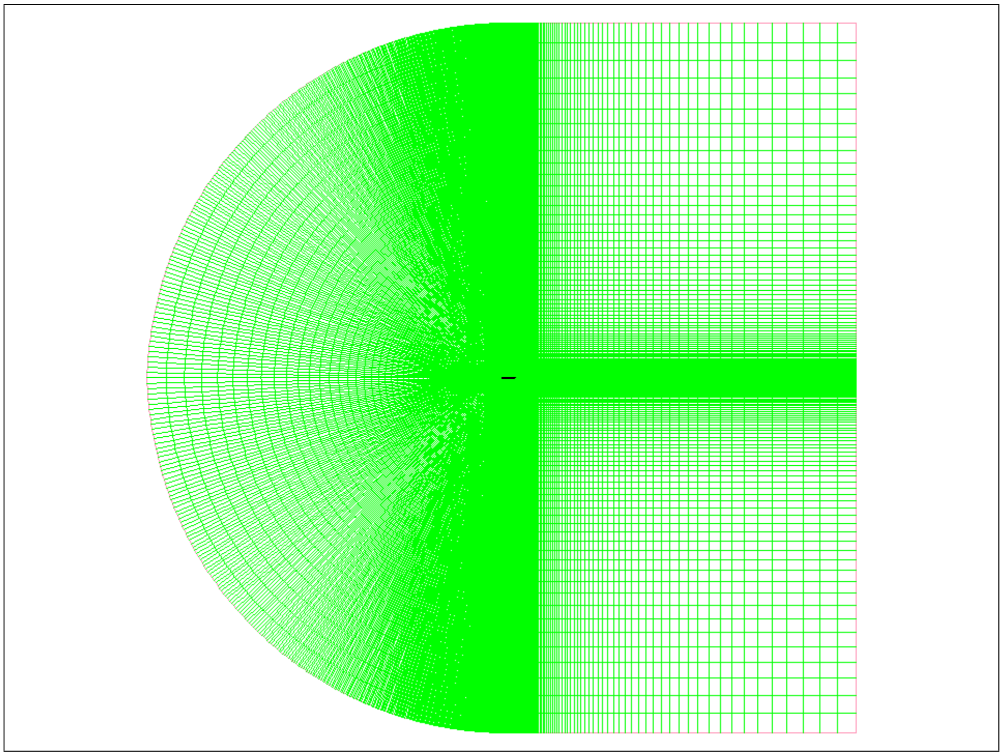

Figure 4.16: RAE 2822 mesh, 1122 × 200 (922 points around airfoil)

Fig. 4.16 show a complete mesh around RAE 2822. The flow domain size for this mesh is 25 $\bar{c}$. The grids are concentrated near the airfoil and in the wake region behind the airfoil.

Fig. 4.17 shows the mesh around RAE 2822 airfoil.The number of grid points around airfoil is 922.

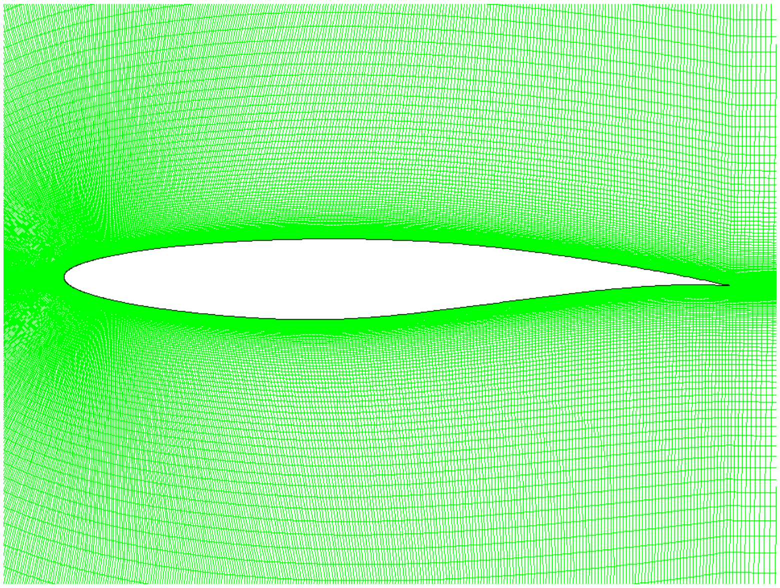

Figure 4.17: Near-body mesh of RAE 2822 airfoil

4.5.3 Baseline & VCCTEF Grids

Two types of grids are generated for baseline and VCCTEF configurations; One for the computational analysis with fully turbulent SA model, and another for the computational analysis with Transition k-kl-omega model. Grid for fully turbulent simulations uses mesh generation methodology of NACA 0012 airfoil and the grid for transition simulation uses the methodology of NACA 63209 and RAE 2822.

Grids for Fully Turbulent Analysis with SA model

Table 4.3 shows the grid size and te number of cells. All the grids were generated by quadratic elements and type pave. GAMBIT preprocessor was used for making these meshes. A complete grid shape of the baseline is shown in the Fig. 4.18.

Fig. 4.19 shows the representative near-body meshes of the baseline and various VCCTEF configurations. In order to take consideration of flap, the number of grid points is slightly increased.

Table 4.3: Grids of Baseline & VCCTEF

Airfoil	Grid Size	# of cells
Baseline VCCTEF 123 VCCTEF 222 VCCTEF 321 VCCTEF 33 VCCTEF 6	692 X 150 (492 pts. on airfoil surface)	103800

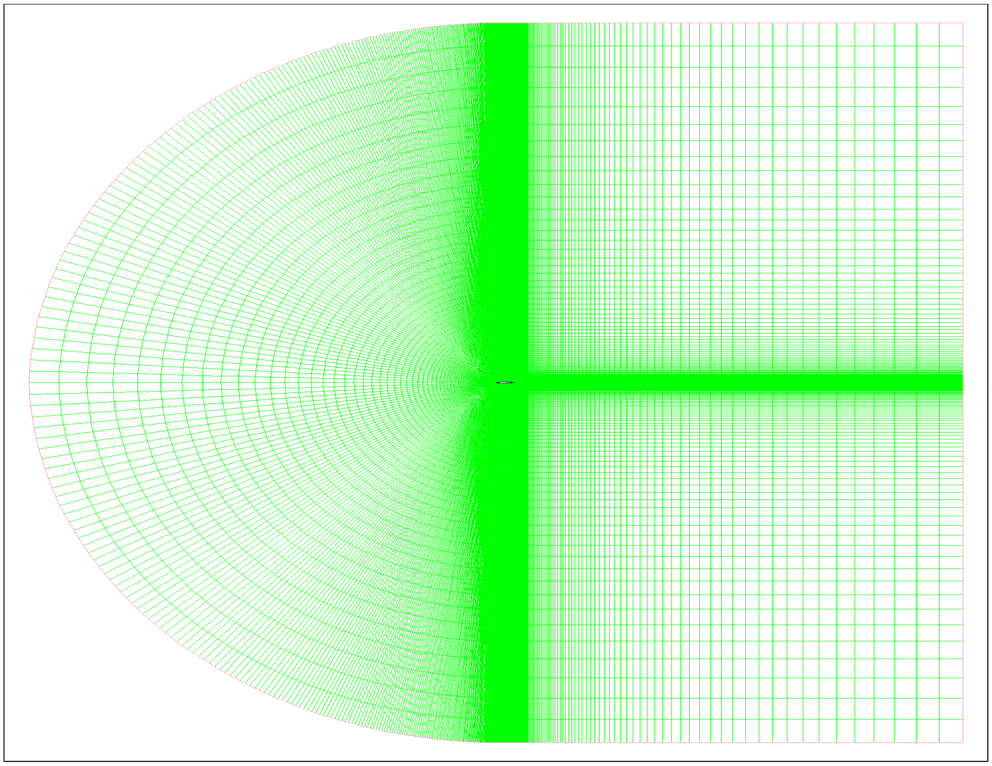

Figure 4.18: Full Grid of Baseline[692 × 150 (492 pts. around airfoil)]

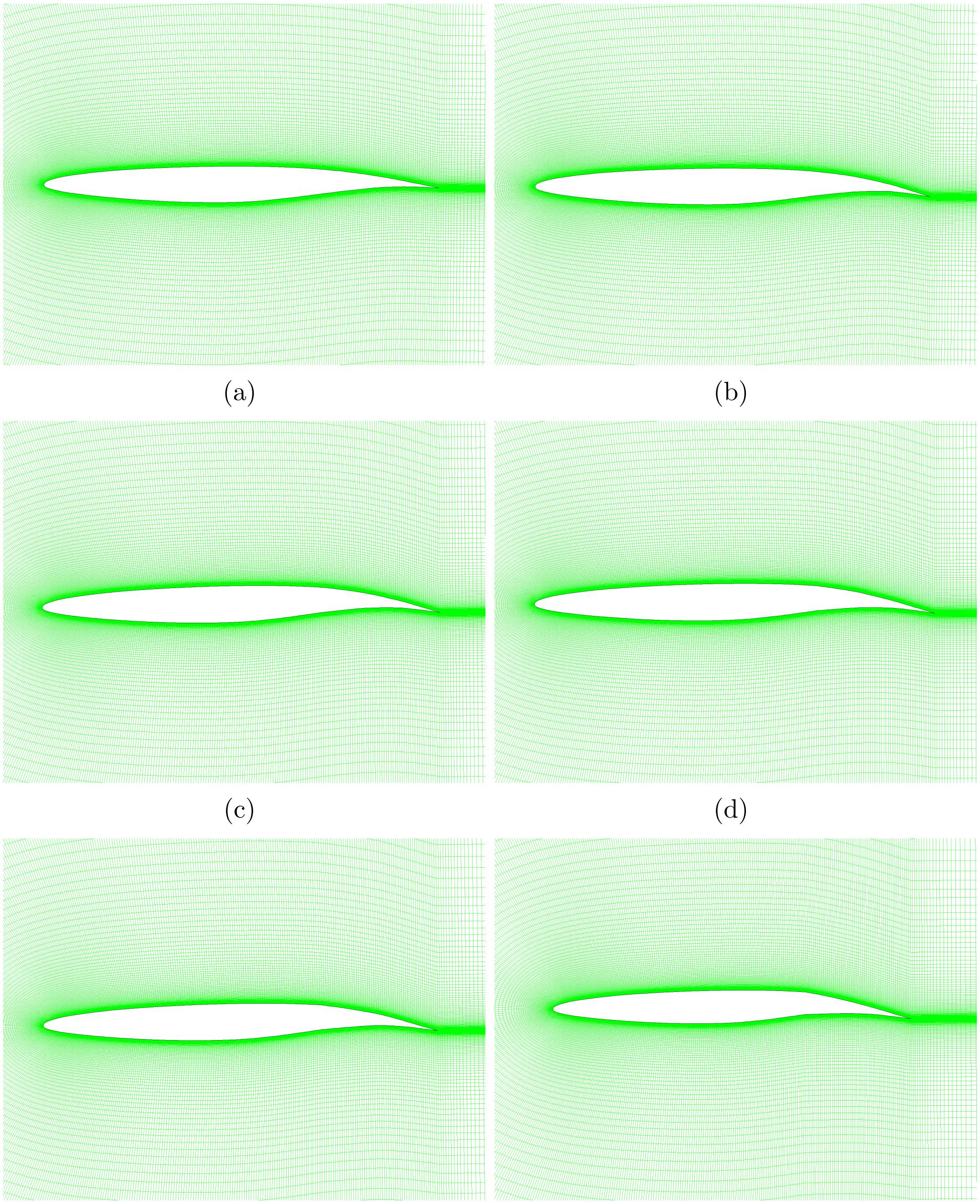

(a)

(b)

(c)

(d)

(e)

(f)

Figure 4.19: Representative Near-Body Mesh 692 × 150 (492 points on airfoil surface) (a) Baseline (b) VCCTEF 123 (c) VCCTEF 222 (d) VCCTEF 321 (e) VCCTEF 33 (f) VCCTEF 6

Grids for computational analysis with Transition k-kl-omega model

Table 4.4 shows the size of the grids and the number of cells. The number of cells are increased relative to the fully turbulent grid.

Table 4.4: Grids of Baseline & VCCTEF (Transition Analysis)

Airfoil	Grid Size	# of cells
Baseline VCCTEF 123 VCCTEF 222 VCCTEF 321 VCCTEF 33 VCCTEF 6	1122 × 200 (992 pts. on airfoil surface)	224400

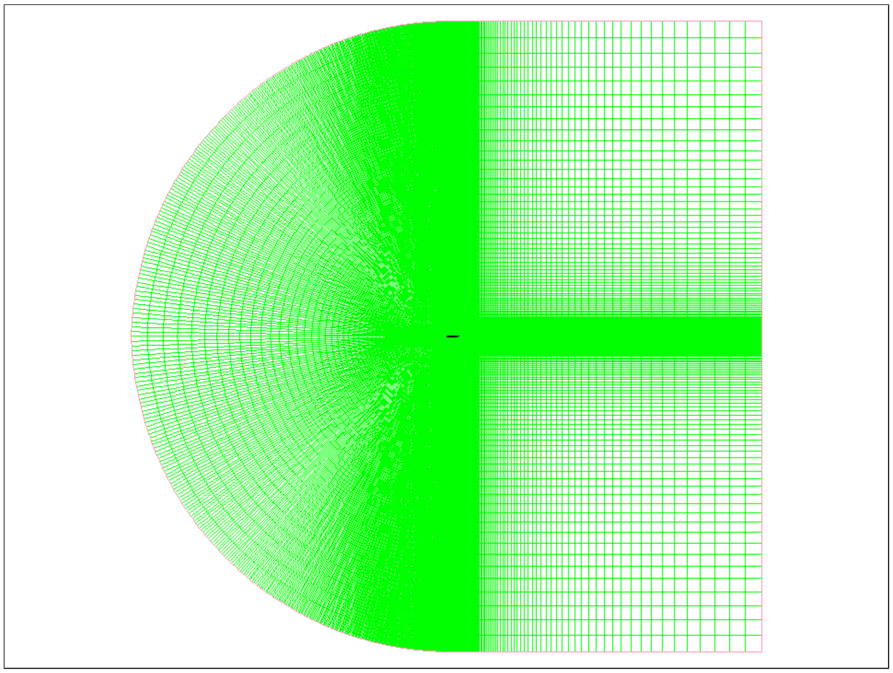

Figure 4.20: Full grid of baseline [1122 × 200 (922 pts. around airfoil)]

Fig. 4.20 shows the complete grid around the baseline. The grid was made finer near the airfoil and in the wake region.

4.6 Simulation in FLUENT

4.6.1 Flight conditions

Simulations of VCCTEF were performed at Reynolds number of 21.6×10^6 and atmospheric conditions at 10,000 m were considered. The conditions of the atmosphere are taken from US standard atmospheric values [87] given in Standard atmosphere charts available on-line [88].These are a subset of International standard atmosphere but under a different name. Table 4.5 shows the standard atmosphere values gives, Reynolds number 21.3277×10^6 (at M = 0.7 & x= 3.587 m).

Table 4.5: U.S STANDARD ATMOSPHERE

Geo-potential Altitude above Sea Level (h) (m)	Temperature T (^{0}C)	Absolute Pressure (P) (N/m^2)	Speed of Sound (a) m/s	Density ρ (kg/m^3)	Dynamic Viscosity (μ) (Ns/m^2)
10000	-49.90	26500	299.5	0.4135	$1.458 \times {*10^{-5}}$

In order to get the Reynolds number = 21.6×10^6 at M = 0.7 and x = 3.587 m, we change the viscosity to 1.4396×10^{-5} Ns/m^2.

4.7 Boundary condition

If the static conditions and free-stream Mach number are known, then boundary condition can be modeled at free stream by pressure far-field conditions in ANSYS FLUENT. To find the flow variables at the boundaries, pressure far-field boundary condition utilizes Riemann invariants (characteristic information). Hence, it is called as a characteristic boundary condition. This study uses pressure far-field conditions at all the domain boundaries.

No-slip boundary condition on the wall i.e. on airfoil and roughness constant 0, keeps the fluid and airfoil in contact.

4.8 Conclusion

The geometry of NACA 0012, NACA 63209, RAE 2822, Outboard airfoil (baseline) and various VCCTEF configurations was made in GAMBIT using NURBS. The coordinates for each of them were generated or taken from various reference according to the requirement. Based on the guidelines of grid generation and by proper consideration of near wall distance, two types of grids are generated one for validation of fully turbulent SA model and another for validation of Transition k-kl-omega model. NACA 0012 airfoil is chosen for fully turbulent SA model validation. Whereas, NACA 63209 and RAE 2822 airfoil are chosen for validation of Transition k-kl-omega model.

CHAPTER 5

RESULTS OF FULLY TURBULENT SIMULATION ON BASELINE & VCCTEF

This chapter discusses the validation of fully turbulent SA model using NACA 0012 airfoil. Using the same simulation methodology, Baseline and various VCCTEF configurations were computationally analyzed. It is also shown that compared to Transition k-kl-omega model, SA model is suitable for fully turbulent simulations.

5.1 Validation using NACA 0012

NACA 0012 airfoil has a sharp trailing edge. However, the modified equation was used to close the airfoil at coordinate (1, 0). The simulation was performed at Mach 0.15 and a Reynolds number of 6 million. In order to satisfy both the conditions, the viscosity was changed by using the equation of Reynold's number Eq. 5.1 .

$$Re = \frac{\rho V X}{\mu} \tag{5.1}$$

Here, ρ =1.225 kg / m^3,

$X = 1m.$

$\mu = 1.021 * 10^{-5}$ kg m /s.

This gives V = 52.078 m/s, as a=$\sqrt{\gamma \times R \times T}$=$\sqrt{1.4X287X300}$= 347.188 m/s.

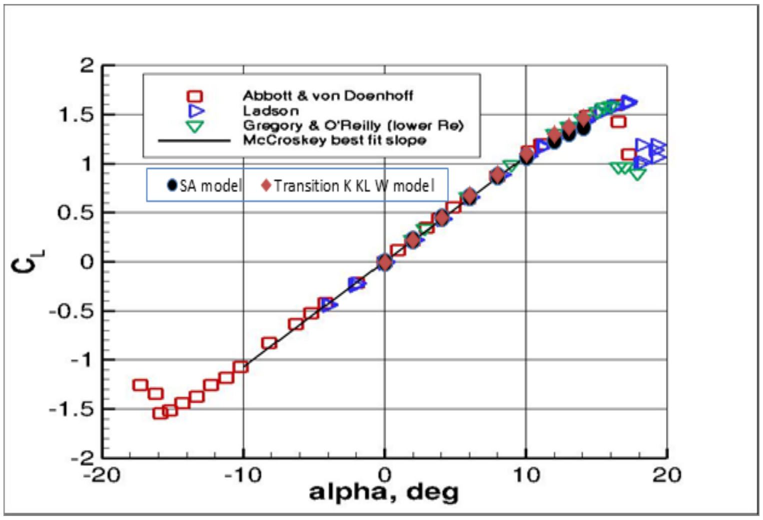

Figure 5.1: Comparison of simulation results C_L vs. α

Figure 5.1 draws a comparison between simulation and experimental results for C_l vs α. One can observe an increase in lift with both SA and Transition k-kl-omega model.

Fig 5.2 shows the variation of C_l vs. α with various grit results of Ladson data (tripped) . The line of best fit is obtained by the Eq. 5.2, which gives the slope.

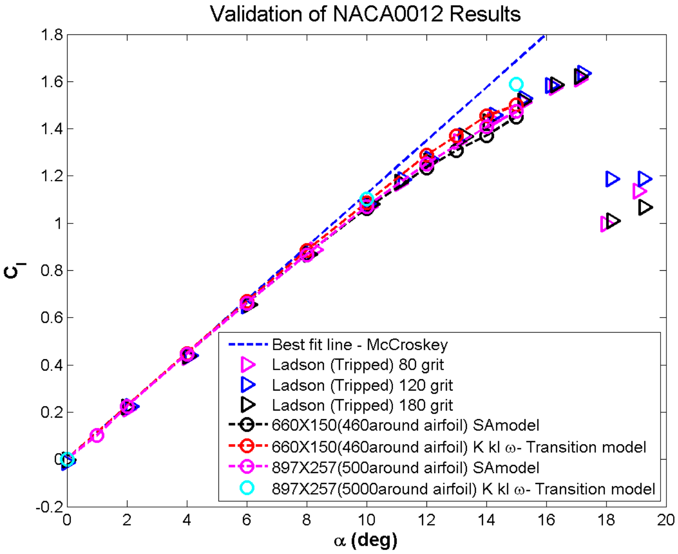

Figure 5.2: C_l vs. α

$$\frac{dC_l}{d\alpha} = 0.1025 + 0.00485 \times \frac{\log_{10}(\frac{Re}{10^6})}{\sqrt{(1-M^2)}} \tag{5.2}$$

Since this airfoil is symmetrical, it is possible to have a straight line passing through the origin. Grid 897 × 257 (513 points around airfoil surface) is NASA Langley Research Center grid, it was available on-line in PLOT3D format. By using the register options in Fluent, the single face grid was divided in two faces; one fluid domain and another airfoil. Same flight conditions as on the validation grid i.e., 660×150 (460 points around airfoil) are applied on it . The results clearly show an agreement of the meshes in C_l value with SA and Transition k-kl-omega model.

Figure 5.3 shows the results of C_D vs. C_L, in which SA model is much closer to Ladson data. Transition k-kl-omega seems to be closer to the Abbot & Von Doenhoff (untripped) data. As we have already discussed in Sec. 4.3, Ladson

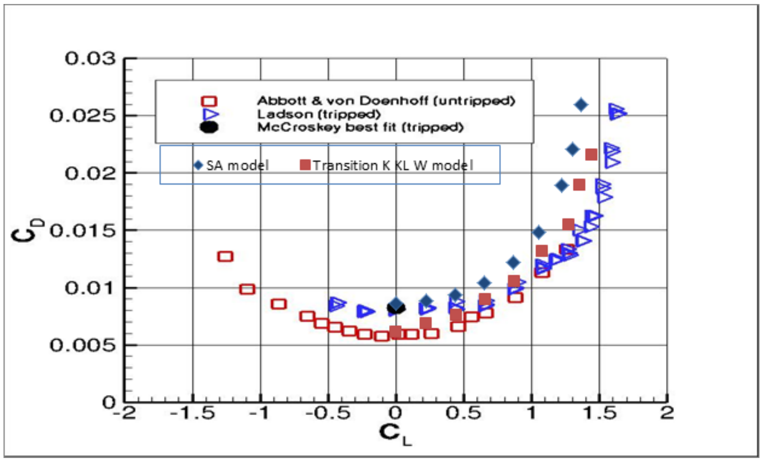

Figure 5.3: Comparison of simulation results C_D vs. C_L

(tripped) data are more appropriate for validation while using fully turbulent model. The grid used for this comparison is 660 x 150 (460 points around airfoil surface). Fig. 5.4 shows the variation of C_d vs C_l with various Ladson tripped data. Grid 897 X 257 (513 points around airfoil surface), which as discussed earlier, is the same mesh used by NASA Langley Research center for validation case. Simulation in the ANSYS FLUENT gives a variation in the C_d value at higher Angle of Attack (AoA) $\sim 10^\circ$ to 15°. This is because of the difference in the codes. Fig. 5.5 shows the variation of C_d with C_l for only SA model. The NASA CFL3D code seems to be the one in agreement with experimental results, however, using the same mesh in ANSYS FLUENT gives a higher drag. As we have already seen from the variation of C_l with α, all the meshes are in agreement with experimental results. Hence, the error is due to the C_d.

Fig. 5.6 shows the variation of C_d with AoA (α). It can be seen that until 10° the error in C_d is less. As the AoA is further increased, the value of C_d is showing more error than the previous AoA. The reason for this error is the inadequacy of

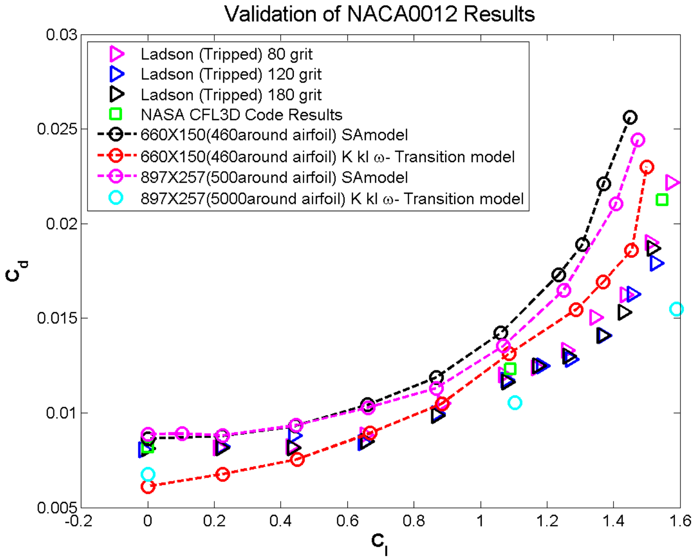

Figure 5.4: C_d vs. C_l

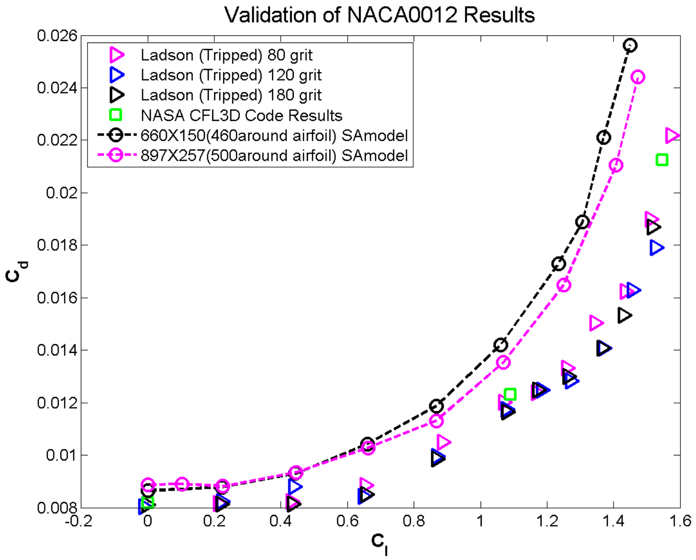

Figure 5.5: C_d vs. C_l (only SA model)

the turbulence models to capture the flow at higher AoA, especially near the stall because the flow tends to behave more in a 3-D manner rather than 2-D. Also, one can not neglect the effects of the wall in closed wind tunnel experiments at higher AoA.

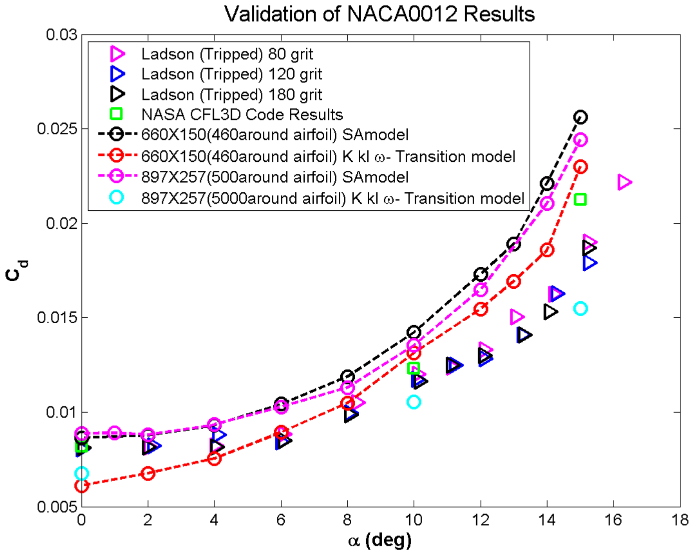

Figure 5.6: C_d vs. α

Fig.5.7 shows the variation of only SA model. The important thing here is that , the trend of experimental results is followed by the computed results.

Experimental data for the comparison of coefficient of pressure (C_p) vs. airfoil chord length (x/c) plots are available for the upper surface only. CFL3D code validates the upper surface very well and we can use their results to validate lower surface data. Figure 5.8 shows the (C_p) vs. x/c plot for 0°. Since the upper and lower surface pressure coefficients are same, we have an overlap in the plot. Figure 5.9 and Figure 5.10 show the C_p vs x/c plots for 10° & 15°. Since lift is increasing, clearly the upper and the lower area of 15° is greater than the 10° plot. The C_p plots are in close agreement with the experimental results and CFL3D results because the lift is entirely dependent on the pressure plots. Hence, the variation in drag is not visible in the C_p vs. x/c plot.

Figure 5.11 shows the comparison of c_f vs. x/c for 0°. This plot has its own

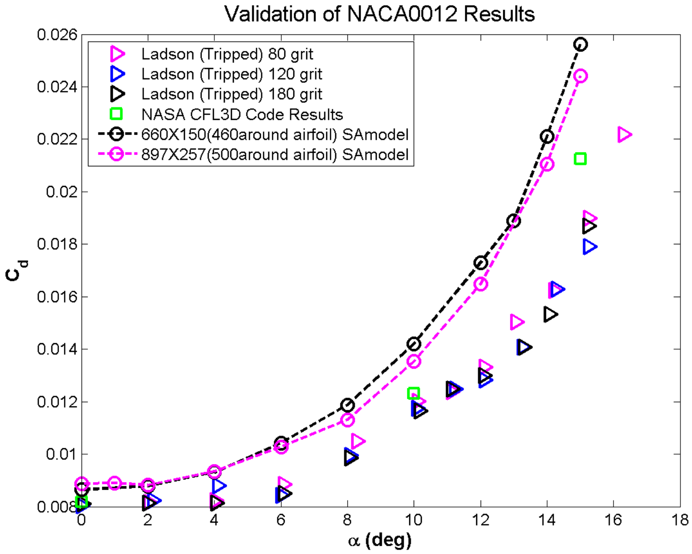

Figure 5.7: C_d vs. α (only SA model)

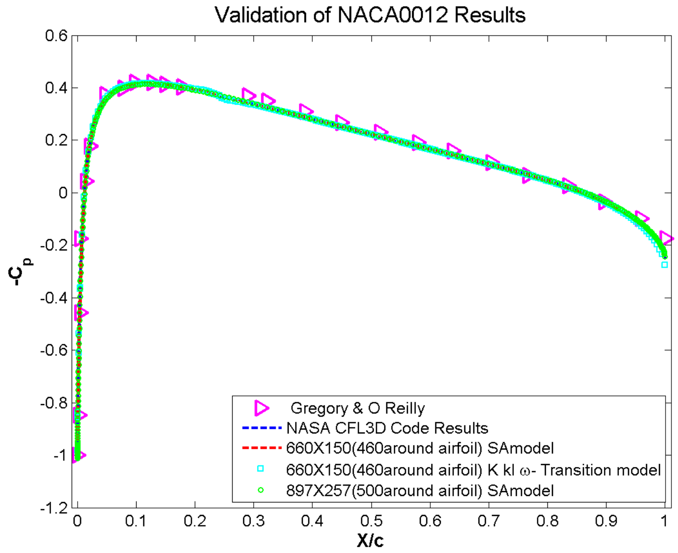

Figure 5.8: C_p vs. x/c 0AoA

importance in validation because of C_d.

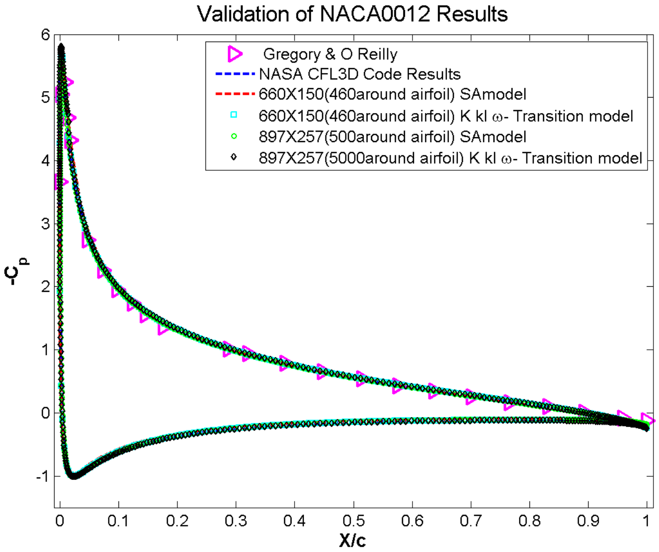

Figure 5.9: C_p vs. x/c 10AoA

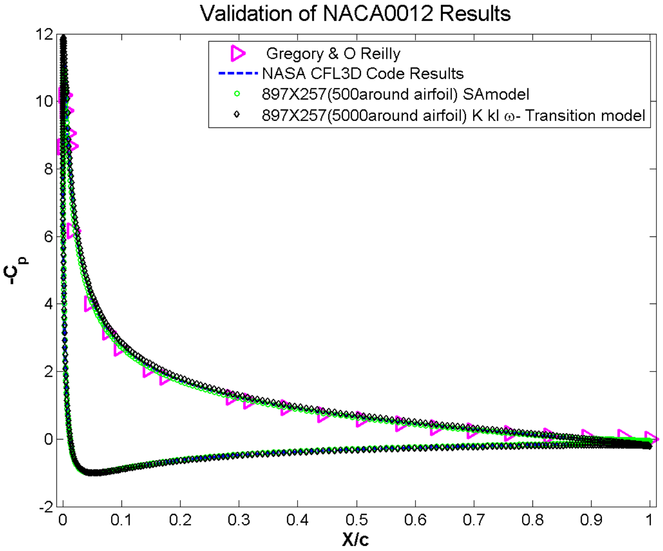

Figure 5.10: C_p vs. x/c 15AoA

5.2 Outboard Airfoil or Kink

5.2.1 Baseline Case

The number of coordinates of the airfoil for outboard was increased by using Xfoil software [89]. The length of chord used for simulation is 3.587 m, as it is near the

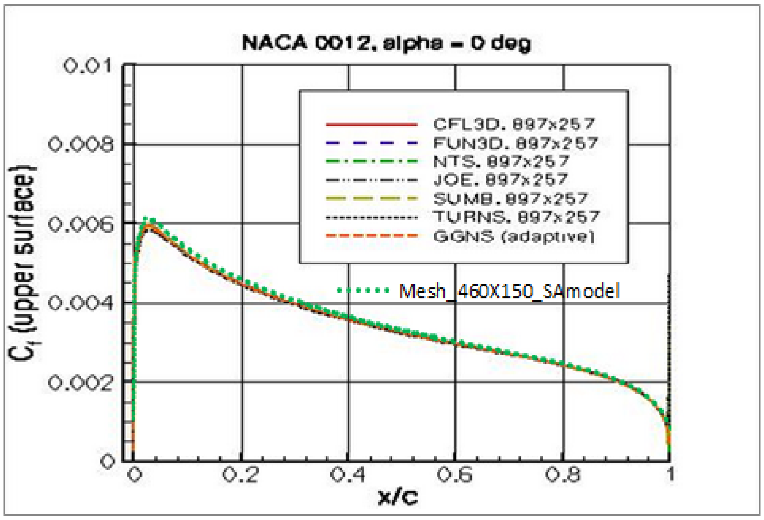

Figure 5.11: comparison of cf vs. x/c at 0AoA

mean aerodynamic center. Besides, it is the chord length at wing break section, where the wing trailing edge breaks from the previous orientation. Fig. 5.12 shows the variation of drag coefficient with respect to the Mach number. As the Mach number increases the value of C_d also increases. Until Mach ($\simeq$) 0.78, the rise of drag coefficient is very small from the initial Mach 0.7, but there is sudden overshoot at Mach 0.8. The rise in the total coefficient of drag C_d is due to the rise in C_{dp} (coefficient of drag due to pressure). This drag is associated with the formation of shock at the upper surface of the airfoil at higher Mach number of 0.8.

$$C_d = C_{dp} + C_{dv} \tag{5.3}$$

Where,

C_d = Total drag coefficient,

C_{dp} = Pressure drag coefficient,

C_{dv} = Viscous drag coefficient.

The contribution of viscous drag coefficient (C_{dv}) is steadily increasing, but there is not much variation in this coefficient relative to its pressure counterpart.

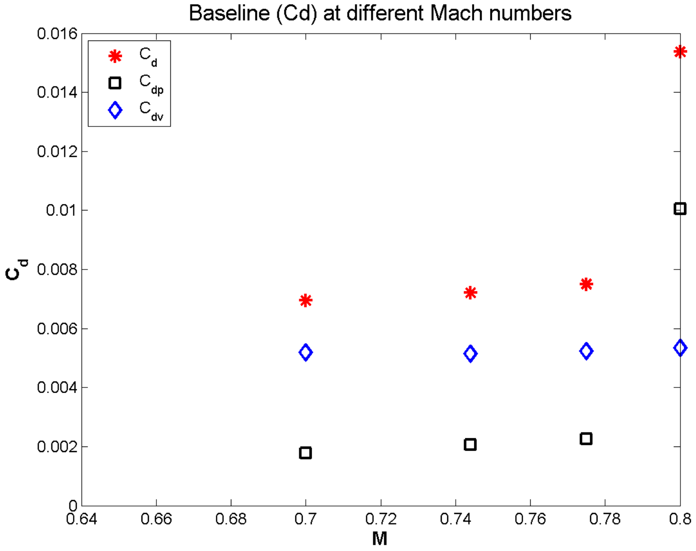

Figure 5.12: Drag divergence study (Baseline)

The lift variation with AoA for different Mach number is shown in the Fig. 5.13. Clearly as the AoA increases, the C_l value increases. The noticeable thing here is increase in slope. From the given figure one can say that,

$$C_{l\alpha}(\text{M}=0.7) < C_{l\alpha}(\text{M}=0.744) < C_{l\alpha}(\text{M}=0.8)$$

Another noticeable thing is the C_l value at 0°. As the Mach number increases the coefficient of lift at 0° also increases.

$$[C_l(\alpha = 0)]_{M=0.7} < [C_l(\alpha = 0)]_{M=0.744} < [C_l(\alpha = 0)]_{M=0.8}$$

$$[\alpha(C_l = 0)]_{M=0.7} \simeq [\alpha(C_l = 0)]_{M=0.744}] \simeq [\alpha(C_l = 0)]_{M=0.8}$$

The value of AoA when C_l is zero is almost same.

Fig 5.14 shows the variation of L/D with respect to Mach number. The value of L/D is increasing steadily. But at M = 0.8, it has suddenly reduced. This is

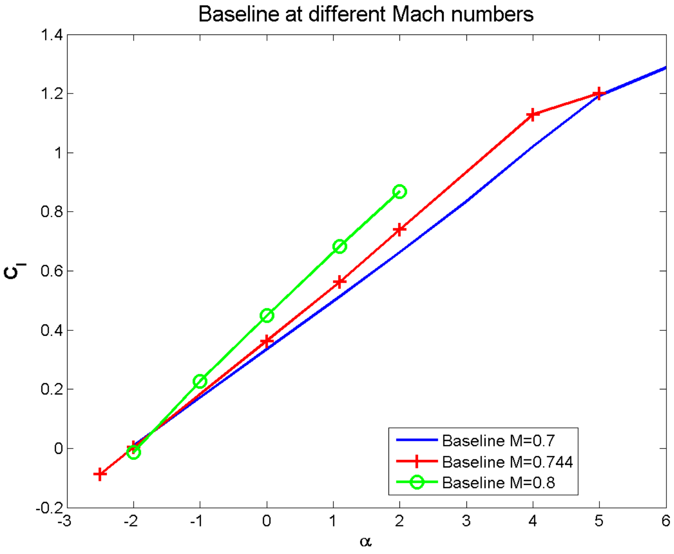

Figure 5.13: C_l vs α (Baseline)

due to the formation of a relatively stronger oblique shock, at around 75 % of chord (this shock formation can be seen in Fig. 5.17). The increase of coefficient of drag due to pressure (C_{dp}) increases the total drag coefficient, thus reducing the L/D ratio.

Fig 5.15 shows the variation of coefficient of pressure (C_p) with x/c at the Mach number 0.7 for different AoA. One can see the variation of AoA until 4°. At AoA 0° the plot follows the HLFC design criteria, in terms of the trend in C_p over the upper and the lower surface. However, there is no shock formation at the upper surface. As the AoA increases, the jump in C_p also increases, near the leading edge. This is due to the formation of the expansion fans near the leading edge. When $\alpha = 0°$, there is a very weak shock formation at x/c $\simeq$ 0.05 and this shock at $\alpha = 1.1°$ becomes slightly stronger. At $\alpha = 2°$, this shock moves aft ($0.05 <$ x/c < 0.1) and when $\alpha = 4°$ this shock is strongest compared to the all

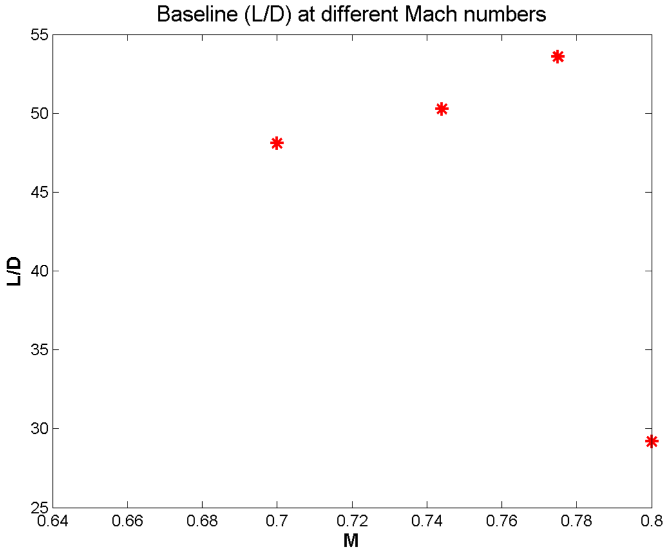

Figure 5.14: Variation of L/D with Mach number(Baseline)

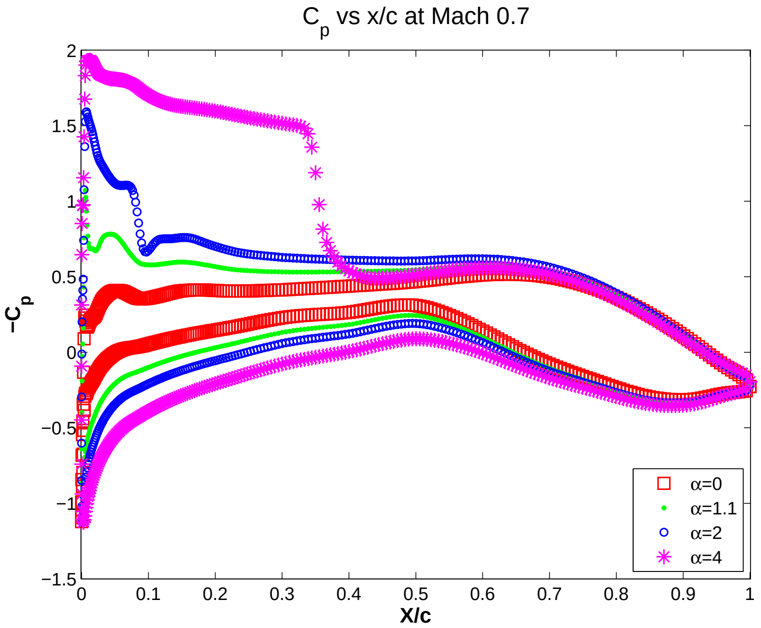

Figure 5.15: C_p vs x/c at M = 0.7

the previous shocks and most aft at x/c $\simeq$ 0.35.

Fig. 5.16 shows the variation of C_p vs x/c at the Mach number 0.744 for different AoA. Here also, plots for AoA until 4° is shown. At AoA 0°, the plot is following the HLFC design criteria in terms of the trend in C_p over the upper and

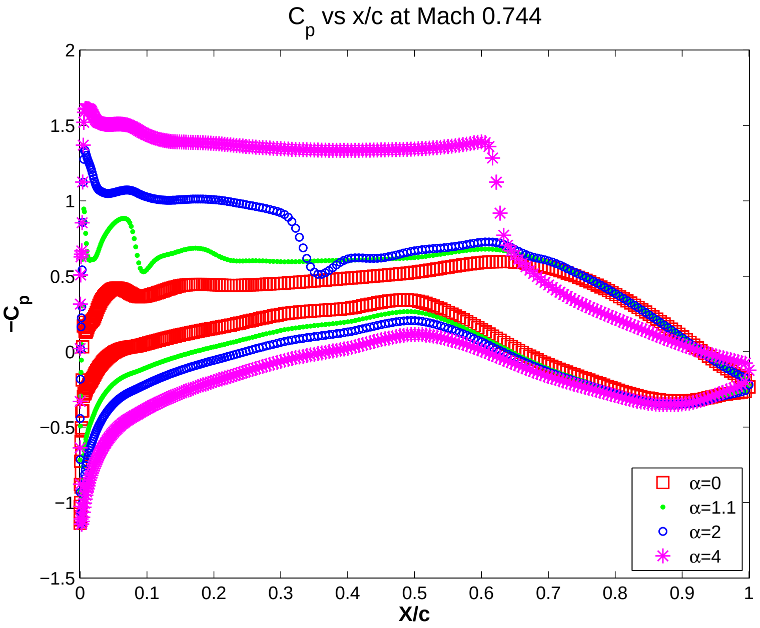

Figure 5.16: C_p vs x/c at M = 0.744

the lower surface. However, there is a very weak shock formation at the upper surface x/c $\simeq$ 0.05, similar to the previous M = 0.7 case. As the AoA increases, the jump in C_p (showing a large reduction in pressure) also increases near the leading edge due to the formation of the expansion fans. The very weak shock formation for $\alpha = 0°$ at x/c $\simeq$ 0.05, becomes slightly stronger for $\alpha = 1.1°$ at 0.05 < x/c < 0.1. For $\alpha = 2°$, this shock moves aft at x/c $\simeq$ 0.3 and when $\alpha = 4°$, this shock is strongest compared to all the previous shocks and most aft at x/c $\simeq$ 0.65. The jump near the leading edge is highest for $\alpha = 4°$.

Figure 5.17 shows the variation of C_p vs x/c at the Mach number 0.8 for different AoA until 2°. At AoA 0°, the plot is following the HLFC design criteria in terms of the trend in C_p over the upper and the lower surface. There is a very weak shock formation at the upper surface at x/c $\simeq$ 0.05 similar to the previous M = 0.7 & 0.744 case. Unlike previous cases, the C_p is following HLFC design

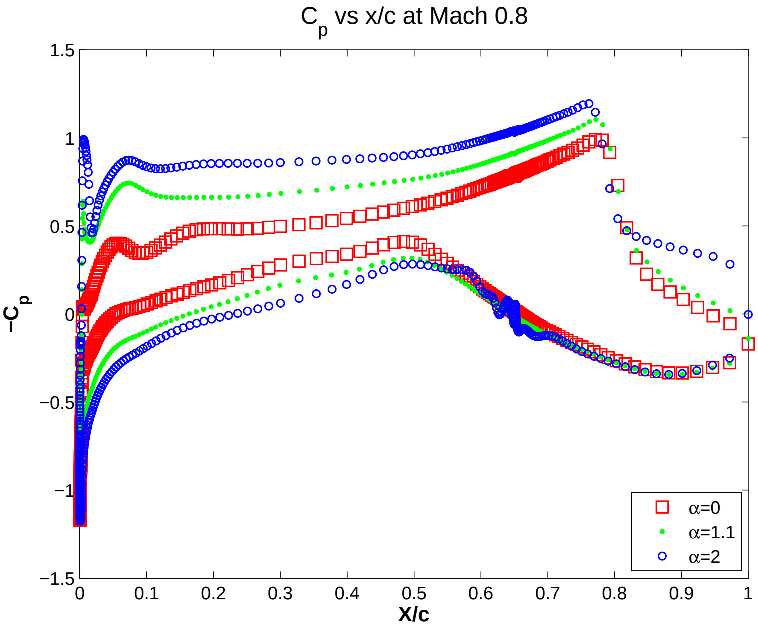

Figure 5.17: C_p vs x/c at M = 0.8

criteria trend line at all the AoA but there is relatively strong shock formation at x/c $\simeq$ 0.75. The jump near the leading edge is highest for $\alpha = 4°$. Unlike the previous cases, there is much decrease in pressure at the leading edge. However, things are settling down quickly under x/c < 0.02.

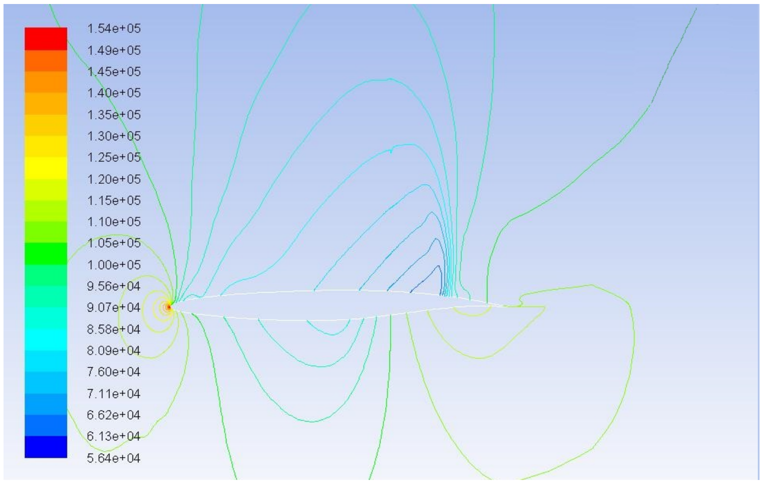

Figure 5.18: Pressure contour 1.1 AoA (M=0.8)

Figure 5.18 shows the contour of static pressure at 1.1°. There is a formation of shock at 75 % of chord($x/c \simeq 0.75$).

Pressure and Mach Contours for the baseline, from AoA $= -2°$ until $2°$ are shown from Fig 5.19 to Fig.5.28

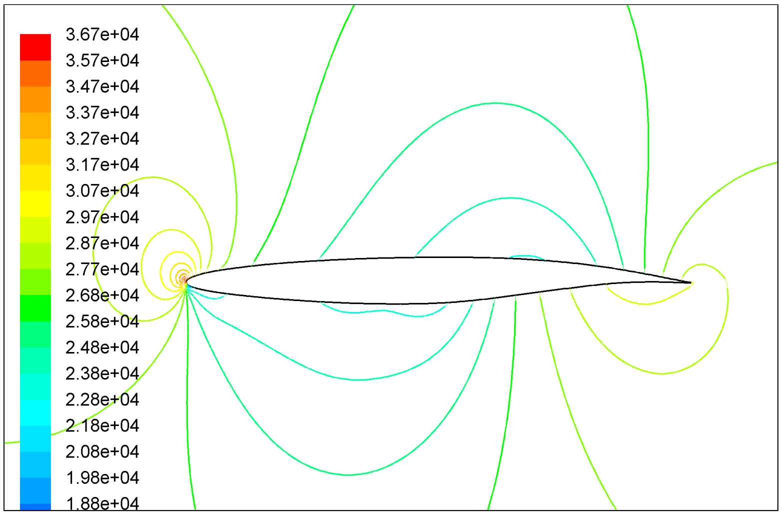

Figure 5.19: Pressure contour of Baseline at α =-2°, M =0.7

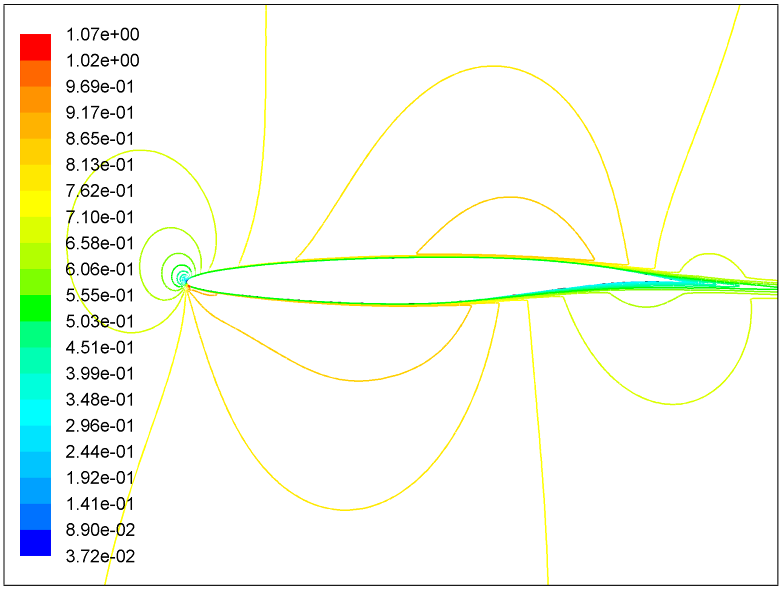

Figure 5.20: Mach contour of Baseline at α =-2°, M =0.7

Fig. 5.19 and Fig. 5.20 shows that the pressure and Mach contour correlates with each other. There is no shock formation on the upper and the lower surface at an AoA = -2° as shown in the Fig. 5.19 and Fig. 5.20

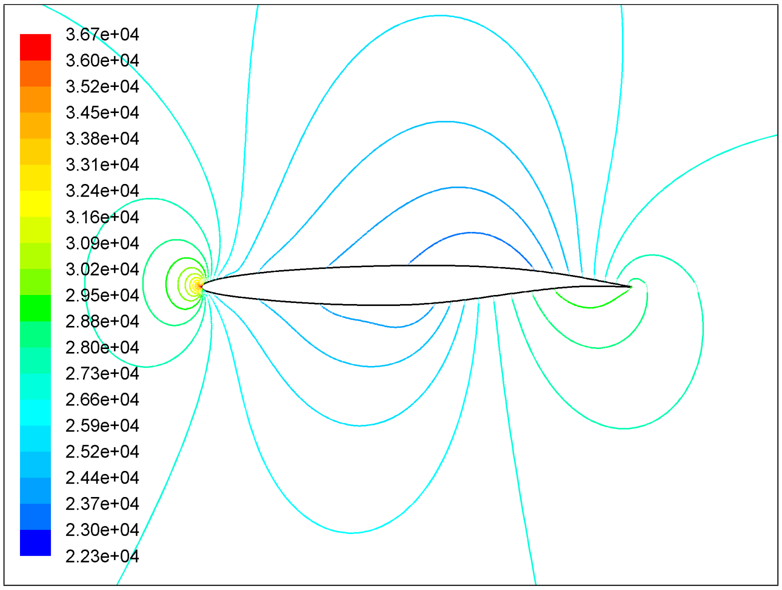

Figure 5.21: Pressure contour of Baseline at α =-1°, M =0.7

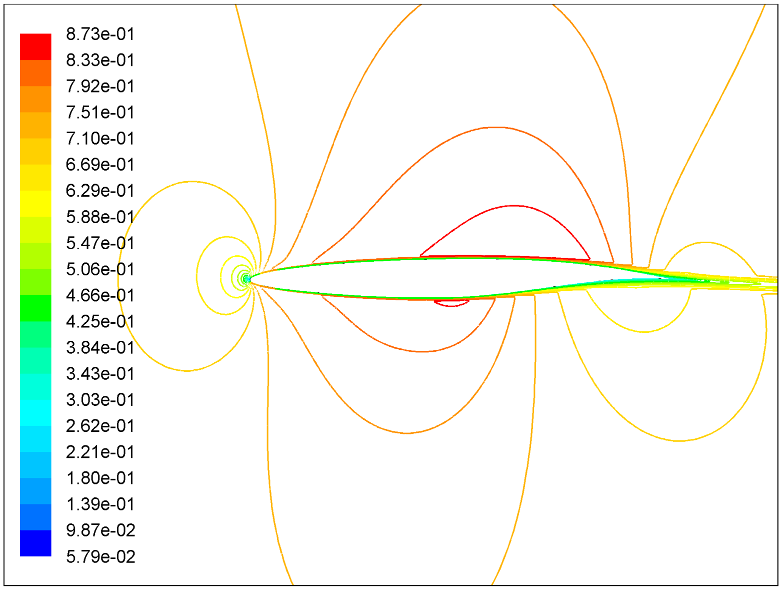

Figure 5.22: Mach contour of Baseline at α =-1°, M =0.7

At AoA = -1° also the pressure and Mach contour shows no shock formation as seen in the Fig. 5.21 and Fig. 5.22. At AoA = 0° the pressure and Mach contours show slight shock formation on the upper surface near the leading edge

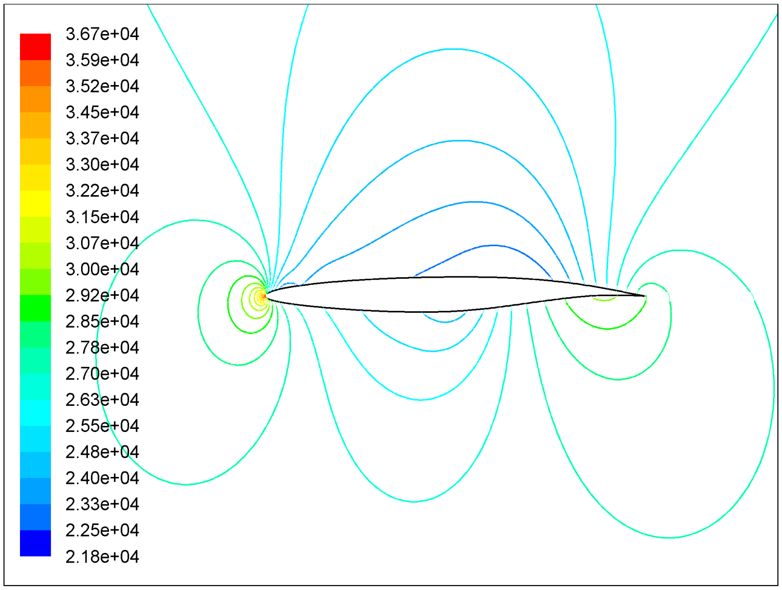

Figure 5.23: Pressure contour of Baseline at α =0°, M =0.7

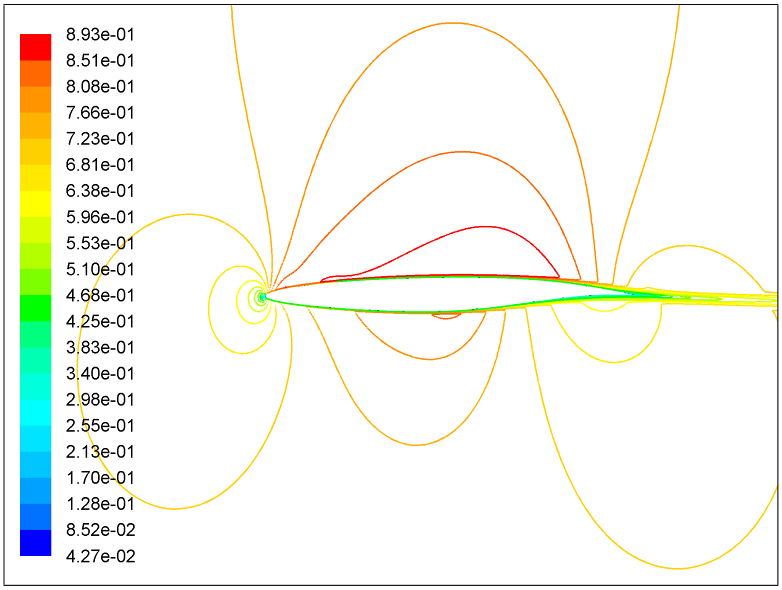

Figure 5.24: Mach contour of Baseline at α =0°, M =0.7

as shown in Fig. 5.23 and Fig. 5.24. This shock moves towards the right as the AoA is increased from 0° to 1.1°. Fig. 5.25 and Fig. 5.26 shows the pressure and Mach contour at AoA = 1.1°. The strength of the shock at this AoA slightly increases compared to 0° case. This is clearly visible in the Fig. 5.15.

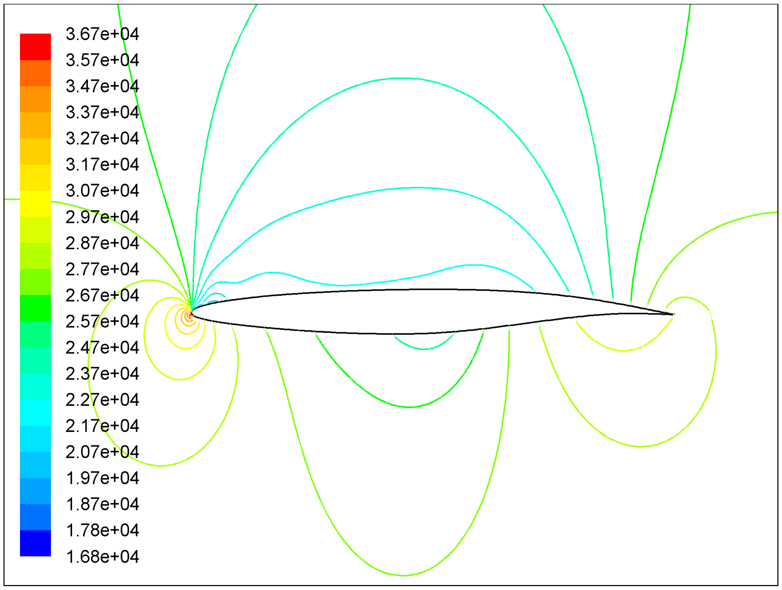

Figure 5.25: Pressure contour of Baseline at α = 1.1°, M =0.7

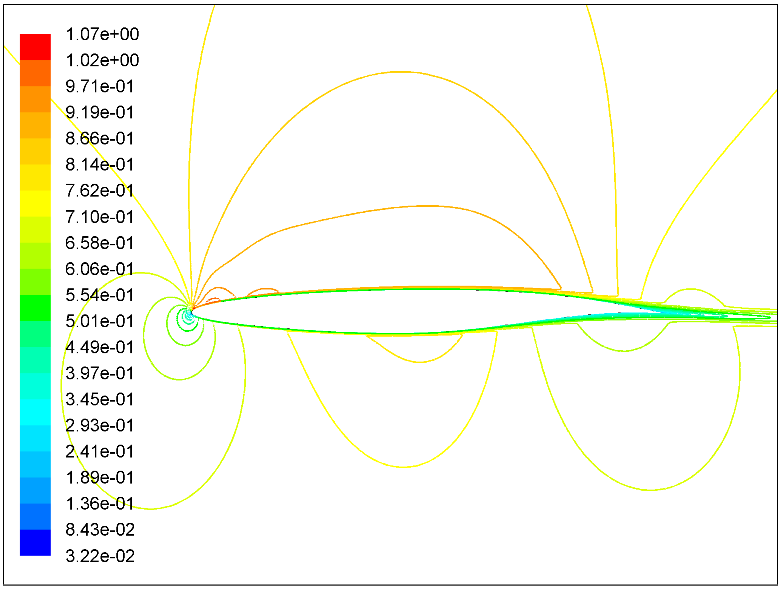

Figure 5.26: Mach contour of Baseline at α = 1.1°, M =0.7

The shock formation is clearly visible on the upper surface of the baseline at AoA=2°, as shown in Fig. 5.27 and Fig. 5.28. This shock formation can also be seen in the C_p vs x/c plot in Fig. 5.15.The shock moves further to the right as the AoA is increasing.

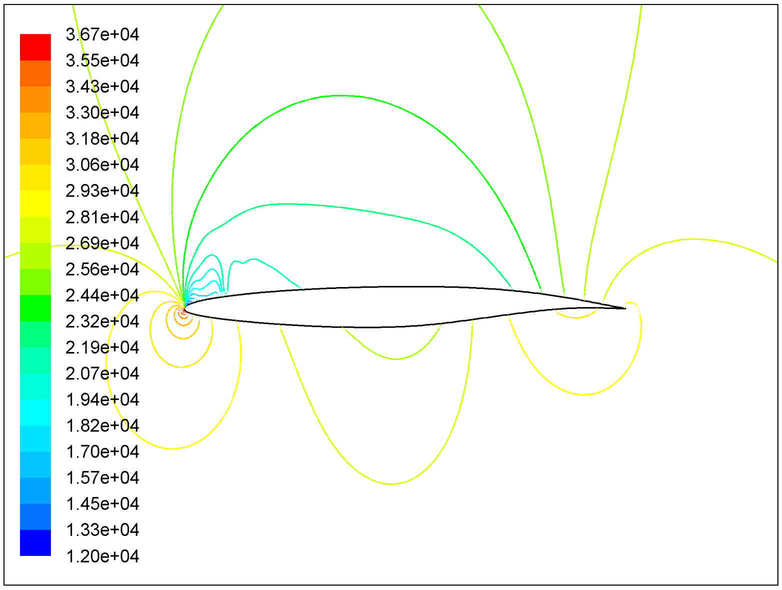

Figure 5.27: Pressure contour of Baseline at α =2°, M =0.7

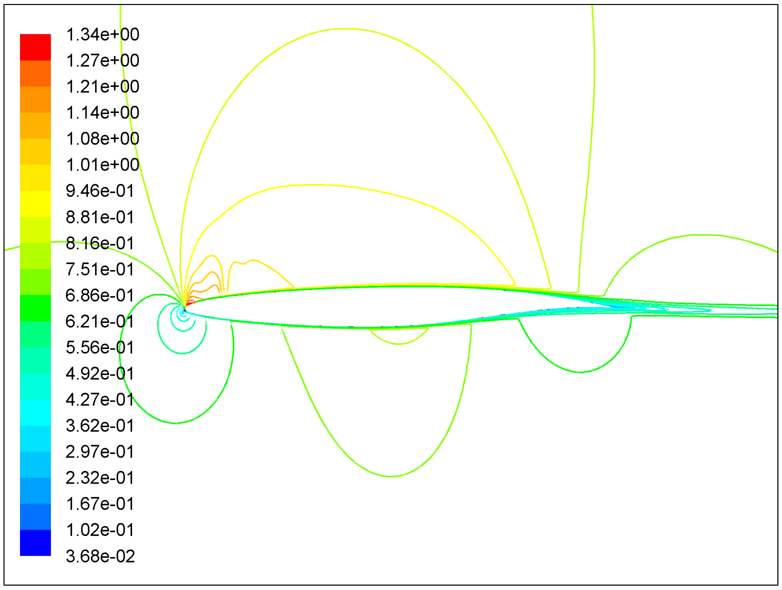

Figure 5.28: Mach contour of Baseline at α =2°, M =0.7

This study aims to find the L/D ratio at various AoA. The values of C_l and C_d are determined and summarized along with their pressure and viscous components in Table 5.1 and Table 5.2

	Drag Coefficient			Fractional Contribution	
AoA	Pressure	Viscous	Total	Pressure	Viscous
-2	0.001531671	0.005098	0.00663	0.231029	0.768970993
-1	0.001465363	0.005167	0.006633	0.220926	0.779073844
0	0.001769581	0.00518	0.00695	0.25462	0.745380485
1.1	0.002532964	0.005134	0.007667	0.330372	0.669628493
2	0.003531482	0.005057	0.008588	0.411202	0.588798001
3	0.007942196	0.004871	0.012813	0.619831	0.380168988
4	0.020218988	0.004614	0.024833	0.814202	0.18579754
5	0.041434205	0.004288	0.045723	0.906208	0.093791897

Table 5.1: Baseline Case: Pressure and viscous contribution to C_d (M=0.7)

Table 5.1 shows that as the AoA increases, pressure component of drag also increases. This is due to the separation at the upper surface. The viscous contribution(skin friction drag) of the drag reduces as the AoA increases. The diminishing contribution of the skin friction suggests that at higher AoA, the dynamics of flow is largely governed by inviscid effects.

	Lift Coefficient			Fractional Contribution	
AoA	Pressure	Viscous	Total	Pressure	Viscous
-2	0.008565	-5.81E-05	0.008507	1.006831	-0.00683
-1	0.171858	-9.27E-06	0.171848	1.000054	-5.4E-05
0	0.33426	4.24E-05	0.334302	0.999873	0.000127
1.1	0.513299	9.43E-05	0.513393	0.999816	0.000184
2	0.662579	0.000131	0.66271	0.999802	0.000198
3	0.834206	0.000162	0.834368	0.999805	0.000195
4	1.020038	0.000194	1.020232	0.99981	0.00019
5	1.193207	0.000236	1.193443	0.999802	0.000198

Table 5.2: Baseline Case: Pressure and viscous contribution to C_l (M=0.7)

Table 5.2 show that pressure component is playing a large role in the production of the lift.

5.2.2 Comparison of Baseline with VCCTEF

As we have seen earlier, trailing edge moves downwards as VCCTEF increases from 123, 222, 321, 33 & 6 respectively. The result of this should be an increase in drag, in this order, which is visible in the Fig. 5.29. At a given AoA, VCCTEF 6 is having the highest drag relative to other 5 configurations. The baseline is having the least drag compared to all VCCTEF configurations. VCCTEF 123 is showing the least drag at any AoA compared to other configurations. The plot of VCCTEF 321 and 33 almost coincide with each other.

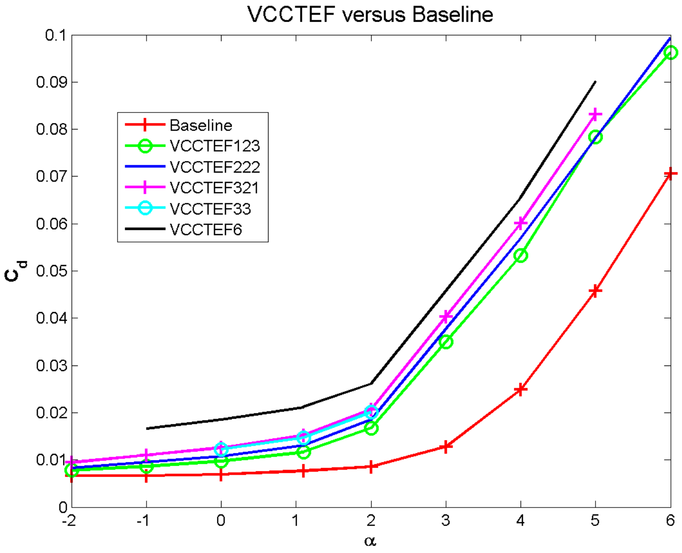

Figure 5.29: Variation of c_d with α

One of the thing to watch in these figures is the trend-line so that a designer can make an educated intuition about the computation of the 3-D geometry and hence the real life cases. Lift and drag coefficient values of the baseline are given in

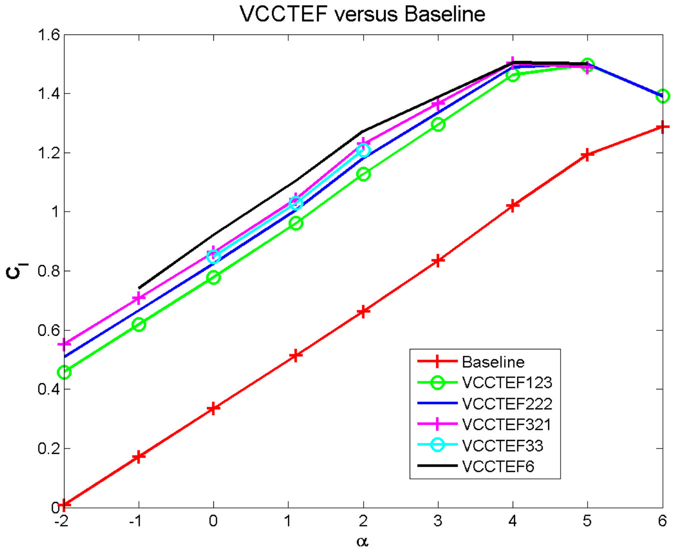

Figure 5.30: Variation c_l with α

the Table 5.1 and 5.2. The lift and drag coefficient values of the various VCCTEF configurations are given in the APPENDIX A. Fig.5.30 shows that all the configurations are increasing the lift coefficient with VCCTEF 6 giving the highest lift. One can see that the configuration also reduces the stall angle. VCCTEF 6 and VCCTEF 33 are having stall between 4° to 5° but certainly $< 5°$. VCCTEF 123 and VCCTEF 222 are stalling at 5°.Baseline will have stalling angle $\geq 6°$. Though these results are 2-D and not 3-D we are pretty sure to say that the VCCTEF configuration with better L/D ratio than baseline will stall earlier.

Fig.5.31 show the drag polar comparison of baseline and other VCCTEF configurations. The minimum drag for the baseline is at $C_l = 0$ and this gives our parasite drag or the zero lift drag ($\simeq 0.0066$). Almost all the VCCTEF configurations are having the same minimum drag point. Only VCCTEF 6 configuration tends to have a higher drag at minimum drag positions of other configurations.

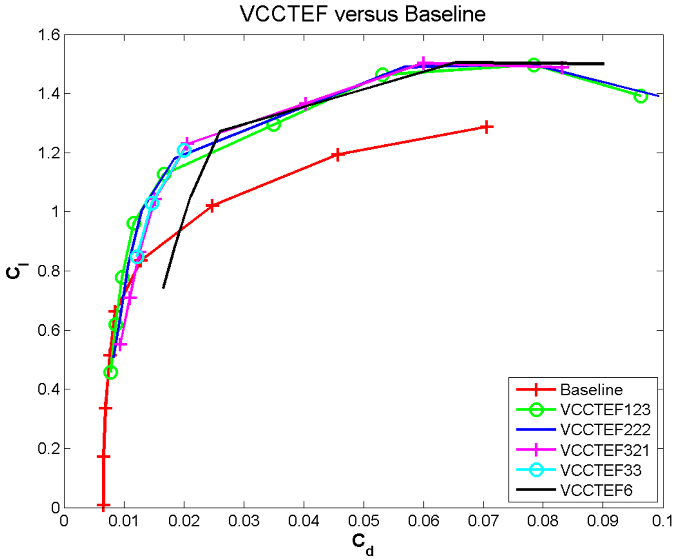

Figure 5.31: Baseline and VCCTEF comparison: drag polar

The highest C_l that any configuration can achieve compared to baseline is accompanied by higher drag.

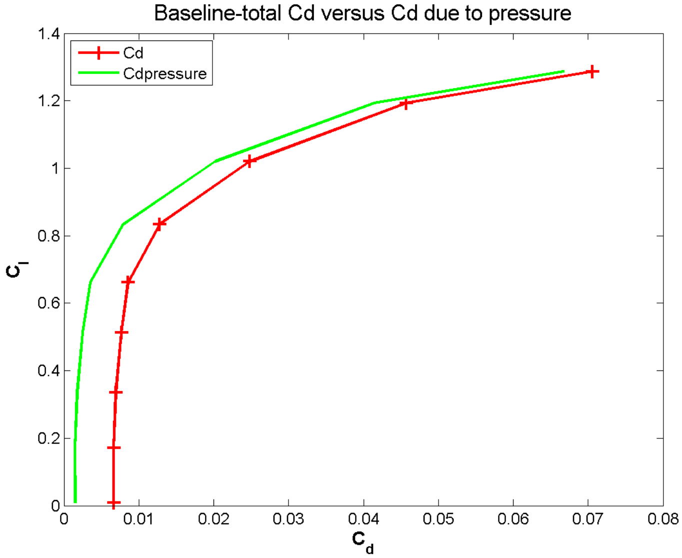

Figure 5.32: Baseline Case: comparison of overall drag and pressure drag

Fig.5.32 shows the difference in the overall drag and drag due to pressure. As the C_l value increases, both the curves tend to meet each other. The low C_l

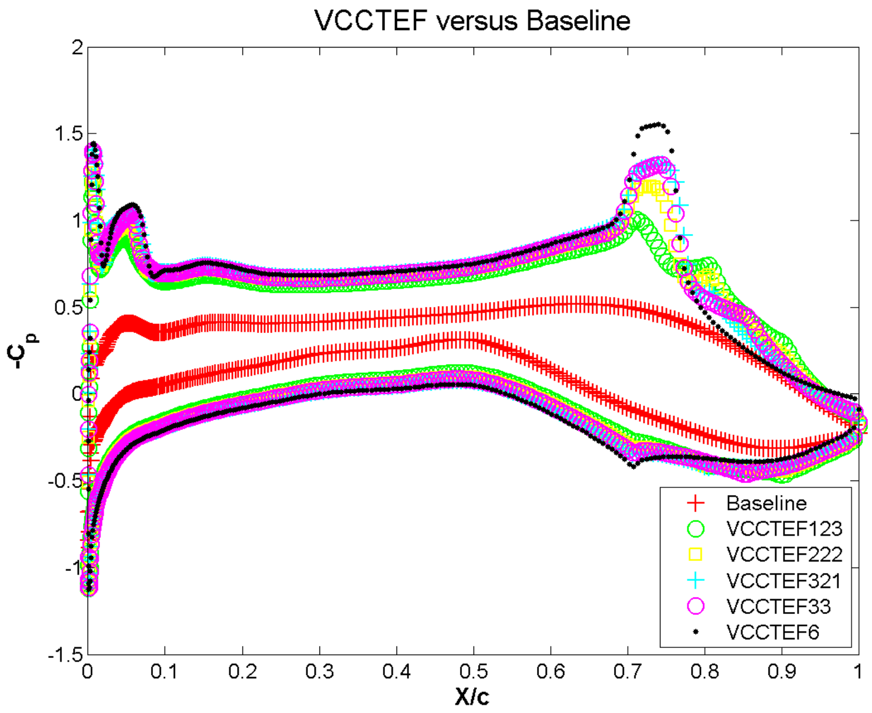

Figure 5.33: Cp comparison of baseline with VCCTEF configuration for 0^o AoA

values show the pre-stall region where a major component of the drag is due to the viscosity.At higher angle of attack, the effect of viscosity seems to be getting neglected by the turbulence model. This is highlighting the need for a better turbulence model.

Fig. 5.33 shows the comparison of C_p of baseline with VCCTEF configurations at AoA $= 0°$. As we move from Baseline to VCCTEF 6 the strength of shock formation(at x/c $\simeq 0.75$) is increasing, though baseline has a smooth compression. There is over expansion before the shock which can be seen by the decrease in pressure before the sudden increase in the pressure. This tendency of expansion along with the strength of shock reduces as we move from VCCTEF 6 to VCCTEF 123. The pressure and Mach contours at AoA $= 0°$ (see Fig. 5.23 and Fig. 5.24) shows no shock formation at x/c =0.75 whereas at x/c $\simeq$ 0.05 there is a very weak shock formation on the upper surface which is reflected in the Fig. 5.33 as well. The pressure and Mach contour for the various VCCTEF configurations are shown in the APPENDIX B.

Fig.5.34 shows that between $-2°$ to $1°$, the L/D value of all the VCCTEF configurations are better than the baseline configuration. From $\sim 1.5°$ no configuration is performing better than baseline.

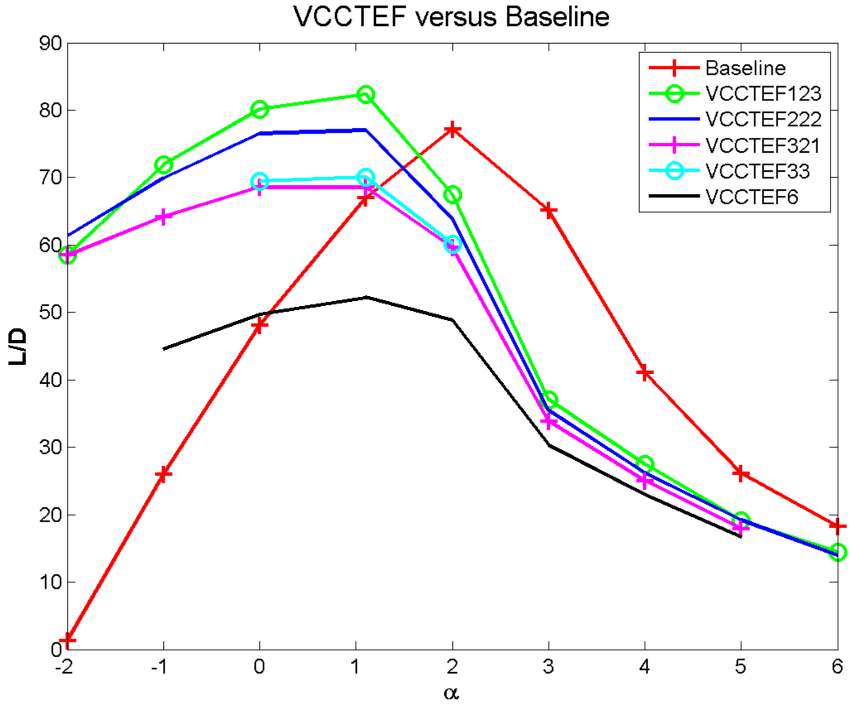

Figure 5.34: L/D variation with α

VCCTEF 123 is showing the best L/D ratio ($\simeq$ 80) at 1°. The baseline is showing better performance in terms of L/D ratio at $\alpha = 2°$ with L/D $\simeq$ 75. VCCTEF 222 shows the similar L/D but at $\alpha = 1°$. Fig 5.35 shows the L/D variation with C_l , where, it is revealed that beyond the $C_l \simeq 0.6$, VCCTEF 123 and

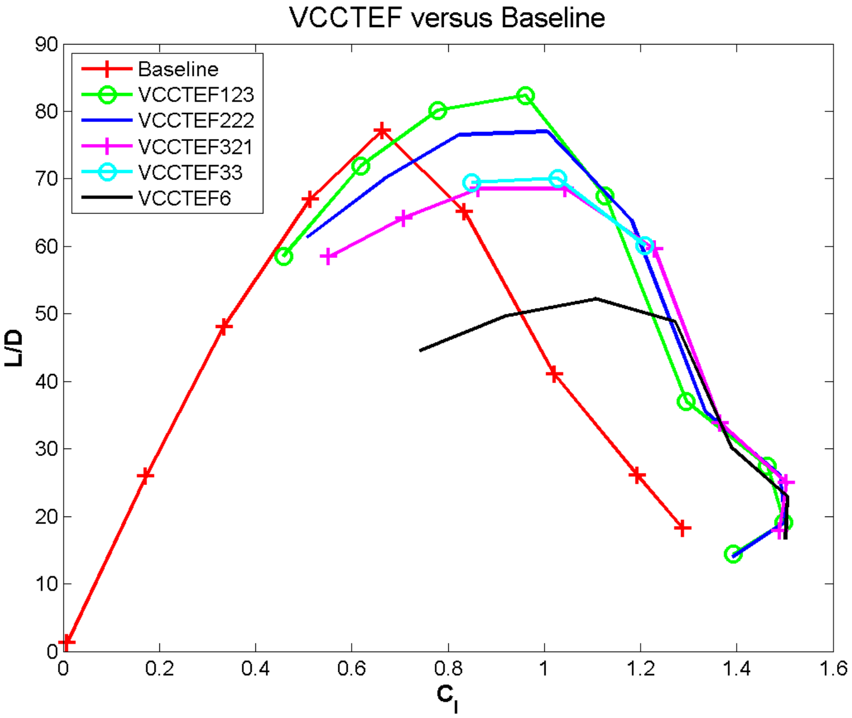

Figure 5.35: L/D variation with C_l

222 are performing better than baseline. Beyond $C_l \simeq 0.8$ all the configurations (except VCCTEF 6) are performing better than baseline. The best performance in the cruise is given by VCCTEF 123, with baseline and 222 following in respective orders. The baseline is showing the best performance at C_l=0.6 which is its design lift coefficient.

5.2.3 Comparison of computational lift increment with theoretical lift increment

A theoretical formulation for incremental lift coefficient was discussed in Section 3.7. Fig. 5.36 gives the theoretical lift increment which is compared with computational lift increment. The computed lift increment is the average of the values at 0° and 1° thus validating the lift increment before the stall when the flow is not separated. The maximum difference is $\simeq 3.3\%$.

From the drag coefficient values of the various VCCTEF configurations (given in the APPENDIX A) it is seen that similar to baseline, as the AoA increases pressure component of drag increases. The viscous contribution (skin friction drag) of the drag reduces as the AoA increases. The diminishing contribution of the skin friction suggest that at higher AoA, dynamics of flow are coming largely by inviscid effects. There is a negligible amount of viscous contribution in the production of lift.

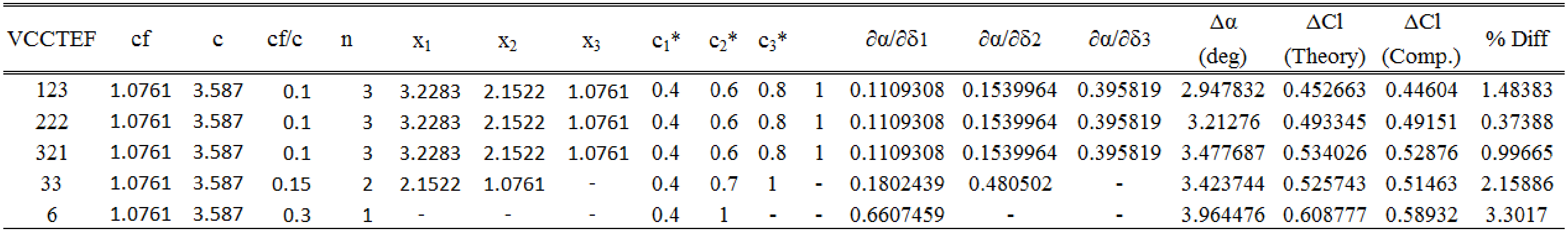

VCCTEF	cf	c	cf/c	n	x_1	x_2	x_3	c_1*	c_2*	c_3*		∂α/∂δ1	∂α/∂δ2	∂α/∂δ3	Δα (deg)	ΔCl (Theory)	ΔCl (Comp.)	% Diff
123	1.0761	3.587	0.1	3	3.2283	2.1522	1.0761	0.4	0.6	0.8	1	0.1109308	0.1539964	0.395819	2.947832	0.452663	0.44604	1.48383
222	1.0761	3.587	0.1	3	3.2283	2.1522	1.0761	0.4	0.6	0.8	1	0.1109308	0.1539964	0.395819	3.21276	0.493345	0.49151	0.37388
321	1.0761	3.587	0.1	3	3.2283	2.1522	1.0761	0.4	0.6	0.8	1	0.1109308	0.1539964	0.395819	3.477687	0.534026	0.52876	0.99665
33	1.0761	3.587	0.15	2	2.1522	1.0761	-	0.4	0.7	1	-	0.1802439	0.480502	-	3.423744	0.525743	0.51463	2.15886
6	1.0761	3.587	0.3	1	-	-	-	0.4	1	-	-	0.6607459	-	-	3.964476	0.608777	0.58932	3.3017

Figure 5.36: Theoretical and computational lift coefficient c_l comparison (SA model)

5.3 Conclusion

For fully turbulent simulations, SA model validated the Ladson (tripped) data at low AoA. Hence it was chosen for the further simulations. During the cruise, compared to the Baseline, VCCTEF 123 showed higher L/D ratio ($\simeq 80$) at $C_l = 1.1$. VCCTEF 222 showed relatively similar L/D ratio as baseline, at its apex value (at $C_l \simeq 0.7$). The computed lift increment was compared with the theoretical lift increment and was found in good agreement.

CHAPTER 6

RESULTS OF TRANSITION SIMULATION ON BASELINE & VCCTEF

In Chapter 5, NACA 0012 Transition k-kl-omega results were close to Abbot & Von Doenhoff (untripped) data. If the airfoil is not tripped than flow over it will be laminar over certain portion and will have transition to turbulent flow. Thus, Transition k-kl-omega predicted the results of NACA 0012 when it was having laminar portion over its surface. The simulations were performed at Mach number = 0.15 and Reynolds number = 6 million. In the present chapter, validation of the Transition k-kl-omega model was done by using two airfoils. One, NACA 63209 (at very high Reynolds number, 20 million) and another was RAE 2822 airfoil (high Mach number, 0.676).

6.1 Validation using NACA 63209

The experimental results of NACA 63209 at Reynolds number 20 million were shown in Section 4.3.2. The numerical simulations were performed at 2 different AoA (0° and 5°) using both SA and Transition k-kl-omega model. Fig. 6.1 show the variation of C_l with respect to AoA, at M =0.3 and Reynolds number = 20 million. The result shows that both SA and Transition model predicted C_l very well. The slope of the curve $C_{l\alpha}$ is also in good agreement.

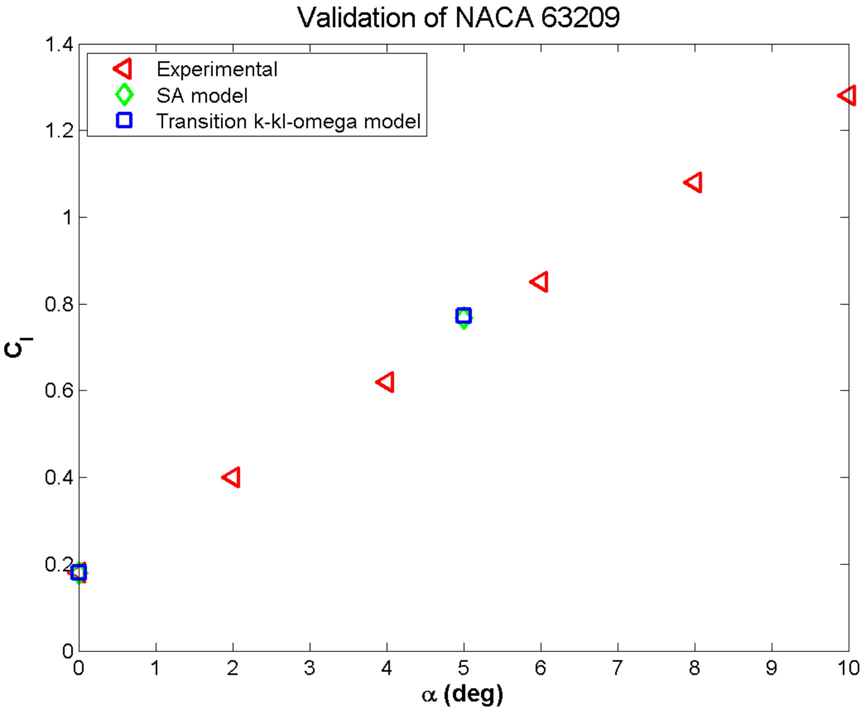

Figure 6.1: C_l vs. AoA (α) (NACA 63209)

During the cruise airfoils are not deflected at higher AoA, the range of AoA we are interested in, is up to 4° maximum. Fig. 6.2 show the variation of C_d with respect to C_l. Until 5°, Transition k-kl-omega model is predicting drag quite well. Compared to SA model, it predicted a slightly lesser drag both at 0° and

5°, which is closer to the experimental value.

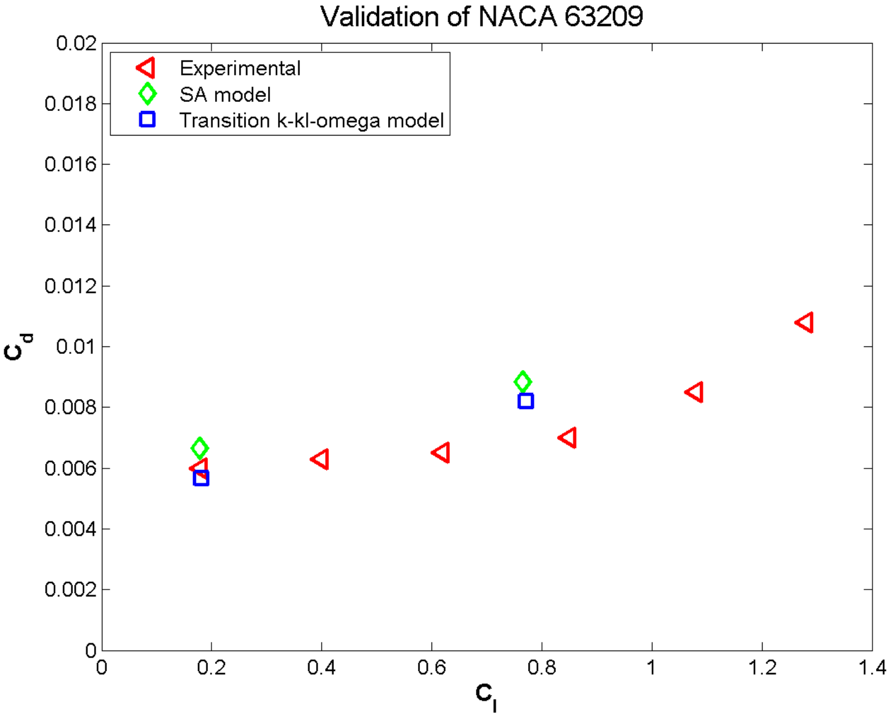

Figure 6.2: C_d vs. C_l (NACA 63209)

6.2 Validation using RAE 2822 airfoil

In the experiments, the airfoil is tripped to make the flow turbulent. Depending on the position of tripping, airfoil may or may not have a considerable region of a laminar portion over its surface. If airfoil is to be made fully turbulent then it is tripped at the leading edge. Results having laminar portion over the surface of airfoil were selected for validation. Two cases were selected, each having a laminar portion up to 10% of the airfoil chord. The simulations were performed at M = 0.676 and Reynolds number 5.7 million using Transition k-kl-omega model. Figure 6.3 shows the C_n vs. α variation. C_n can be approximated as C_l for low AoA, based on the equation given below,

$$C_n = C_l\ cos(\alpha) + C_d\ sin(\alpha) \tag{6.1}$$

When α is small, $sin(\alpha) \simeq 0$, and $cos(\alpha) \simeq 1$. Thus, $C_n = C_l$. Fig. 6.3 is showing an almost constant offset at both the angles. The present study is focused towards comparing and finding a better VCCTEF configuration. The deflection in camber, causes a change in lift curve slope $C_{l\alpha}$ because of the increased circulation, based on Kutta-Joukowski theorem. Nguyen et.al [48] has suggested that uncertainty in deflection of VCCTEF can cause a constant offset in the coefficient of lift. Rather than the magnitude of C_l, its slope ($C_{l\alpha}$) is a better indicator for lift comparison.

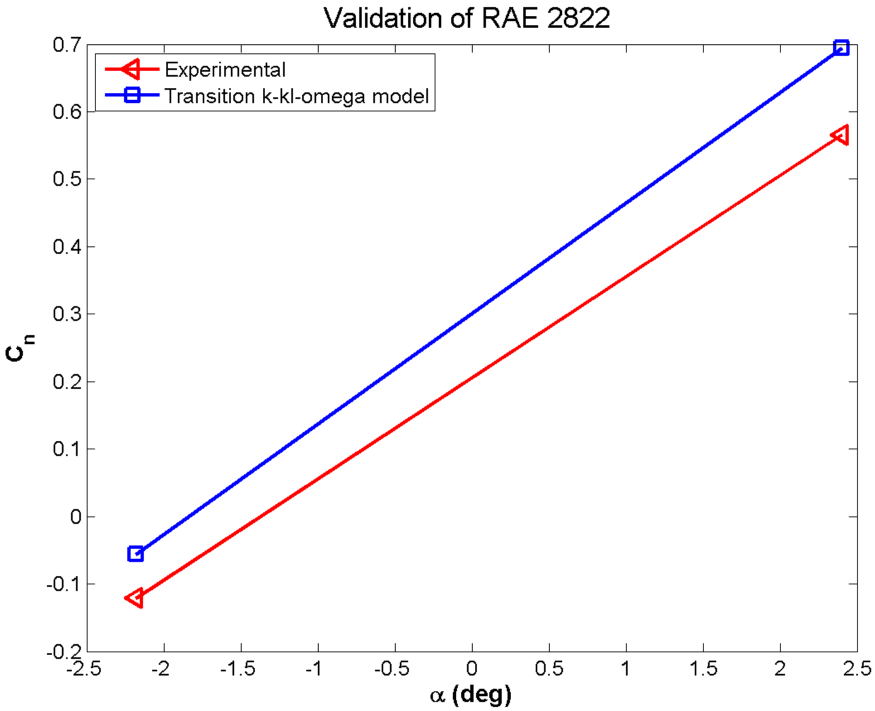

Figure 6.3: C_n vs. α variation, RAE 2822 airfoil

Fig. 6.3 shows that slope of experimental and simulation results are almost similar. Fig. 6.4 shows the comparison of C_d with respect to AoA (α). At both the AoA, the computed drag is similar to the experimental drag value. Fig. 6.5 shows the comparison of pressure coefficient for $\alpha = 2.4°$. Computed pressure coefficient matches well with the experimental values, with an exception on the upper surface until 15% of chord, where C_p is over predicted. Fig. 6.6 shows that experimental and computed C_p matches well with each other at $\alpha = -2.18°$.

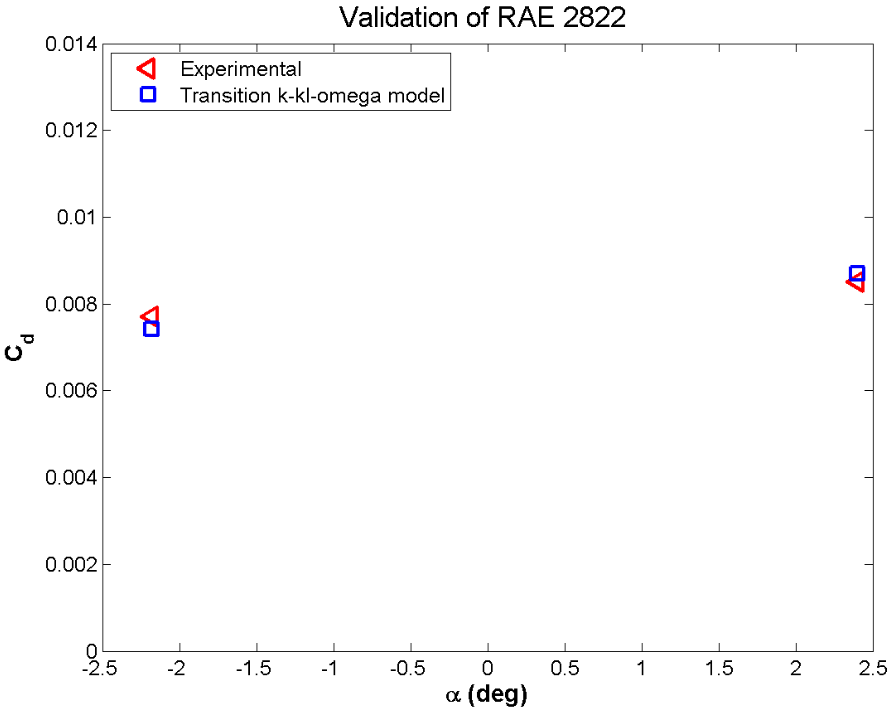

Figure 6.4: C_d vs. α variation, RAE 2822 airfoil

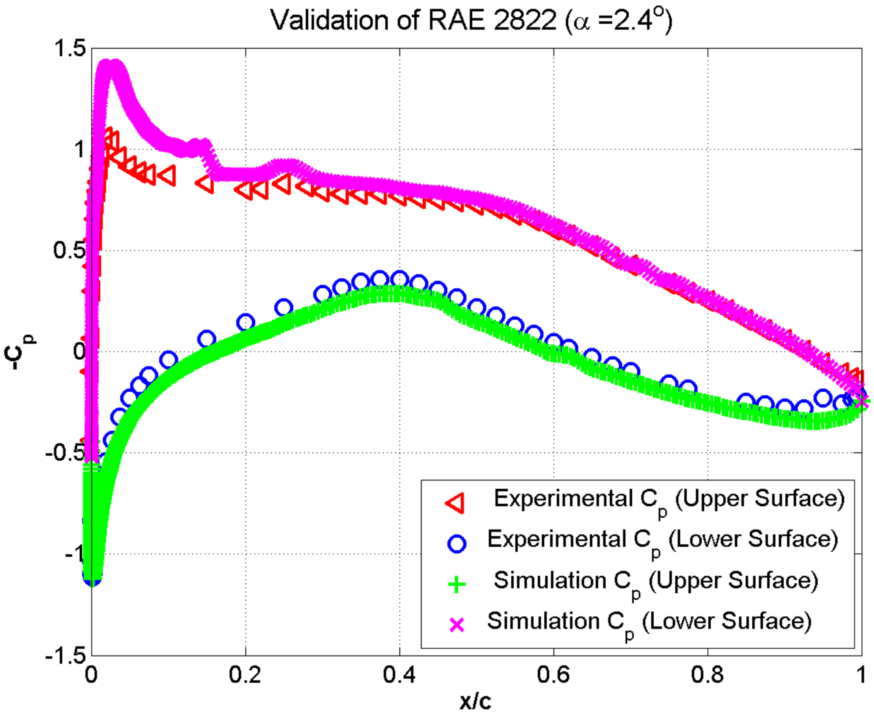

Figure 6.5: C_p vs. x/c, α = 2.4°, RAE 2822 airfoil

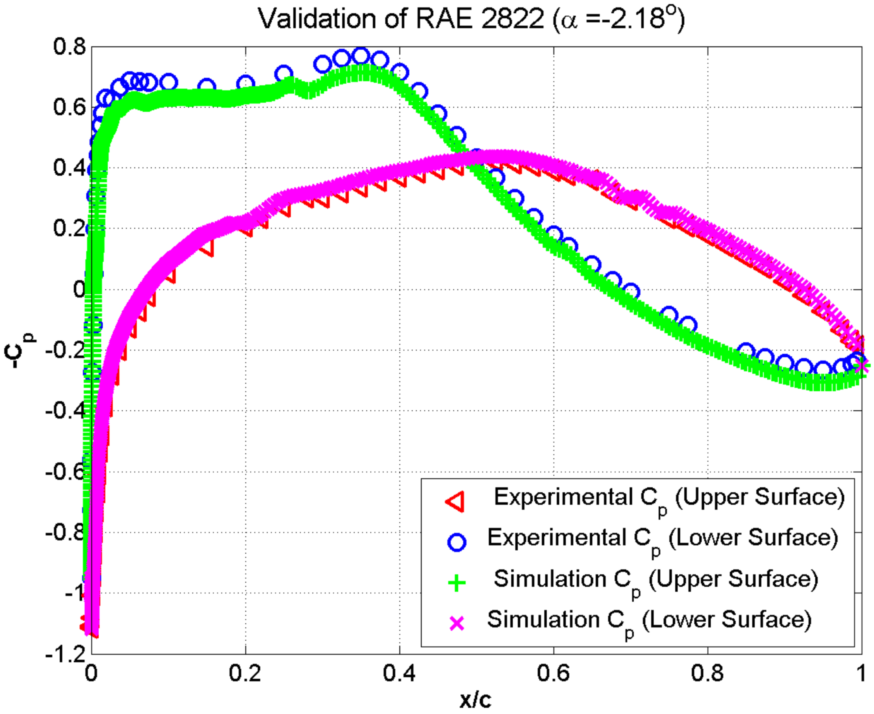

Figure 6.6: C_p vs. x/c, α = -2.18°, RAE 2822 airfoil

6.3 Outboard Airfoil or Kink (Transition k-kl-omega Model)

This section presents the results of Transition k-kl-omega model simulations on the Baseline and various VCCTEF configurations.

6.3.1 Baseline

In this subsection, the various simulations which were run on the baseline using Transition model are discussed.

Grid Dependence

The three grids that were studied using the Transition model at AoA = 0° , 2° and 4° are given below,

1. Grid I: 700×150 (500 pts. around airfoil), 105000 cells
2. Grid II: 1122×200 (922 pts. around airfoil),224400 cells
3. Grid III: 1422×250 (922 pts. around airfoil), 355500 cells

Grid I is similar to the grid which used SA model for the simulations shown in Chapter 5. Grid II is the validation grid used on NACA 63209 and RAE 2822 airfoil. Grid III is made by increasing number of cells. The simulations were performed at M = 0.7 and Reynolds number = 21.6 million. Fig 6.7 shows the variation of C_l with respect to the grid sizes. It is seen that there is no much change in the C_l value for the various grids. C_l increases with AoA.

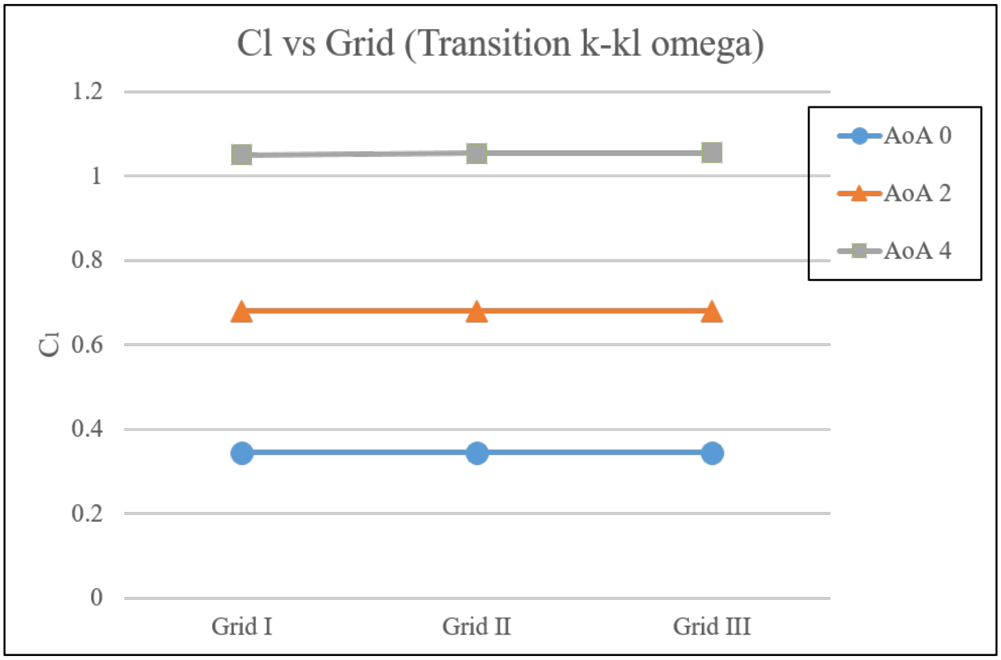

Figure 6.7: C_l vs. Grid (M=0.7, Re = 21.6 million)

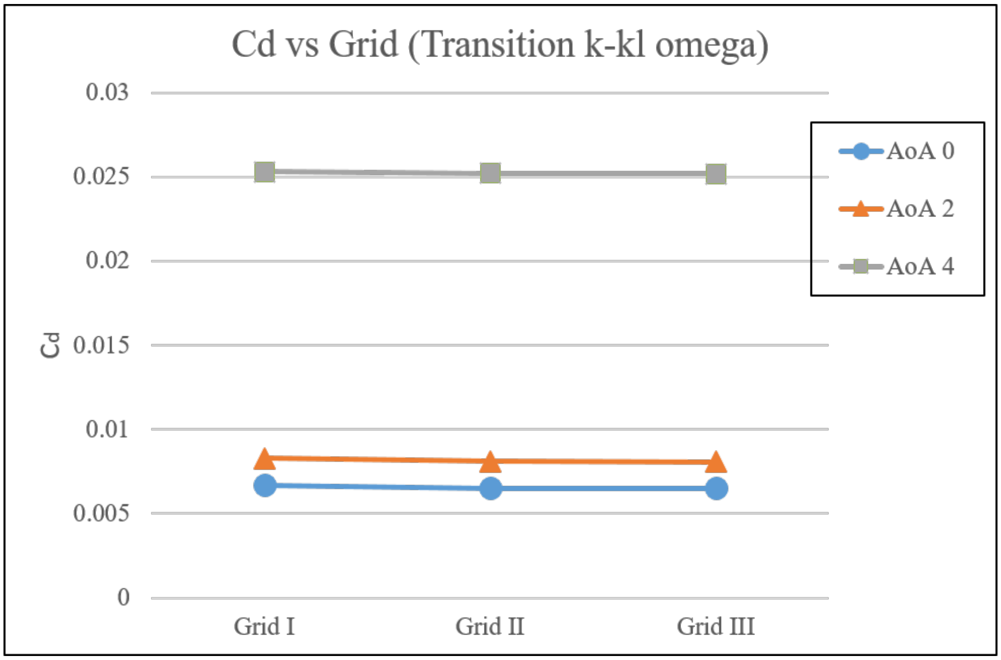

Figure 6.8: C_d vs. Grid (M=0.7, Re = 21.6 million)

Fig. 6.8 shows a slight variation in the C_d value between Grid II and Grid I. Grid II is having a slightly lower C_d value. There is no change in Grid II and III.

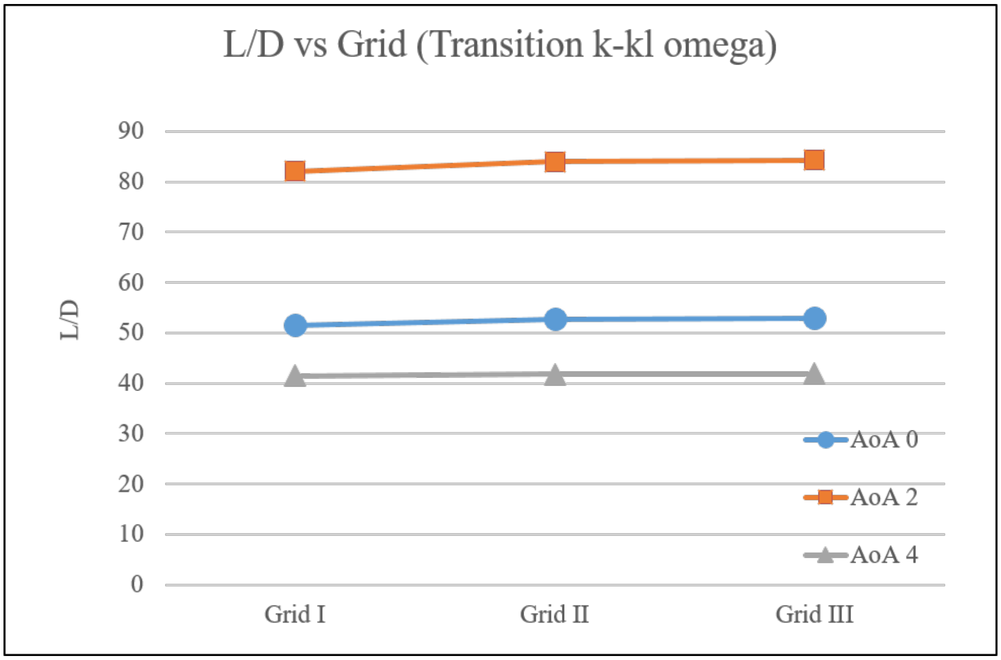

Figure 6.9: L/D vs. Grid (M=0.7, Re = 21.6 million)

Fig. 6.9 shows a slight higher L/D ratio in Grid II relative to Grid I. The L/D ratio for Grid I at AoA = 2°, is 82 whereas for Grid II and III it is 84. The comparison of pressure coefficient plots for various grids is shown in Fig. 6.10. All the grids overlap each other suggesting no change in C_p at various AoA.

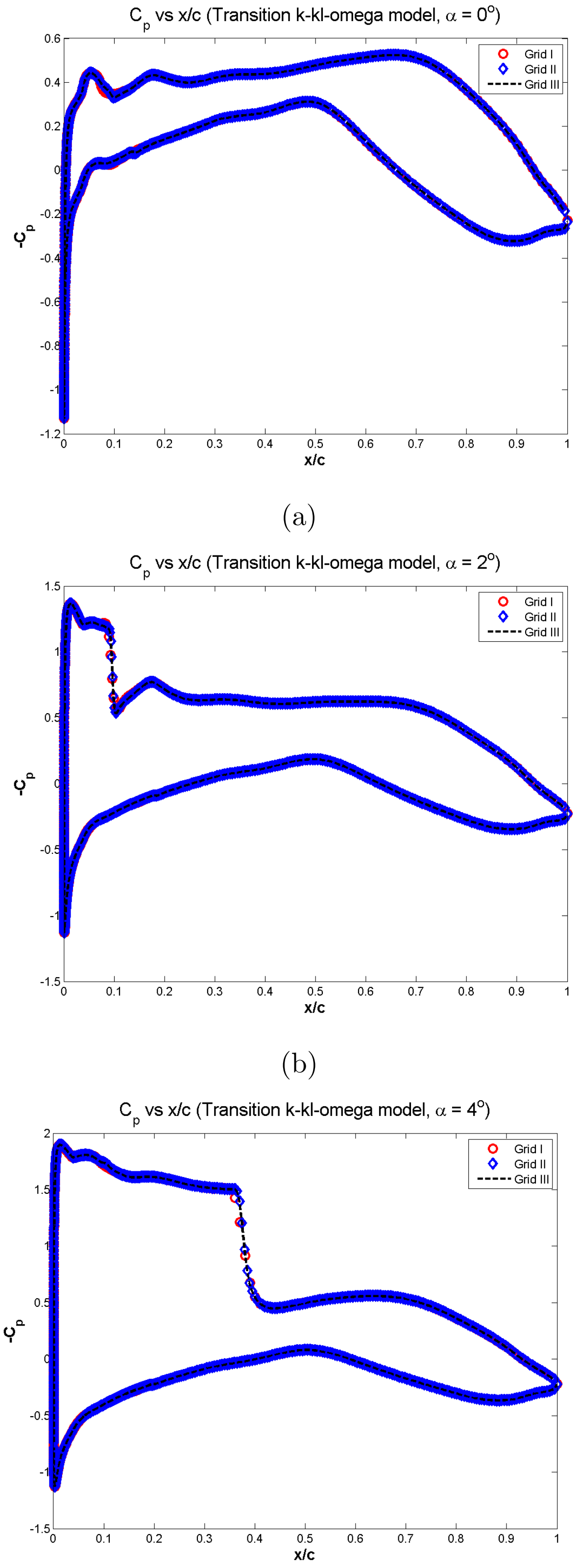

(a)

(b)

(c)

Figure 6.10: Baseline results of C_p vs. x/c using Transition k-kl-omega (a) α= 0° (b) α= 2° (c) α= 4°

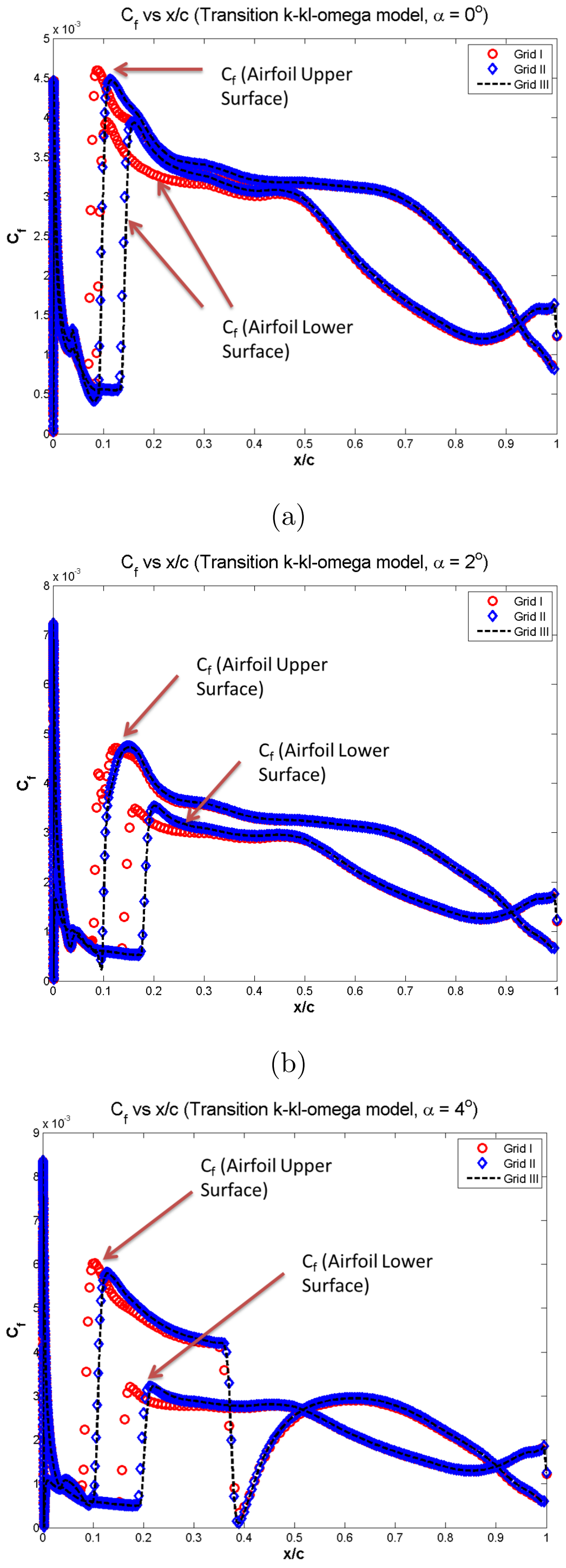

(a)

(b)

(c)

Figure 6.11: Baseline results of C_f vs. x/c using Transition k-kl-omega (a) α= 0° (b) α= 2° (c) α= 4°

Fig. 6.11 shows the variation of the skin friction coefficient (C_f) with x/c for the various AoA. Fig. 6.11(a) shows an increase in C_f at x/c = 0.09 (9% of airfoil chord length) for all the three grids. This corresponds to the airfoil upper surface transition point, because as the flow changes from laminar to turbulent, the skin friction coefficient increases. For the Grid I, the lower surface transition point is at x/c = 0.09, whereas, for Grid II and III the transition point is at x/c = 0.13 (13% of the chord length).Hence, Grid II and III agree with each other. The variation in the transition location of the upper and the lower surface for other angle of attacks are shown in Table 6.1 which also suggests that for Grid II and III, the location of transition point is on the same x/c location.

Table 6.1: Transition location for Grid I,II and III at $\alpha = 0°$, $2°$ and $4°$

AoA (α)	Grid #	Transition location (Airfoil Upper surface)	Transition location (Airfoil Lower surface)
0	Grid I	9%	9%
	Grid II	9%	13%
	Grid III	9%	13%
2	Grid I	9%	14%
	Grid II	10%	18%
	Grid III	10%	18%
4	Grid I	9%	15%
	Grid II	10%	20%
	Grid III	10%	20%

Based on the results for various grids. Grid II and III predicted similar results. Grid II will be used for the various VCCTEF configurations. Fig. 6.12 shows the variation of Mach number with respect to x/c. The plots are derived from the C_p and Mach number relation, which depicts the direct relation between them.

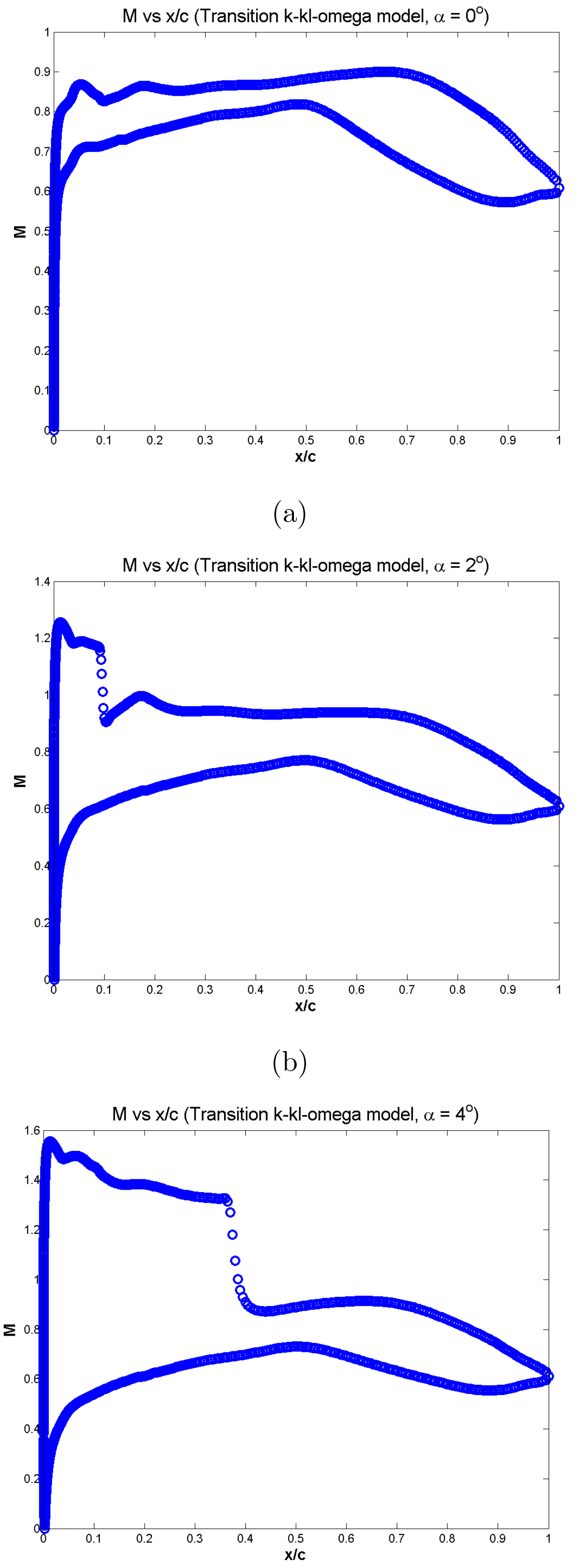

(a)

(b)

(c)

Figure 6.12: Baseline results of M vs. x/c using Transition k-kl-omega (a) $\alpha = 0°$ (b) $\alpha = 2°$ (c) $\alpha = 4°$

The values of C_l and C_d for Baseline using Transition model are determined and summarized along with their pressure and viscous components in Table 6.2 and Table 6.3

Table 6.2: Baseline Case (Transition k-kl-omega): Pressure and viscous contribution to C_d (M=0.7)

	Drag Coefficient			Fractional Contribution	
AOA	Pressure	Viscous	Total	Pressure	Viscous
-2	0.001208	0.004887	0.006095	0.198178	0.801822
0	0.001598	0.005095	0.006693	0.238717	0.761283
1.1	0.002232	0.004925	0.007158	0.311889	0.688111
2	0.003378	0.00491	0.008288	0.407558	0.592442
4	0.020607	0.004692	0.025299	0.814535	0.185465

Similar to the SA model results, Table 6.2 shows that as the AoA increases, pressure component of drag also increases and the viscous contribution(skin friction drag) of the drag reduces. The diminishing contribution of the skin friction suggests that at higher AoA, the dynamics of flow are largely governed by inviscid effects. At AoA = 4°, the pressure component increases rapidly due to shock formation.

Table 6.3: Baseline Case (Transition k-kl-omega): Pressure and viscous contribution to C_l (M=0.7)

	Lift Coefficient			Fractional Contribution	
AOA	Pressure	Viscous	Total	Pressure	Viscous
-2	0.015631	-6.5E-05	0.015566	1.004171	-0.00417
0	0.34518	2.87E-05	0.345208	0.999917	8.3E-05
1.1	0.52679	7.95E-05	0.52687	0.999849	0.000151
2	0.680276	9.51E-05	0.680371	0.99986	0.00014
4	1.050664	0.000142	1.050806	0.999865	0.000135

Table 6.3 shows that similar to SA model, pressure component is playing a large role in the production of the lift and the viscous contribution in the lift is negligible.

6.3.2 Comparison of Baseline and VCCTEF (Transition k-kl-omega model)

Simulations for VCCTEF configurations were performed using the Grid II (1122 × 200 (922 points around airfoil)). This is the same mesh which was used for validation of Transition k-kl-omega model. Simulations were performed for various AoA, ranging from -2° to 4°. There are two reasons for selecting this range. Firstly, during the cruise, we do not use very high AoA. Secondly, the W-ATRA aircraft has twist distribution for outboard airfoil from -2° to 1.1°. The VCCTEF 6 configuration at 2° shows a huge deviation from its trend line due to separation. So the results of VCCTEF 6 are presented until 1.1°.

The trend of C_d vs x/c plots are similar to that of SA model. The deflection of trailing edge for VCCTEF increases in the order 123, 222, 321, 33 & 6 respectively. At any given AoA, VCCTEF 6 is having the highest drag and baseline is having the least drag. VCCTEF 123 shows the least drag among all the VCCTEF configurations. Compared to baseline, all the VCCTEF configurations showed increase in lift as it is visible in the Fig. 6.14.The plots of VCCTEF 222 and 321 almost coincide with each other. There is no stall seen for any of the configurations.

Fig. 6.15 shows the drag polar comparison of baseline and other VCCTEF

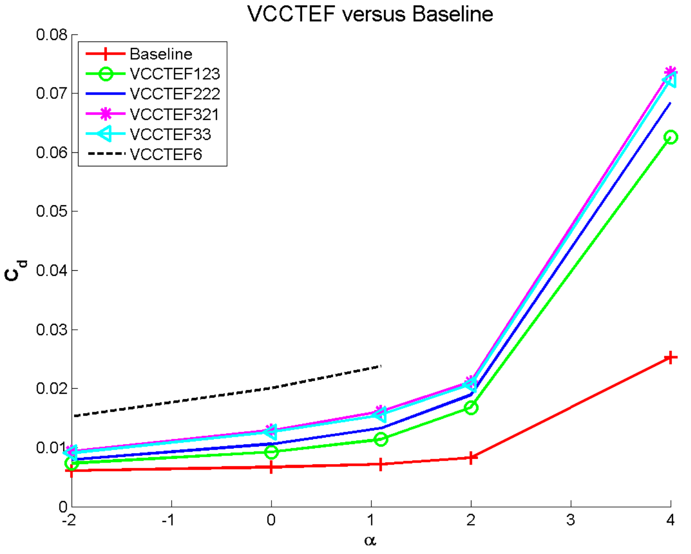

Figure 6.13: Variation c_d with α (Transition model)

configurations. Baseline configuration's parasite drag or the zero lift drag is $\simeq$ 0.0061. The parasite drag for fully turbulent simulation was 0.0066. VCCTEF 123 shows minimum drag compared to all the VCCTEF configurations from C_l 0.5 to 1. Until $C_l = 1.3$, the increment in drag is gradual. After that, there is a sudden increase in drag coefficient. This increment in drag is due to increased pressure drag. Fig. 6.16 show that as C_l increases, the pressure component of the drag also increases. The contribution of viscous component of drag reduces with increase in C_l.

Fig. 6.17 shows the comparison of C_p of baseline with VCCTEF configurations at AoA = 0°. The strong shock at x/c = 0.75, can be seen in the C_p corresponding to VCCTEF 6 on the upper surface. Neglecting the initial jumps on the upper surface, all the VCCTEF configurations follow HLFC design criteria by having a steep pressure gradient on the upper surface.

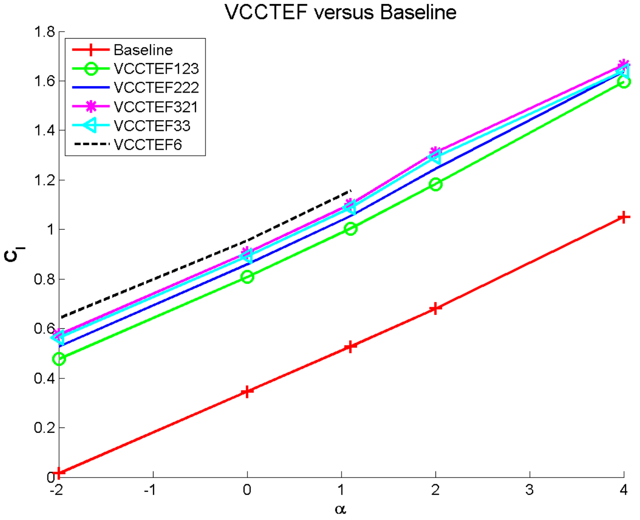

Figure 6.14: Variation c_l with α (Transition model)

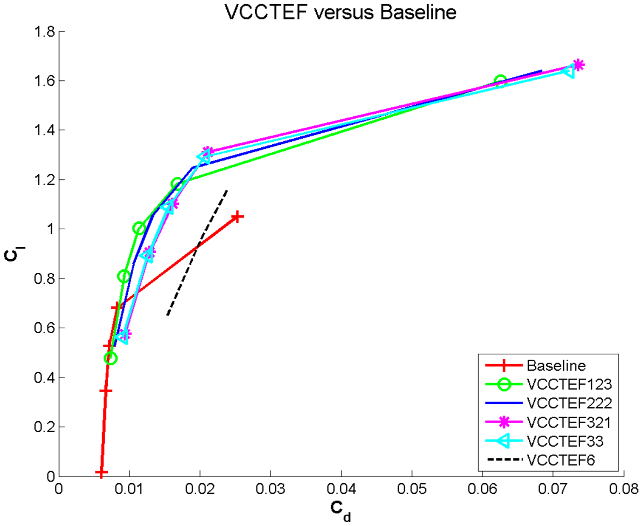

Figure 6.15: Baseline and VCCTEF comparison: drag polar (Transition model)

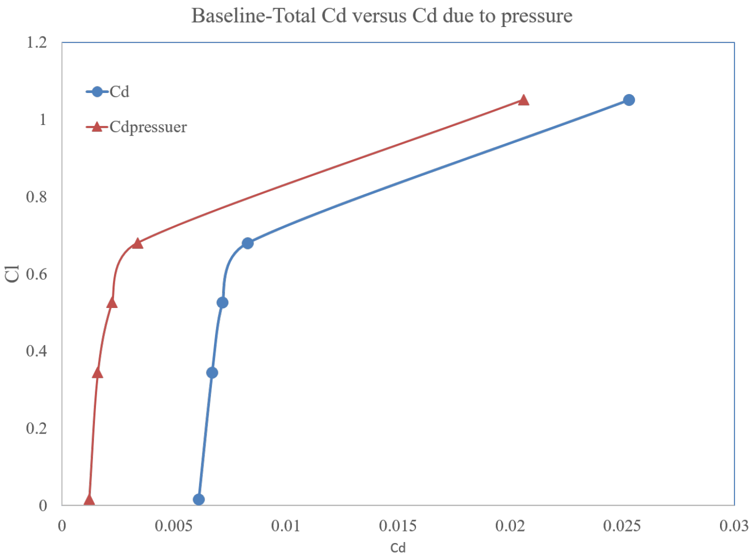

Figure 6.16: Baseline Case: Comparison of overall drag and pressure drag (Transition model)

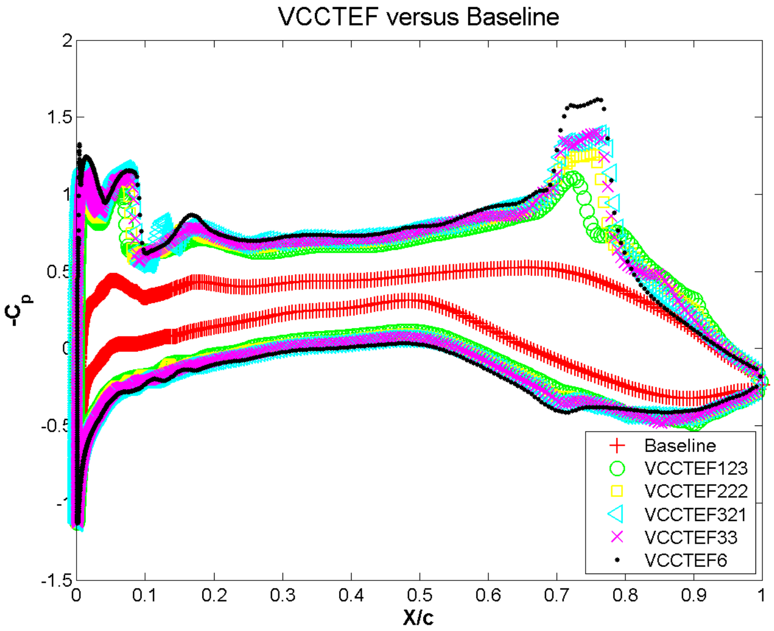

Figure 6.17: C_p vs. x/c comparison of baseline with VCCTEF configuration for 0^o AoA (Transition model)

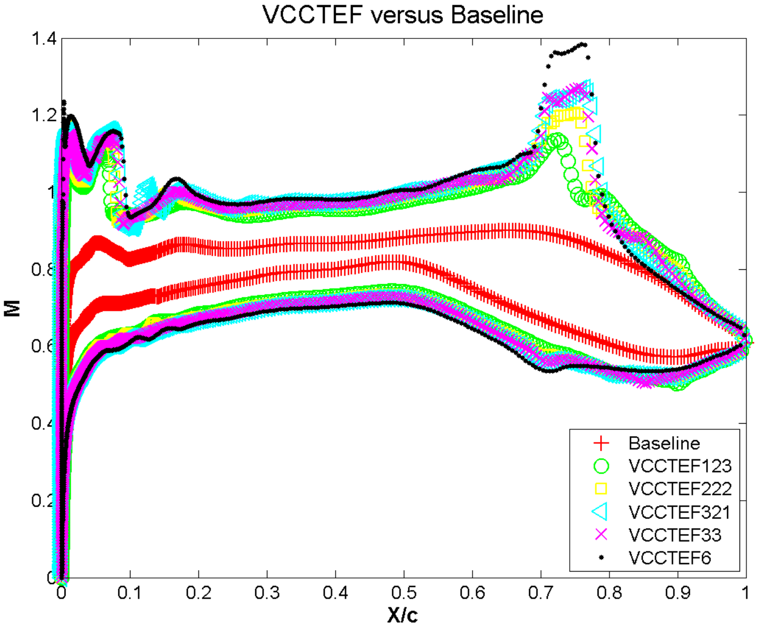

Figure 6.18: M vs. x/c comparison of baseline with VCCTEF configuration for 0^o AoA (Transition model)

Fig. 6.18 shows the variation of Mach number with respect to x/c. A direct correspondence between the C_p plot and Mach number plot can be seen. The plot of Mach number is obtained from the Eq. 6.2.

$$M = \sqrt{\frac{2}{\gamma - 1}\left[\left(1 + \frac{\gamma - 1}{2}M_\infty^2\right)\left(1 + \frac{\gamma}{2}M_\infty^2 C_p\right)^{-\frac{\gamma-1}{\gamma}} - 1\right]} \tag{6.2}$$

Fig.6.19 shows the comparison of L/D ratio with respect to AoA. At $\alpha < 1°$, all the VCCTEF configurations are performing better than baseline. VCCTEF 123 is showing the best L/D ratio of 88 at 1°. Compared to fully turbulent SA model (L/D =80) there is 10 % increment. This is because of the reduction in viscous drag component due to consideration of laminar portion.

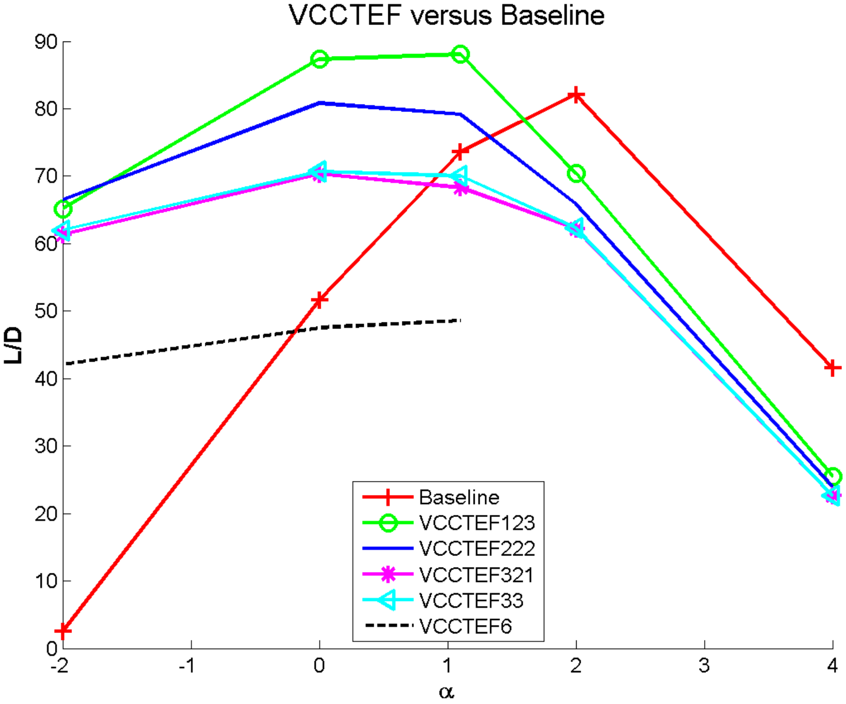

Figure 6.19: L/D variation with α (Transition model)

Fig. 6.20 shows the variation of L/D ratio with C_l. VCCTEF 123 shows the best L/D for C_l between a range of 0.8 to 1.1 .

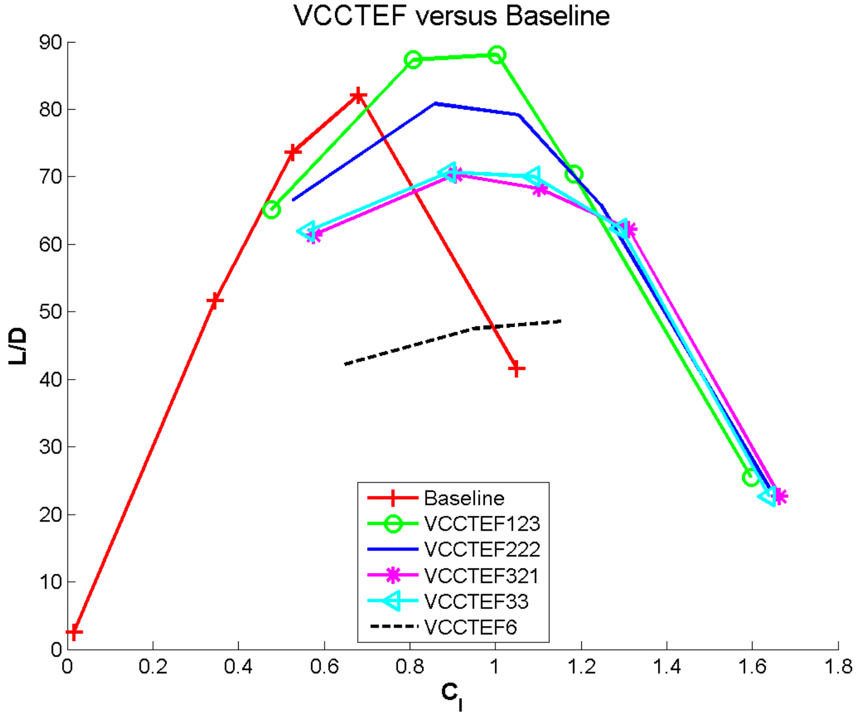

Figure 6.20: L/D variation with C_l(Transition model)

6.3.3 Comparison of computational lift increment with theoretical lift increment

A comparison of theoretical and computed lift increment is shown in the Fig. 6.21. The maximum error is 0.0426 corresponding to VCCTEF 33. The computed lift increment is obtained using the C_l values of 0^0 and 1^0.

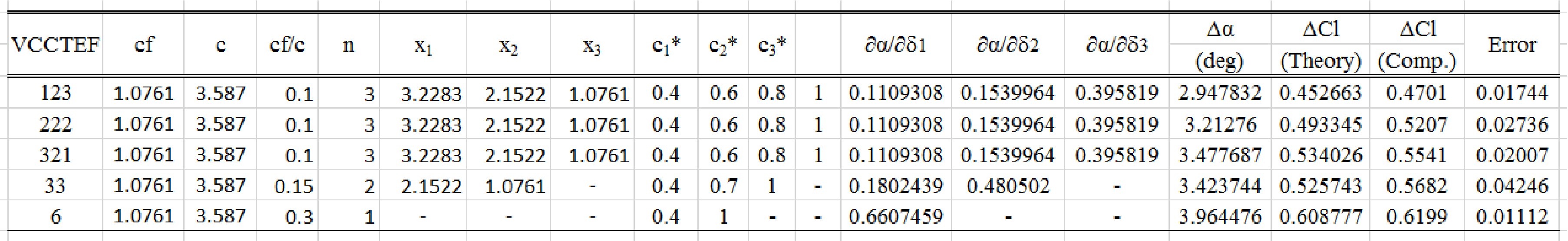

VCCTEF	cf	c	cf/c	n	x_1	x_2	x_3	c_1*	c_2*	c_3*		∂α/∂δ1	∂α/∂δ2	∂α/∂δ3	Δα (deg)	ΔCl (Theory)	ΔCl (Comp.)	Error
123	1.0761	3.587	0.1	3	3.2283	2.1522	1.0761	0.4	0.6	0.8	1	0.1109308	0.1539964	0.395819	2.947832	0.452663	0.4701	0.01744
222	1.0761	3.587	0.1	3	3.2283	2.1522	1.0761	0.4	0.6	0.8	1	0.1109308	0.1539964	0.395819	3.21276	0.493345	0.5207	0.02736
321	1.0761	3.587	0.1	3	3.2283	2.1522	1.0761	0.4	0.6	0.8	1	0.1109308	0.1539964	0.395819	3.477687	0.534026	0.5541	0.02007
33	1.0761	3.587	0.15	2	2.1522	1.0761	-	0.4	0.7	1	-	0.1802439	0.480502	-	3.423744	0.525743	0.5682	0.04246
6	1.0761	3.587	0.3	1	-	-	-	0.4	1	-	-	0.6607459	-	-	3.964476	0.608777	0.6199	0.01112

Figure 6.21: Theoretical and computational lift coefficient C_l comparison (Transition model)

CHAPTER 7

CONCLUSIONS AND RECOMMENDATIONS

7.1 Conclusion

This study deals with the new concept called Variable Camber Continuous Trailing Edge Flap (VCCTEF) system developed by NASA [5], as conventional flap and slats are not efficient with aeroelastic wing shaping control for drag minimization. The airfoil used for the present study was an outboard airfoil of Wing of Advanced Technology Regional Aircraft (W-ATRA) [1], which extends from wing break station to the tip. The airfoil has a chord length of 3587 *mm* (141.2205 *inches*). VCCTEF overall flap chord is 30% of airfoil chord, measured from the first hinge line. The flow solver used to conduct this study is non- commercial ANSYS FLUENT software. The simulation on the baseline and various VCCTEF configurations were performed using two models i.e. Fully turbulent SA model and Transition k-kl-omega model. The results identified the most aerodynamic efficient VCCTEF configuration amongst the various configurations. VCCTEF 123 showed the best L/D ratio of $\simeq 80$ at 1° using SA model. Transition model predicted an L/D ratio of $\simeq 88$, which shows a 10 % increment in the aerodynamic efficiency. The improvement in the ratio is coming from the laminar region over the airfoil. Both the models predicted an increase in the drag as the AoA increases, because of the increment in the pressure component of drag. Compared to baseline, VCCTEF 123 has 7.2 % increment in L/D ratio using Transition k-kl-omega model and 6.3 % increment in L/D ratio using SA model. Two-Dimensional (2-D) CFD results have the tendency to produce weak shocks and over-expansions before the shock formation on the surface of the airfoil. These may be absent in the experimental work. 2-D flow has sharp gradients which can be relieved in Three-dimensional (3-D) flow by variation in pressure gradient due to cross-flow, which is called as 3-D relief effect. Upon neglecting the weak shocks near the leading edge all the configurations (including baseline) are showing favorable pressure gradient up to 65% of chord at AoA $=0°$ and all the VCCTEF configurations showed the shock formation at hinge positions with VCCTEF 6 having a strong shock. VCCTEF 123, which is parabolic arc angle configuration, showed better performance than all configurations.The computed incremental lift coefficient and theoretical lift coefficients are in good agreement using both SA and Transition k-kl-omega model.

7.2 Recommendations & Future Work

To access the full potential of VCCTEF following points must be considered.

- A study of the 3-D wing can give us more insight on the performance of the ATRA wing with VCCTEF configuration.
- Using VCCTEF 123 configuration on 3-D wing, an aeroelastic analysis can be performed.
- Effect of elastomer must be studied upon the 3-D wing.
- A study to estimate worst hinge moments cases in cruise conditions with maneuver loads, must be performed.

REFERENCES

[1] Prasetyo Edi and J. P. Fielding, "Civil-Transport Wing Design Concept Exploiting New Technologies," *Journal of Aircraft*, vol. 43, no. 4, pp. 932–940, Jul. 2006. [Online]. Available: http://arc.aiaa.org/doi/abs/10.2514/1.15556

[2] Boeing Commmercial Airline Co., "Hybrid Laminar FlowControl Study Final Technical Report," *NASA CR 165930,1982*.

[3] E. Greff, "Aerodynamic Design and Technology Concepts for a New Ultra-High Capacity Aircraft," *International Council of the Aeronautical Sciences, Paper 96-4.6.3,1996*.

[4] U. K. Kaul and N. T. Nguyen, "Drag Optimization Study of Variable Camber Continuous Trailing Edge Flap (VCCTEF) Using OVERFLOW," *32nd AIAA Applied Aerodynamics Conference , 16-20 June 2014, Atlanta, GA*, pp. 1–20.

[5] N. Nguyen, "Elastically Shaped Future Air Vehicle Concept," *NASA Innovation Fund Award 2010 Report, October 2010, Submitted to NASA Innovative Partnerships Program.*

[6] N. Nguyen, K. Trinh, K. Reynolds, J. Kless, M. Aftosmis, J. Urnes, and C. Nguyen, N., Trinh, K., Reynolds, K., Kless, J., Aftosmis, M., Urnes, J., and Ippolito, “Elastically Shaped Wing Optimization and Aircraft Concept for Improved Cruise Efficiency,” *AIAA Aerospace Sciences Meeting, AIAA-2013-0141, January 2013.*

[7] Alexander Bolonkin and Glenn B. Gilyard, “Estimated Benefits of Variable-Geometry Wing Camber Control for Transport Aircraft,” *NASA/TM-1999-206586*, 1999.

[8] J.-P. Marec, “Drag Reduction: a Major Task for Research,” *Proceedings of the CEAS/DragNet European Drag Reduction Conference, 19-21 June 2000, Potsdam, Germany.*

[9] Glenn B. Gilyard, Jennifer Georgie, and J. S.Barnicki, “Flight Test of an Adaptive Configuration Optimization System for Transport Aircraft,” *NASA TM-1999-206569*, p. 14, 1999.

[10] “Camber (Aerodynamics).” [Online]. Available: *http : //en.wikipedia.org/wiki/Camber_(aerodynamics)#cite_note* − 1

[11] J. E. Green, “Laminar flow control-back to the future,” *AIAA paper*, vol. 3738, p. 2008, 2008.

[12] Urnes, James and Nguyen, Nhan and Ippolito, Corey and Totah, Joseph and Trinh, Khanh and Ting, Eric, “A Mission Adaptive Variable Camber Flap Control System to Optimize High Lift and Cruise Lift to Drag Ratios of

Future N+ 3 Transport Aircraft," *51st AIAA Aerospace Sciences Meeting, Grapevine, TX*, 2013.

[13] N. Nguyen, N. Precup, J. Urnes, C. Nelson, E. Ting, S. Lebofsky, and E. Livne, "Experimental investigation of a flexible wing with a variable camber continuous trailing edge flap design," in *AIAA Aviation 2014 Conference, Atlnta Georgia*, 2014.

[14] P.-C. Chen, Z. Zhou, S. S. Ghoman, and N. Falkiewicz, "Low-weight low-drag truss-braced wing design using variable camber continuous trailing edge flaps," in *56th AIAA/ASCE/AHS/ASC Structures, Structural Dynamics, and Materials Conference*, 2015, p. 1176.

[15] N. H. McClamroch, *Steady aircraft flight and performance.* Princeton University Press, 2011.

[16] "Cruise Flight." [Online]. Available: http://aerostudents.com/files/aircraftPerformance2/cruiseFlight.pdf

[17] S. V. Thibert JJ, Reneaux V, "ON-ERA activities in drag Reduction,," *Cognr. Int. Counc. Aero. Sci*, vol. 17, pp. 1053–64, 1990.

[18] M. Jahanmiri, "Aircraft drag reduction: An overview," Chalmers University of Technology, Tech. Rep., 2011.

[19] J. Reneaux *et al.*, "Overview on drag reduction technologies for civil transport aircraft," *ONERA: Tire a Part*, vol. 153, pp. 1–18, 2004.

[20] J. Slooff, “Subsonic transport aircraft-new challenges and opportunities for aerodynamic research the 36th lanchester lecture,” 2002.

[21] A. Sareen, R. W. Deters, S. P. Henry, and M. S. Selig, “Drag reduction using riblet film applied to airfoils for wind turbines,” *Journal of Solar Energy Engineering*, vol. 136, no. 2, p. 021007, 2014.

[22] J. Anders, “Airfoil large eddy breakup devices for turbulent drag reduction,” 1986.

[23] D. M. Bushnell, *Viscous drag reduction in boundary layers.* AIAA, 1990, vol. 123.

[24] P. Viswanath, “Aircraft viscous drag reduction using riblets,” *Progress in Aerospace Sciences*, vol. 38, no. 6, pp. 571–600, 2002.

[25] M. J. Walsh, “Riblets as a viscous drag reduction technique,” *AIAA journal*, vol. 21, no. 4, pp. 485–486, 1983.

[26] J. C. Lin, S. K. Robinson, R. J. McGhee, and W. O. Valarezo, “Separation control on high-lift airfoils via micro-vortex generators,” *Journal of aircraft*, vol. 31, no. 6, pp. 1317–1323, 1994.

[27] A. Seifert, T. Bachar, D. Koss, M. Shepshelovich, and I. Wygnanskil, “Oscillatory blowing: a tool to delay boundary-layer separation,” *AIAA journal*, vol. 31, no. 11, pp. 2052–2060, 1993.

[28] L. Gao, H. Zhang, Y. Liu, and S. Han, “Effects of vortex generators on a blunt trailing-edge airfoil for wind turbines,” *Renewable Energy*, vol. 76, pp. 303–311, 2015.

[29] N. T. Nguyen, N. Precup, E. Livne, J. Urnes, E. Dickey, C. Nelson, J. Chiew, D. Rodriguez, E. Ting, and S. Lebofsky, “Wind tunnel investigation of a flexible wing high-lift configuration with a variable camber continuous trailing edge flap design,” in *33rd AIAA Applied Aerodynamics Conference, AIAA-2015-2417*, 2015.

[30] X. Zheng and Y. Yan, “A biomimetic smart control of viscous drag reduction,” *Advances in Natural Science*, vol. 3, no. 2, pp. 139–151, 2010.

[31] Ronald D. Joslin, “Aircraft laminar flow control,” *Annual Review of FLuid Mechanics,ProQuest*, 1998.

[32] “Boundary layer.” [Online]. Available: https://en.wikipedia.org/wiki/Boundary_layer

[33] A. L. Braslow, “A History of Suction-Type Laminar-Flow Control with Emphasis on Flight Research,” *MOnograph Aerospace History , Number 13*, 1999.

[34] Boeing Commercial Airplane Co., “Natural Laminar FlowAirfoil Analysis and Trade Studies Final Report,” *NASA CR 159029,1979.*

[35] “SWEPTDES, A computer program of RAeS TDM 6312 for calculating the subcritical inviscid flow over a finite wing, with compressibility effects updated to the standard of ESDU TDM 7312.”

[36] J. Green, "Civil aviation and the environmental challenge," *Aeronautical Journal*, vol. 107, no. 1072, pp. 281–300, 2003.

[37] "FARNBOROUGH: Aero secrets of Boeings new Dreamliner." [Online]. Available: https://www.flightglobal.com/news/articles/farnborough-aero-secrets-of-boeings-new-dreamline-401784/

[38] "Boeing tests hybrid laminar flow control for 787-9." [Online]. Available: https://www.flightglobal.com/news/articles/boeing-tests-hybrid-laminar-flow-control-for-787-9-358123/

[39] "Boeing Ditches Drag Reduction System For 777X." [Online]. Available: http://aviationweek.com/commercial-aviation/boeing-ditches-drag-reduction-system-777x

[40] "Boeing 777." [Online]. Available: https://en.wikipedia.org/wiki/Boeing_777

[41] B. Smith, "The boeing 777," *Advanced Materials and Processes*, vol. 161, no. 9, pp. 41–44, 2003.

[42] "Boeing 787 Dreamliner." [Online]. Available: https://en.wikipedia.org/wiki/Boeing_787_Dreamliner

[43] D. L. Rodriguez, M. J. Aftosmis, M. Nemec, and S. C. Smith, "Static aeroelastic analysis with an inviscid cartesian method," *AIAA Paper 2014*, vol. 836, 2014.

[44] D. Nguyen, N. Nguyen, and K. Trinh, "Finite element modeling and vibration analysis of aeroelastic wing structures," in *51st AIAA Aerospace Sciences Meeting including the New Horizons Forum and Aerospace Exposition*, 2013, p. 58.

[45] "Development of Variable Camber Continuous Trailing Edge Flap System," *Boeing Report No. 2012X0015, October 4, 2012.*

[46] T. L. Jordan, W. M. Langford, C. M. Belcastro, J. M. Foster, G. H. Shah, G. Howland, and R. Kidd, "Development of a Dynamically Scaled Generic Transport Model Testbed for Flight Research Experiments," *AUVSI Unmanned Unlimited, Arlington, VA, 2004.*

[47] C. Morris, J. Sheahan, J. Dykman, D. Clingman, and J. M. Urnes, "Control system design for a variable camber continuous trailing edge flap system on an elastic wing," in *55th AIAA/ASMe/ASCE/AHS/SC Structures, Structural Dynamics, and Materials Conference*, 2014, p. 0835.

[48] N. Nguyen, E. Ting, and S. Lebofsky, "Aeroelastic analysis of a flexible wing wind tunnel model with variable camber continuous trailing edge flap design," *56th AIAA/ASCE/AHS/ASC Structures, Structural Dynamics, and Materials Conference*, 2015.

[49] N. Precup, M. Mor, and E. Livne, "The design, construction, and tests of a concept aeroelastic wind tunnel model of a high-lift variable camber continuous trailing edge flap (hl-vcctef) wing configuration," in *56th*

AIAA/ASCE/AHS/ASC Structures, Structural Dynamics, and Materials Conference, 2015, p. 1406.

[50] S. S.-M. Swei, G. G. Zhu, and N. Nguyen, "Lmi-based multiobjective optimization and control of flexible aircraft using vcctef," in *56th AIAA/ASCE/AHS/ASC Structures, Structural Dynamics, and Materials Conference*, 2015, p. 1844.

[51] S. S.-M. Swei and N. Nguyen, "Aeroelastic wing shaping control subject to actuation constraints," in *55th AIAA/ASMe/ASCE/AHS/SC Structures, Structural Dynamics, and Materials Conference*, 2014, p. 1041.

[52] J. Dykman, H. Truong, and J. Urnes, "Active control for elastic wing structure dynamic modes," *56th AIAA/ASCE/AHS/ASC Structures, Structural Dynamics, and Materials Conference*, 2015.

[53] U. K. Kaul and N. T. Nguyen, "A 3-d computational study of a variable camber continuous trailing edge flap (vcctef) spanwise segment," *33rd AIAA Applied Aerodynamics Conference*, 2015.

[54] H. D. Akaydin, S. Moini-Yekta, J. A. Housman, and N. Nguyen, "Use of a viscous flow simulation code for static aeroelastic analysis of a wing at high-lift conditions," in *33rd AIAA Applied Aerodynamics Conference*, 2015, p. 2418.

[55] J. D. Bošković, R. Wise, and J. A. Jackson, “Drag identification and reduction technology (direct) for commercial aircraft,” *15th Dynamics Specialists Conference, AIAA SciTech*, 2016.

[56] Y. Liu and E. Stumpf, “Variable camber application to aircraft in formation flight,” in *54th AIAA Aerospace Sciences Meeting*, 2016, p. 0773.

[57] D. C. Wilcox, *Turbulence Modelling for CFD, DCW Industries Inc., California, USA*. ISBN 0-9636051-5-1, 2000.

[58] E. Shames, *Mechanics of Fluid Flow*, 4th ed. McGraw-Hill, Inc., 2003.

[59] P. R. Spalart and S. R. Allmaras, “A One-Equation Turbulence Model for Aerodynamic Flows,,” *AIAA 92-0439,AIAA 30th Aerospace Sciences Meeting and Exhibit,, Reno, NV,1992.*

[60] D. K. Walters and D. Cokljat, “A three-equation eddy-viscosity model for reynolds-averaged navier–stokes simulations of transitional flow,” *Journal of fluids engineering*, vol. 130, no. 12, p. 121401, 2008.

[61] ANSYS Inc., “ANSYS Fluent Theory Guide, Release 15.0,” Tech. Rep., 2013.

[62] T. Holst, “Numerical computation of transonic flow governed by the full-potential equation,” *NASA Technical Memorandum 84310*, 1983.

[63] R. H. Pletcher, J. C. Tannehill, and D. Anderson, *Computational fluid mechanics and heat transfer*. CRC Press, 2012.

[64] Amjad, Ali Pasha, “Application of shock-unsteadiness model to hypersonic shock/turbulent boundary-layer interaction,” Ph.D. dissertation, I.I.T. Bombay, 2012.

[65] M. Munk, “General theory of thin wing sections,” *NACA Rep*, vol. 142, p. 243, 1922.

[66] J. D. Anderson Jr, *Fundamentals of aerodynamics.* Tata McGraw-Hill Education, 1985.

[67] T. Von Karman, “Mechanical similitude and turbulence,” *International Journal of Computational Fluid Dynamics*, vol. 5, no. 611, pp. 58–76, 1931.

[68] S. B. Pope, *Turbulent flows.* Cambridge university press, 2000.

[69] ANSYS Inc., “Fluent 12.0/12.1 documentation,” *Users Guide Manual*, 2009.

[70] I. Abbot and von Doendoff, “Theory of wing sections,” *Dover Publications New York*, 1959.

[71] C. Ladson, “Effects of independent variation of mach and reynolds numbers on the low-speed aerodynamic characteristics of the naca 0012 airfoil section,” *NASA-TM-4074,1988.*

[72] N. Gregory and C. OReilly, “Low-speed aerodynamic characteristics of naca 0012 aerofoil section, including the effects of upper-surface roughness simulating hoar frost(low speed aerodynamic characteristics of airfoil profiles including effects of upper surface roughness simulating hoar frost),” 1970.

[73] Langley Research Centre, “2D NACA 0012 Airfoil Validation Case.” [Online]. Available: http://turbmodels.larc.nasa.gov/naca0012_val.html

[74] “NACA 6 digit.” [Online]. Available: http://people.clarkson.edu/ pmarzocc/AE429/The NACA airfoil series.pdf

[75] W. Timmer, “An overview of naca 6-digit airfoil series characteristics with reference to airfoils for large wind turbine blades,” *47th AIAA Aerospace Sciences Meeting*, 2009.

[76] Laurence K,Loftin Jr and William J Bursnall, “The effects of variations in reynolds number between 3.0 x 10^6 and 25.0 x 10^6 upon the aerodynamic characteristics of a number of naca 6-series airfoil sections,” *NACA-TR-964*, 1950.

[77] Cook, P.H., M.A. McDonald, M.C.P. Firmin, “Aerofoil rae 2822 - pressure distributions, and boundary layer and wake measurements,” *Experimental Data Base for Computer Program Assessment, AGARD Report AR 138*, 1979.

[78] J. Barche *et al.*, “Experimental data base for computer program assessment,” *AGARD-Report AGARD-AR-138*, pp. 2002–0843, 1979.

[79] D. C. Eleni, T. I. Athanasios, and M. P. Dionissios, “Evaluation of the turbulence models for the simulation of the flow over a National Advisory Committee for Aeronautics (NACA) 0012 airfoil,” *Journal of Mechanical Engineering Research*, vol. 4, no. 3, pp. 100–111, Mar. 2012.

[80] Ü. Kaynak, S. Ç. Çakmakçıoğlu, and M. S. Genç, "Transition at low-re numbers for some airfoils at high subsonic mach numbers," 2012.

[81] F. Palacios, T. D. Economon, A. C. Aranake, S. R. Copeland, A. K. Lonkar, T. W. Lukaczyk, D. E. Manosalvas, K. R. Naik, A. S. Padrón, B. Tracey *et al.*, "Stanford university unstructured (su2): Open-source analysis and design technology for turbulent flows," *AIAA paper*, vol. 243, pp. 13–17, 2014.

[82] P. Schneider, "NURB Curves: A Guide for the Uninitiated," 2014.

[83] "GAMBIT Modeling Guide." [Online]. Available: $https : //www.sharcnet.ca/Software/Gambit/html/modeling_guide/mgtoc.htm$

[84] Mark Drela and Youngren Harold, "XFOIL 6.9 User Primer," Cambridge, 2001.

[85] Eppler Richard, "Airfoil Program System,PROFILE07 User's Guide," Stuttgart, Germany, 2007.

[86] "Y+ Wall Distance Estimation." [Online]. Available: $http : //www.cfd - online.com/Tools/yplus.php$

[87] "Us standard atmosphere, 1976," US Airforce, NOAA-S/T, Tech. Rep., 1976.

[88] "U.S Standard Atmosphere Air Properties in SI Units." [Online]. Available: $http : //www.engineeringtoolbox.com/standard - atmosphere - d\_604.html$

[89] M. Drela, "Xfoil 6.97," *XFOIL Subsonic Airfoil Development System*, 2012.

APPENDIX A

In this section the coefficient of the lift and drag values of the various VCCTEF configurations are given.The fractional contribution of the pressure and viscous component is also shown along with the actual values. As the AoA increases it is seen that pressure component of drag increases. Pressure component of lift is contributing mostly in the lift generation.

Table A.1: VCCTEF 123 Case: Pressure and viscous contribution to C_d

	Drag Coefficient			Fractional Contribution	
AoA	Pressure	Viscous	Total	Pressure	Viscous
-2	0.002635586	0.005187	0.007823	0.336902	0.663098085
-1	0.003419953	0.00519	0.00861	0.397229	0.60277145
0	0.004584212	0.005138	0.009722	0.47151	0.528490215
1.1	0.006628589	0.005034	0.011662	0.568382	0.431617886
2	0.011830257	0.004867	0.016698	0.708496	0.291503855
3	0.030342326	0.004613	0.034955	0.868036	0.131963969
4	0.048854395	0.004358	0.053213	0.918098	0.081901578
5	0.074430349	0.003998	0.078428	0.949024	0.050976426

Table A.2: VCCTEF 123 Case: Pressure and viscous contribution to C_l

	Lift Coefficient			Fractional Contribution	
AoA	Pressure	Viscous	Total	Pressure	Viscous
-2	0.618964	6.40E-06	0.61897	0.99999	1.03E-05
-1	0.779131	5.42E-05	0.779185	0.99993	6.96E-05
0	0.9605	9.84E-05	0.960599	0.999898	0.000102
1.1	1.12657	0.000127	1.126696	0.999888	0.000112
2	1.294448	0.000177	1.294625	0.999863	0.000137
3	1.462325	0.000227	1.462553	0.999844	0.000156
4	1.496822	0.000259	1.497081	0.999827	0.000173
5	1.391664	0.000262	1.391927	0.999812	0.000188

Table A.3: VCCTEF 222 Case: Pressure and viscous contribution to C_d

	Drag Coefficient			Fractional Contribution	
AoA	Pressure	Viscous	Total	Pressure	Viscous
-2	0.002635586	0.005187	0.007823	0.336902	0.663098085
-1	0.003419953	0.00519	0.00861	0.397229	0.60277145
0	0.004584212	0.005138	0.009722	0.47151	0.528490215
1.1	0.006628589	0.005034	0.011662	0.568382	0.431617886
2	0.011830257	0.004867	0.016698	0.708496	0.291503855
3	0.030342326	0.004613	0.034955	0.868036	0.131963969
4	0.048854395	0.004358	0.053213	0.918098	0.081901578
5	0.074430349	0.003998	0.078428	0.949024	0.050976426

Table A.4: VCCTEF 222 Case: Pressure and viscous contribution to C_l

	Lift Coefficient			Fractional Contribution	
AoA	Pressure	Viscous	Total	Pressure	Viscous
-2	0.507601	-4.42E-05	0.507557	1.000087	-8.7E-05
-1	0.666086	6.28E-06	0.666092	0.999991	9.42E-06
0	0.824572	5.68E-05	0.824628	0.999931	6.88E-05
1.1	1.00598	1.01E-04	1.006081	0.9999	9.99E-05
2	1.180728	0.000129	1.180857	0.999891	0.000109
3	1.334872	0.000181	1.335053	0.999865	0.000135
4	1.489017	0.000233	1.48925	0.999844	0.000156
5	1.49912	0.000116	1.499236	0.999922	7.77E-05

Table A.5: VCCTEF 321 Case: Pressure and viscous contribution to C_d

	Drag Coefficient			Fractional Contribution	
AoA	Pressure	Viscous	Total	Pressure	Viscous
-2	0.004303574	0.005143	0.009446	0.455584	0.544416442
-1	0.005918668	0.005098	0.011016	0.537271	0.462728952
0	0.007533763	0.005052	0.012586	0.59858	0.401419516
1.1	0.010279235	0.004933	0.015212	0.675736	0.32426357
2	0.015856291	0.004777	0.020633	0.768488	0.231511569
3	0.035808414	0.004535	0.040344	0.887581	0.112418813
4	0.055760536	0.004294	0.060055	0.928498	0.071501819
5	0.0792615	0.003914	0.083175	0.952947	0.04705277

Table A.6: VCCTEF 321 Case: Pressure and viscous contribution to C_l

	Lift Coefficient			Fractional Contribution	
AoA	Pressure	Viscous	Total	Pressure	Viscous
-2	0.552275	-3.91E-05	0.552236	1.000071	-7.1E-05
-1	0.707331	1.1E-05	0.707342	0.999984	1.56E-05
0	0.862386	6.11E-05	0.862447	0.999929	7.08E-05
1.1	1.042657	1.04E-04	1.042761	0.9999	9.98E-05
2	1.228881	0.000133	1.229013	0.999892	0.000108
3	1.365733	0.000184	1.365917	0.999865	0.000135
4	1.502585	0.000236	1.50282	0.999843	0.000157
5	1.488069	0.000255	1.488324	0.999829	0.000171

Table A.7: VCCTEF 33 Case: Pressure and viscous contribution to C_d

	Drag Coefficient			Fractional Contribution	
AoA	Pressure	Viscous	Total	Pressure	Viscous
0	0.007139463	0.005076	0.012215	0.584484	0.415515992
1.1	0.009721252	0.004959	0.014681	0.662177	0.337822881
2	0.015303776	0.004798	0.020102	0.761299	0.238701271

Table A.8: VCCTEF 33 Case: Pressure and viscous contribution to C_l

	Lift Coefficient			Fractional Contribution	
AoA	Pressure	Viscous	Total	Pressure	Viscous
0	0.848468	6.04E-05	0.848529	0.999929	7.12E-05
1.1	1.028328	1.04E-04	1.028432	0.999899	0.000101
2	1.20904	0.000132	1.209172	0.999891	0.000109

Table A.9: VCCTEF 6 Case: Pressure and viscous contribution to C_d

	Drag Coefficient			Fractional Contribution	
AoA	Pressure	Viscous	Total	Pressure	Viscous
-2	0.0097232	0.005006	0.014729	0.660152	0.339847646
-1	0.011660596	0.004972	0.016632	0.701088	0.298912516
0	0.013652514	0.004889	0.018541	0.736336	0.263663979
1.1	0.016402479	0.004771	0.021174	0.774659	0.22534138
2	0.021412082	0.004649	0.026061	0.821617	0.178382546
3	0.041346896	0.004437	0.045783	0.903098	0.096901963
4	0.061281709	0.004224	0.065506	0.935514	0.064485702
5	0.086258034	0.003891	0.090149	0.956839	0.043161027

Table A.10: VCCTEF 6 Case: Pressure and viscous contribution to C_l

	Lift Coefficient			Fractional Contribution	
AoA	Pressure	Viscous	Total	Pressure	Viscous
-2	0.599074	-2.05E-05	0.599054	1.000034	-3.4E-05
-1	0.74138	3.32E-05	0.741414	0.999955	4.47E-05
0	0.921083	7.82E-05	0.921161	0.999911	8.86E-05
1.1	1.1051602	0.00012	1.1051722	0.999886	0.000114
2	1.27198	0.000146	1.272126	0.999885	0.000115
3	1.388142	0.000191	1.388333	0.999862	0.000138
4	1.504304	0.000237	1.50454	0.999843	0.000157
5	1.500372	0.000246	1.500618	0.999836	0.000164

APPENDIX B

The contours of various VCCTEF configurations are shown in this section. In the pressure and Mach contours the coalition of contour lines implies shock formation. Based on the Fig. B.1 and B.2 a direct relation between the pressure and Mach contours can be observed.

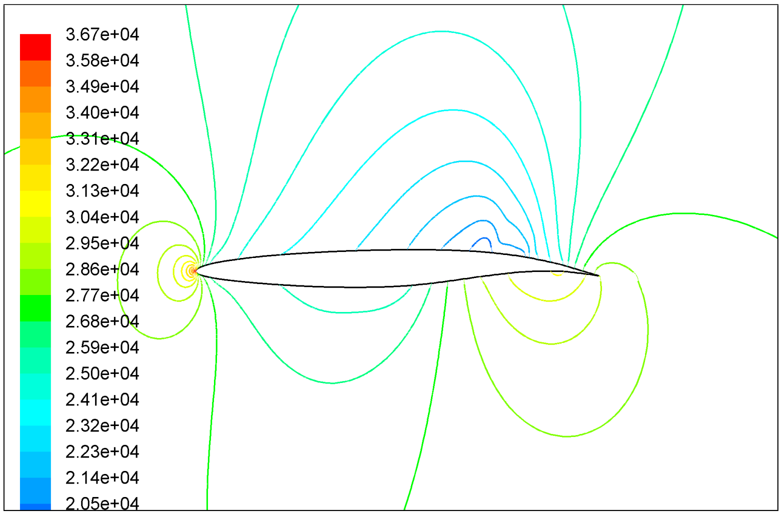

Figure B.1: Pressure contour of VCCTEF 123 at -2 AoA at M =0.7

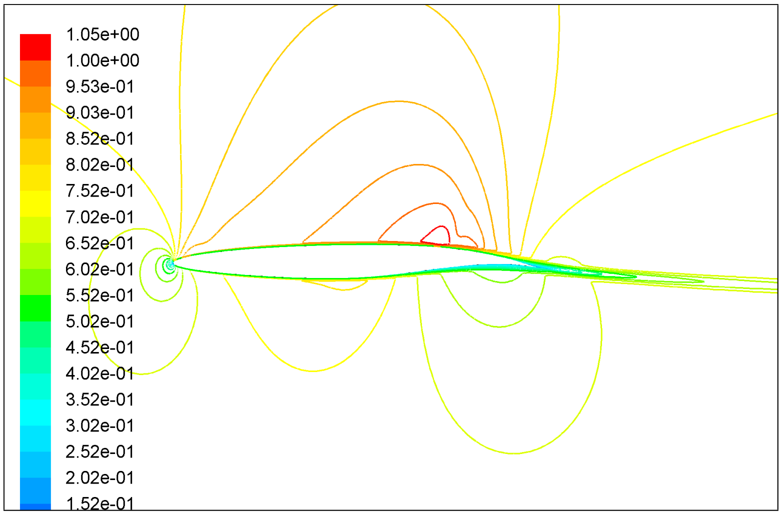

Figure B.2: Mach contour of VCCTEF 123 at -2 AoA at M =0.7

The Fig. B.3 shows that at AoA = 0° there is a slight shock formation on the upper surface of the airfoil, near the leading edge (L.E shock) and about 75% of the chord length (aft-shock). This is also seen in the C_p vs. x/c plot in the Fig. 5.33 The shock formation is also visible in the Fig.B.4. The maximum Mach

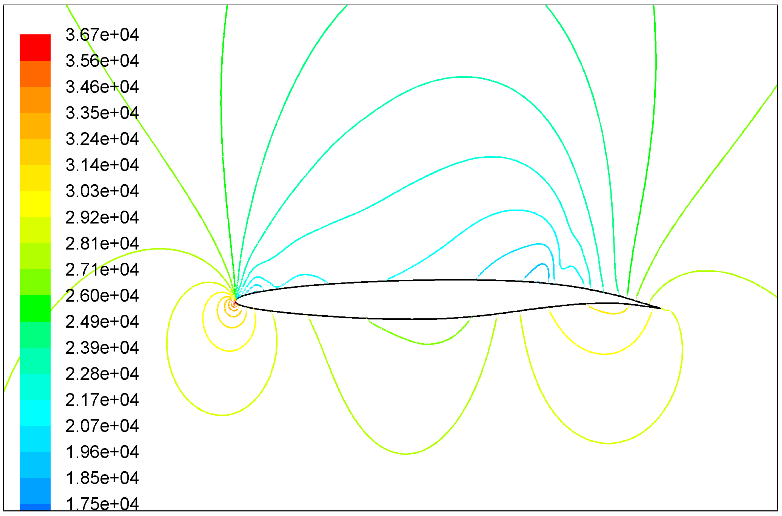

Figure B.3: Pressure contour of VCCTEF 123 at 0 AoA at M =0.7

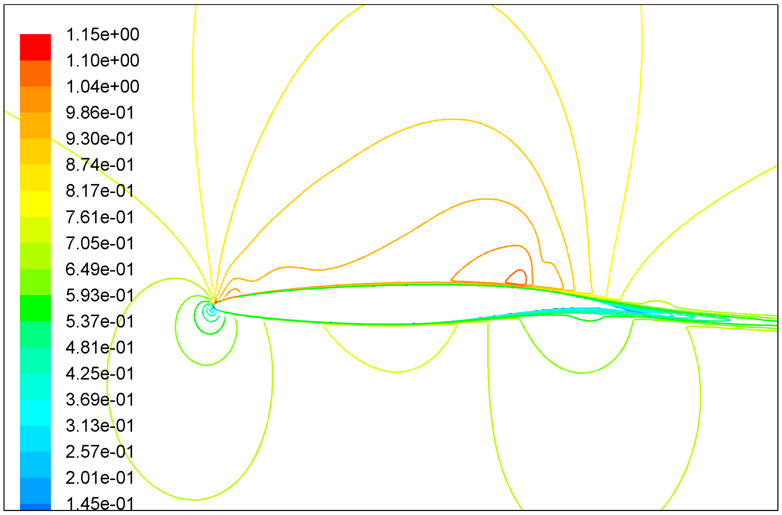

Figure B.4: Mach contour of VCCTEF 123 at 0 AoA at M =0.7

number that is reached on the surface is 1.15.

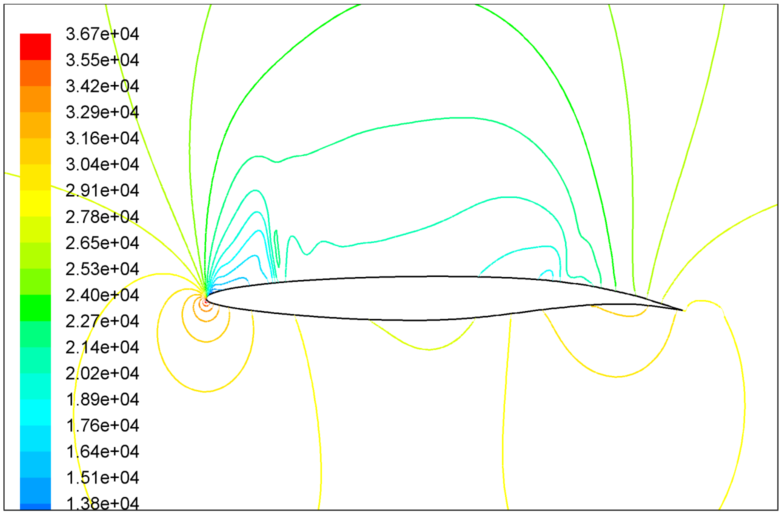

Figure B.5: Pressure contour of VCCTEF 123 at 1.1 AoA at M =0.7

The shock at the leading edge moves towards the right as the AoA is increased from 0° to 1.1° as shown in the Fig. B.5 and B.6. The shock at 75 % of the chord (aft-shock) seems to be almost at the same position.

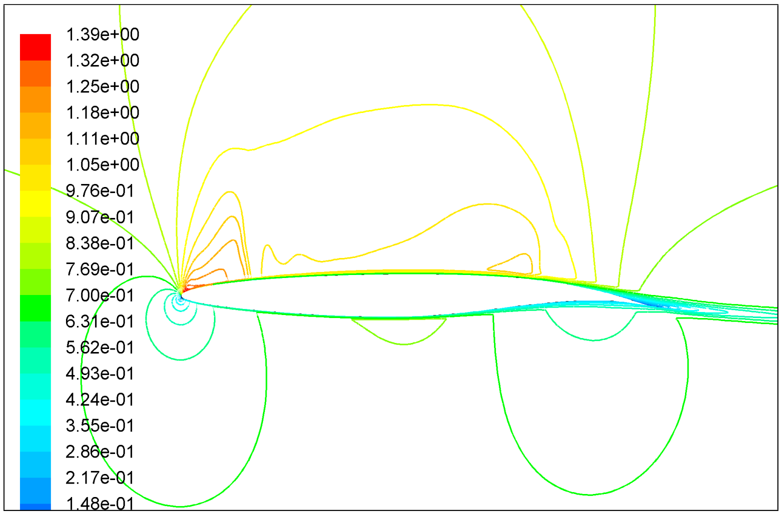

Figure B.6: Mach contour of VCCTEF 123 at 1.1 AoA at M =0.7

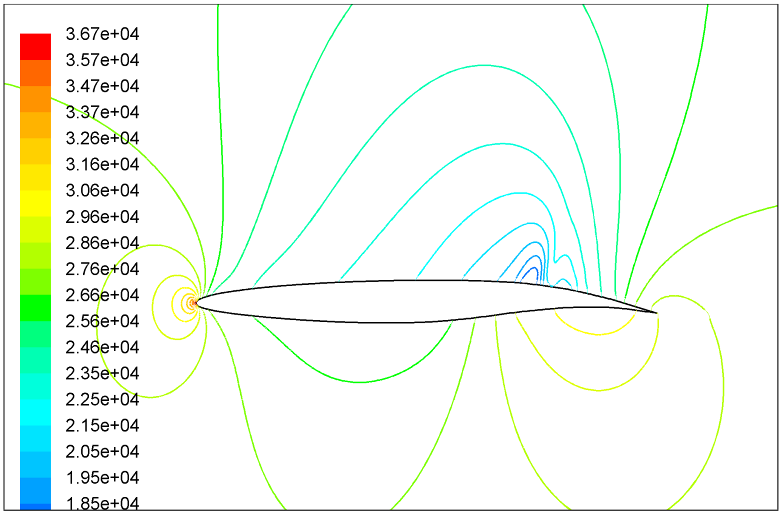

Figure B.7: Pressure contour of VCCTEF 222 at -2 AoA at M =0.7

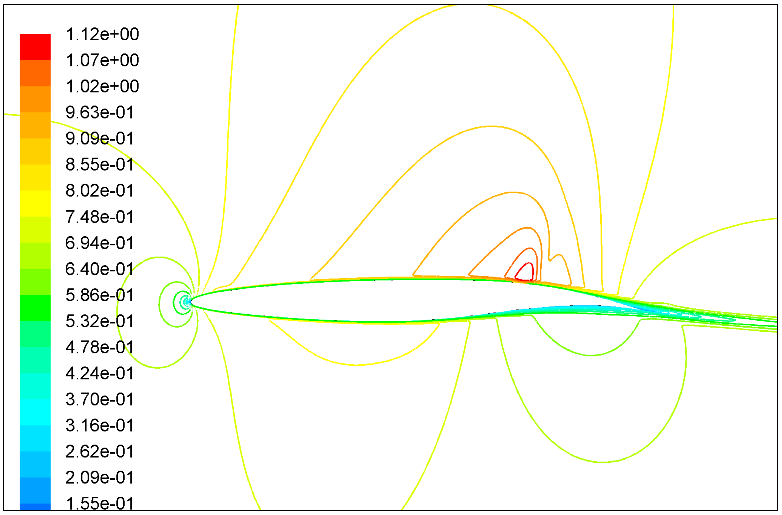

Figure B.8: Mach contour of VCCTEF 222 at -2 AoA at M =0.7

Compared to VCCTEF 123 (AoA = -2°) case, the shock of VCCTEF 222 at x/c =75% of chord seems to be slightly stronger as shown in the Fig. B.7 and Fig. B.8. The maximum Mach number on the airfoil surface is also increased from 1.05 to 1.12. There is no shock formation near the leading edge of the airfoil.

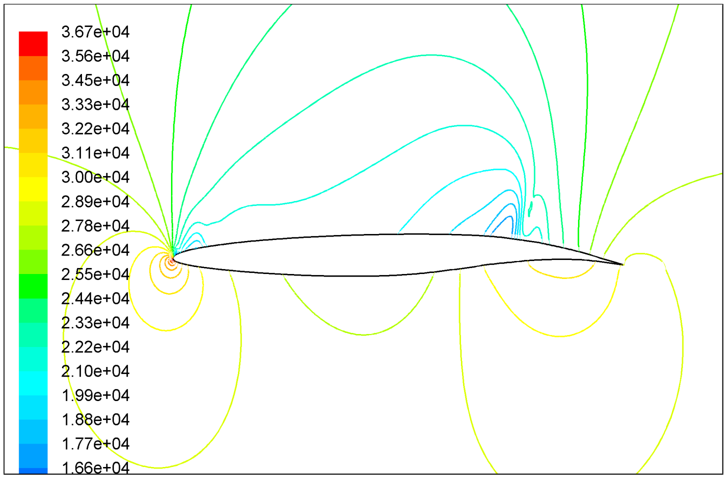

Figure B.9: Pressure contour of VCCTEF 222 at 0 AoA at M =0.7

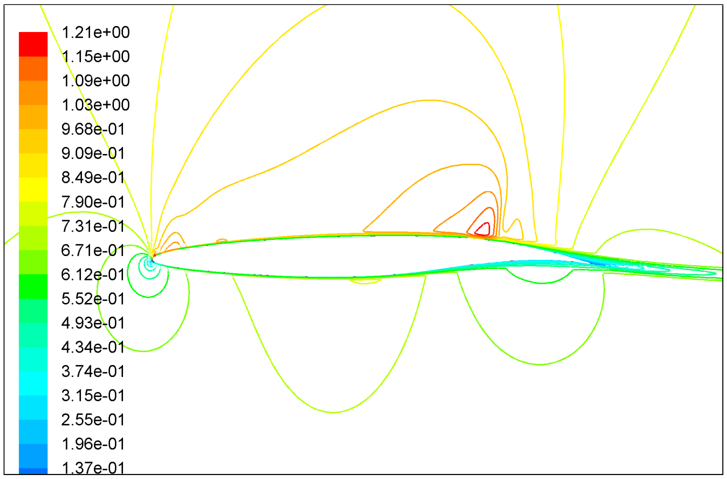

Figure B.10: Mach contour of VCCTEF 222 at 0 AoA at M =0.7

The shock formation on the upper surface of VCCTEF 222 at AoA = 0° (near the leading edge) is visible in both the pressure and Mach contour shown in the Fig. B.9 and B.10. The contour figures correlates with the pressure coefficient plot shown in the Fig. 5.33 in which shock formation is visible as the sudden decrease in C_p at x/c =0.75. The strength of VCCTEF 222 aft-shock is higher than the shock of VCCTEF 123. The maximum Mach number on the upper surface is 1.21.

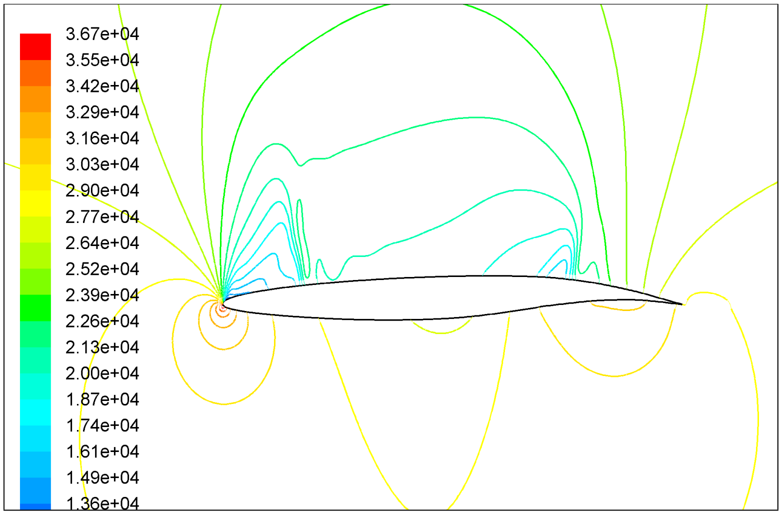

Figure B.11: Pressure contour of VCCTEF 222 at 1.1 AoA at M =0.7

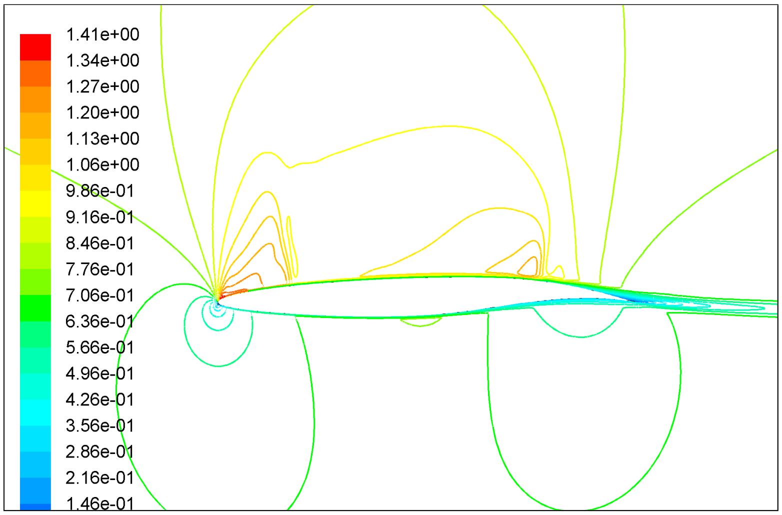

Figure B.12: Mach contour of VCCTEF 222 at 1.1 AoA at M =0.7

The leading edge shock moves to the right as the AoA is increased from 0° to 1.1° as shown in the Fig B.11 and B.12. The maximum Mach number on the surface of airfoil is 1.41. The aft-shock seems to be at the same position as the AoA = 0° case of VCCTEF 222.

The pressure and Mach contours of VCCTEF 321 at AoA =-2° is almost similar to the VCCTEF 123 and 222 contours with respect to the shock formation as shown in the Fig. B.13 and Fig. B.14. There is only one shock formation which is the aft-shock.

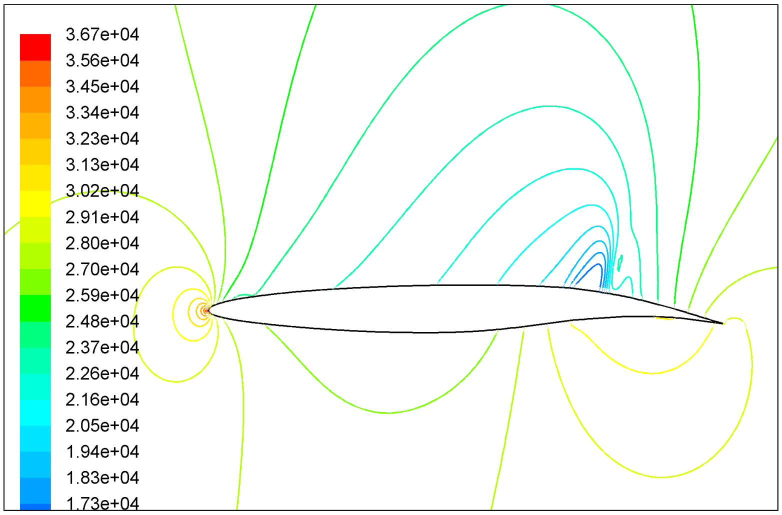

Figure B.13: Pressure contour of VCCTEF 321 at -2 AoA at M =0.7

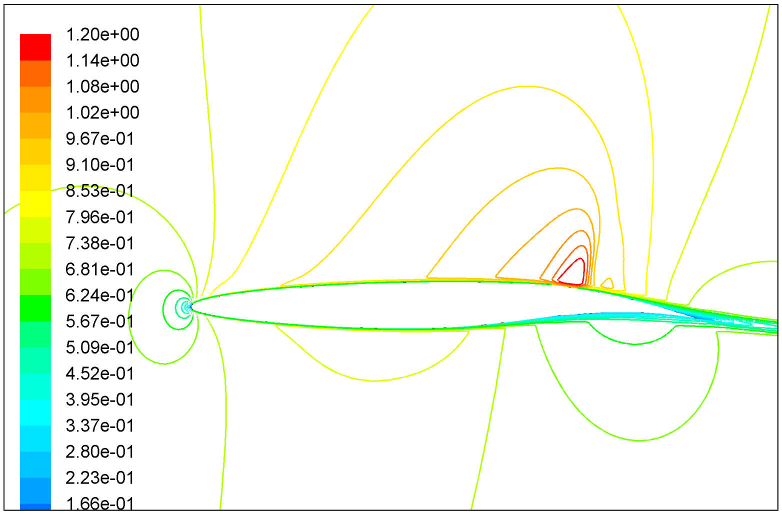

Figure B.14: Mach contour of VCCTEF 321 at -2 AoA at M =0.7

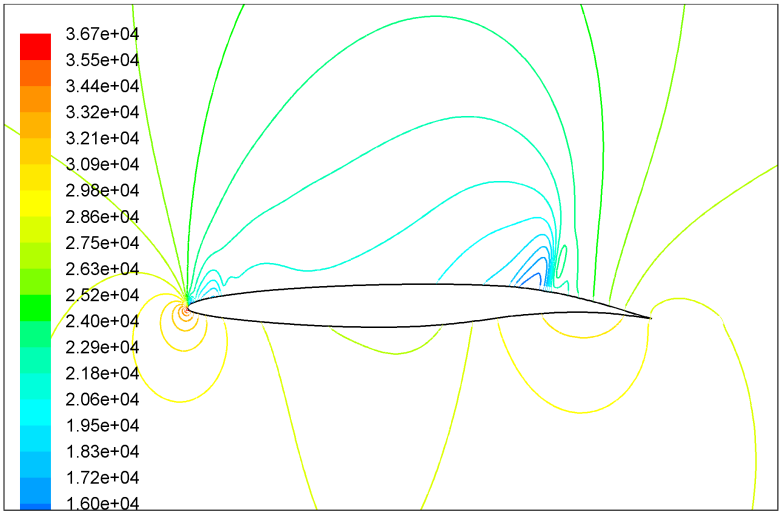

Figure B.15: Pressure contour of VCCTEF 321 at 0 AoA at M =0.7

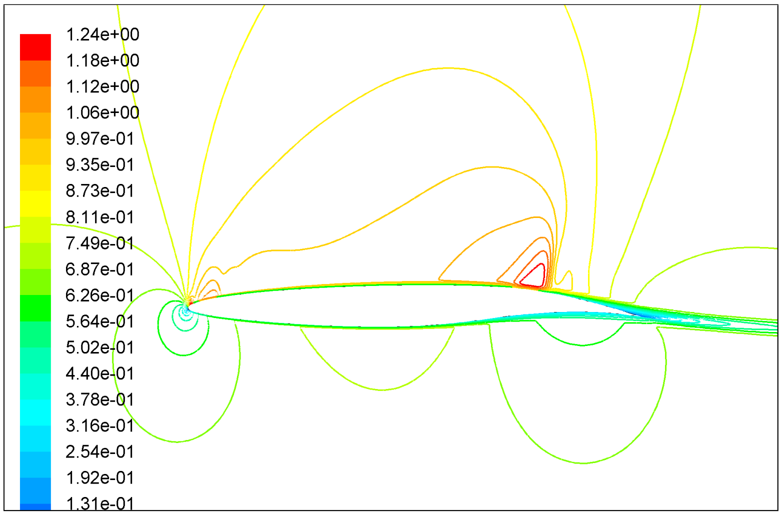

Figure B.16: Mach contour of VCCTEF 321 at 0 AoA at M =0.7

As seen in the previous figures in the present section the contour plots at AoA =0° correlate well with the pressure coefficient plot shown in the Fig. 5.33. VCCTEF 321 also have two shocks on its surface. One, near the leading edge and another at x/c $\simeq$ 75 % of the chord.

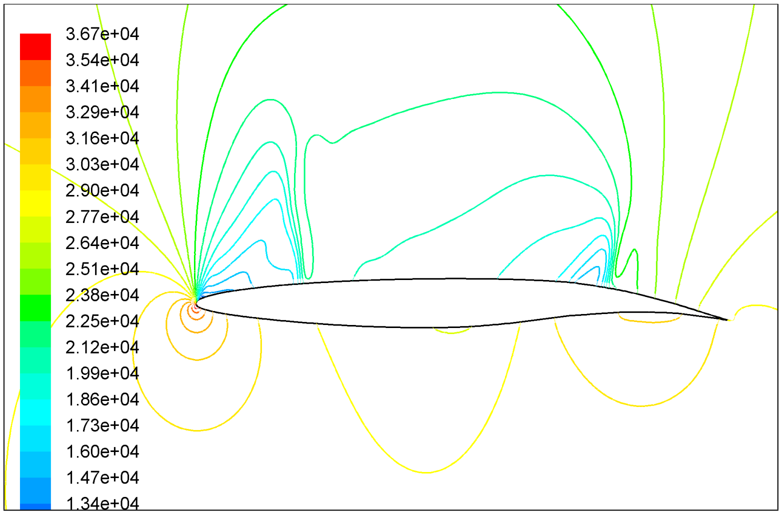

Figure B.17: Pressure contour of VCCTEF 321 at 1.1 AoA at M =0.7

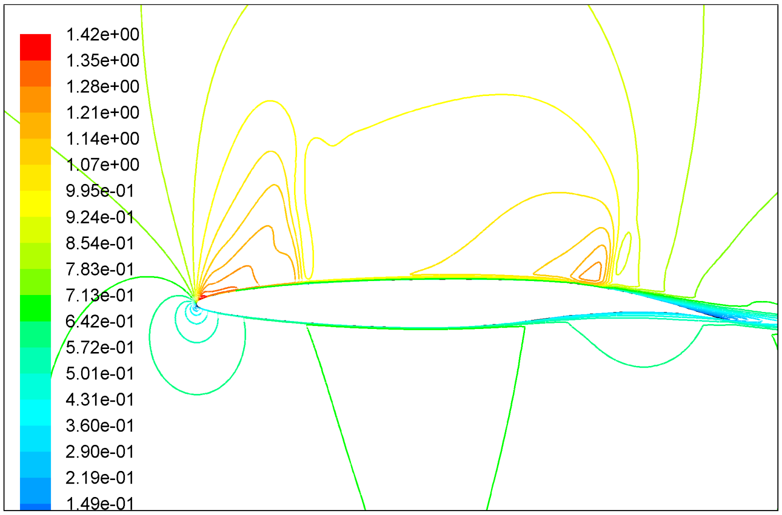

Figure B.18: Mach contour of VCCTEF 321 at 1.1 AoA at M =0.7

Compared to the previous configurations the strength of the shock near the leading edge is higher in VCCTEF 321 which is visible in the Fig. B.17 and B.18. The aft shock seems to be at the same position for all the configurations. The strength of aft shock is also stronger relative to VCCTEF 123 and 321.

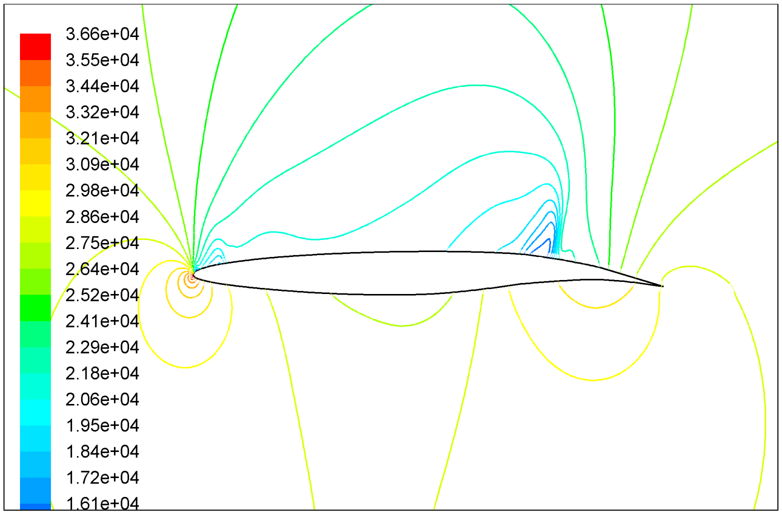

Figure B.19: Pressure contour of VCCTEF 33 at 0 AoA at M =0.7

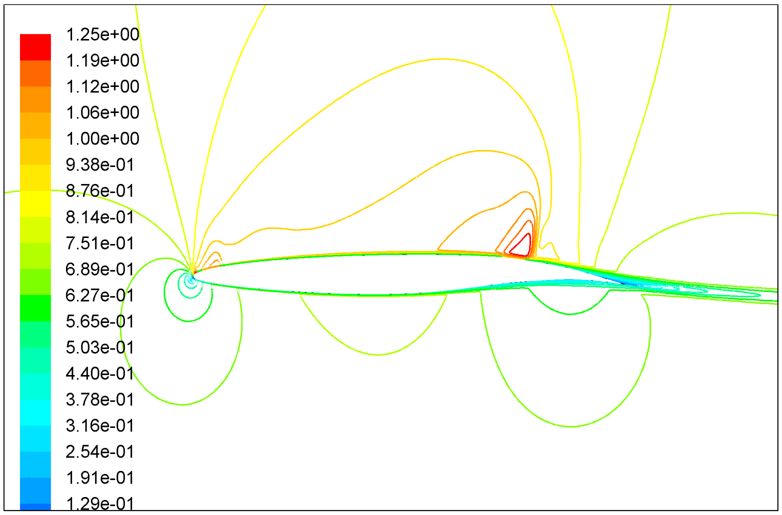

Figure B.20: Mach contour of VCCTEF 33 at 0 AoA at M =0.7

From the Fig.B.19 and B.20 it can be seen that there are two shock formations. The pressure and Mach contour of VCCTEF 321 and 33 are almost the same. The highest pressure and Mach number at AoA = 0 ° are also the same. It is due to this reason the C_p plot (Fig. 5.33) of VCCTEF 33 overlaps the VCCTEF 321 plot. Relative to VCCTEF 123 and 222 the strength of the shock of VCCTEF 33 is higher.

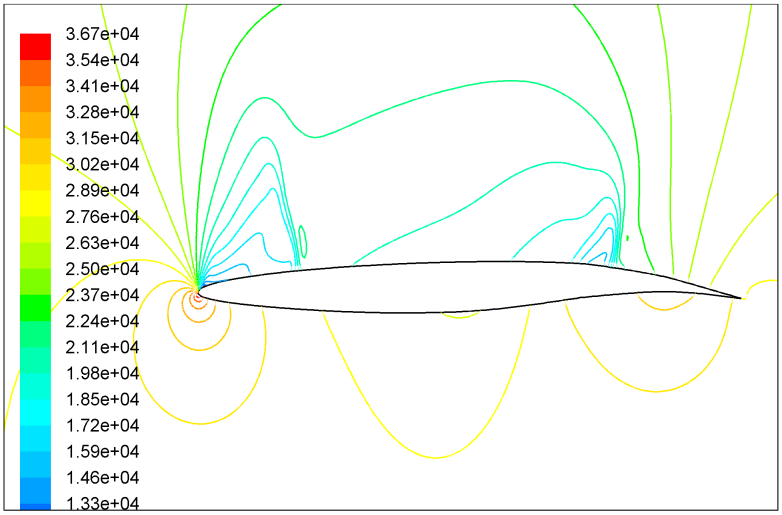

Figure B.21: Pressure contour of VCCTEF 33 at 1.1 AoA at M =0.7

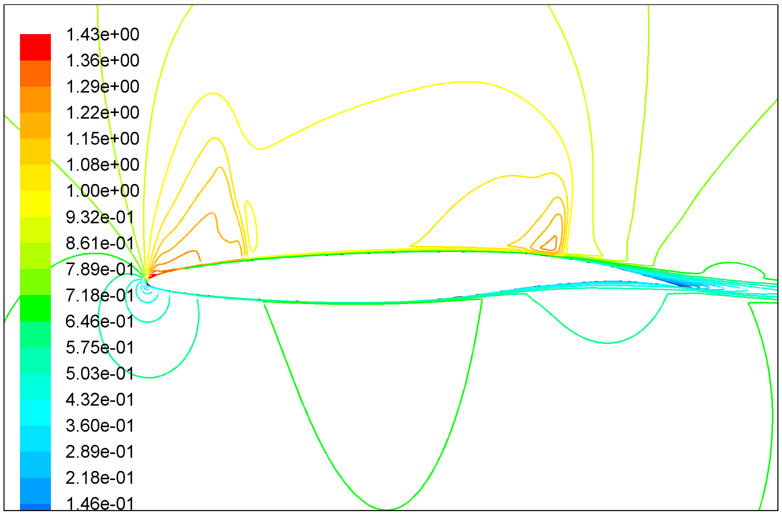

Figure B.22: Mach contour of VCCTEF 33 at 1.1 AoA at M =0.7

Like the previous configurations as the AoA of VCCTEF 33 is increased from 0° to 1.1° the leading edge shock moves towards the right as shown in the Fig. B.21 and Fig. B.22.

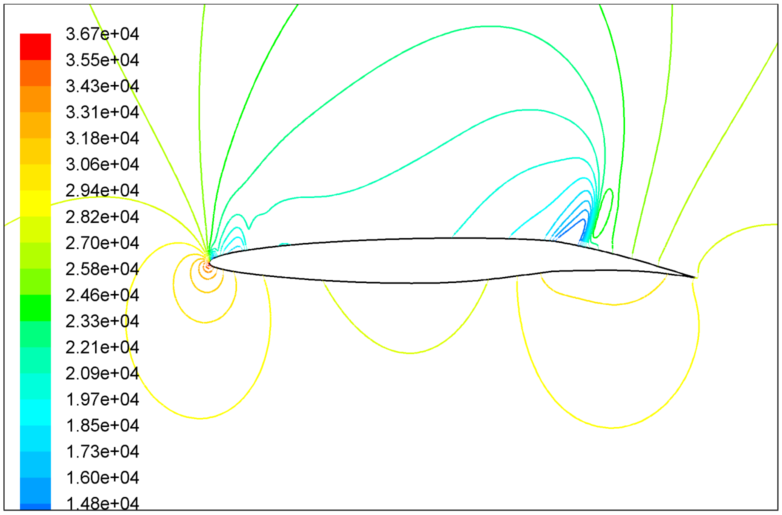

Figure B.23: Presure contour of VCCTEF 6 at 0 AoA at M =0.7

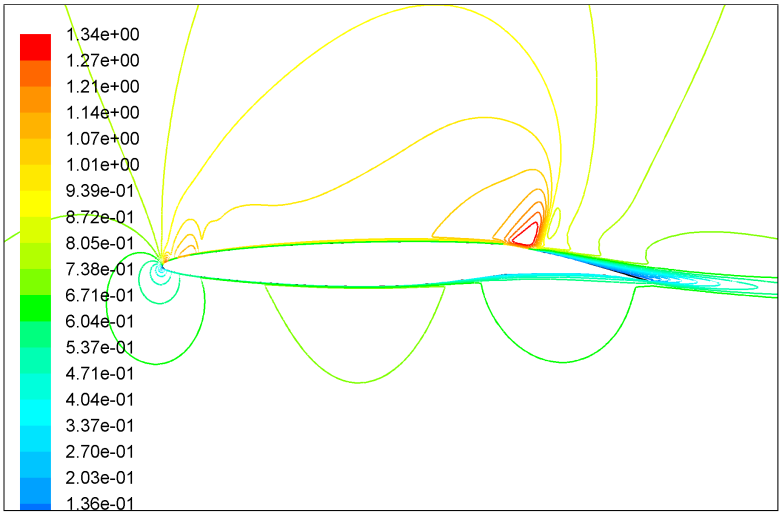

Figure B.24: Mach contour of VCCTEF 6 at 0 AoA at M =0.7

The shock formation is strongest for VCCTEF 6 at AoA =0° this is also visible in the C_p plot in the Fig. 5.33. The maximum pressure and Mach number of the airfoil at AoA =0° is highest with VCCTEF 6 (as shown in the Fig B.23 and Fig B.24). Due to which this lift and drag of the VCCTEF 6 is higher than all other configurations.

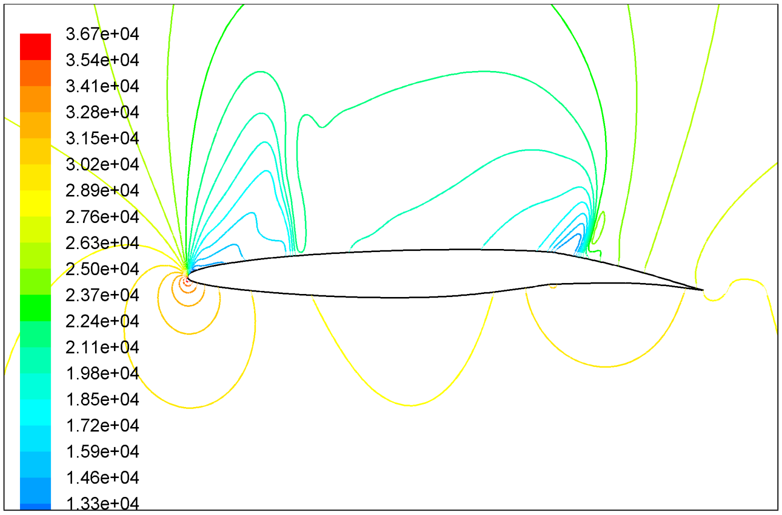

Figure B.25: Presure contour of VCCTEF 6 at 1.1 AoA at M =0.7

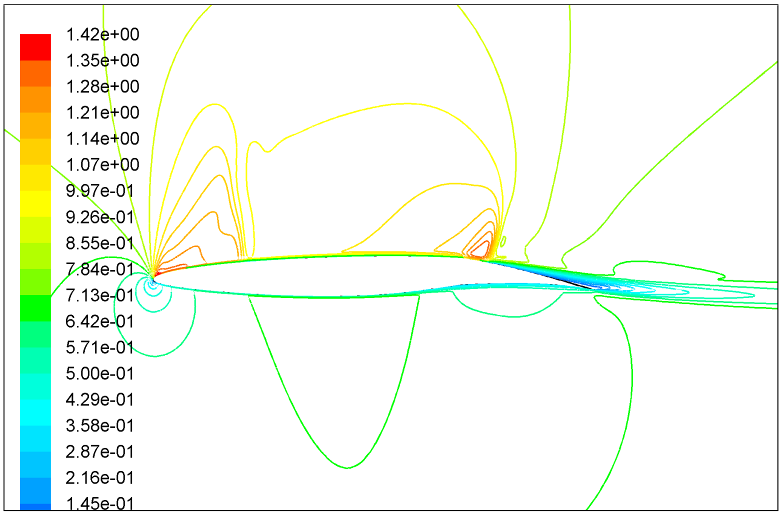

Figure B.26: Mach contour of VCCTEF 6 at 1.1 AoA at M =0.7

For all the configurations as the AoA is increasing, the strength of the shocks also increases.The position of the leading edge shock moves right whereas the formation of the aft-shock is almost at the same position. This is same for VCCTEF 6 (as seen in the Fig. B.25 and B.26).

Vitae

- Name: Mohammed Abdul Raheem
- Nationality: Indian
- Date of Birth: 04-08-1987
- Email: *aeroraheem@gmail.com*
- Permenant Address: 19-2-11/129/8A,
  Misrigunj, Hyderabad - 500053,
  Telangana, India.
- Education: B. Tech (Aeronautical Engineering)
  Institute of Aeronautical Engineering, Telangana, Hyderabad.
  Percentage : 83 out of 100
- Education: MS (Aerospace Engineering)
  King Fahd University of Petroleum and Minerals,
  Dhahran, 31261, Kingdom of Saudi Arabia.
  GPA : 3.5 out of 4

Publication:

Dr. Prasetyo Edi and Mohammed Abdul Raheem, “The application of Variable Camber Continuous Trailing Edge Flap on HLFC-ATRA-Outboard wing section,” *Journal of Aircraft*, (To be submitted).